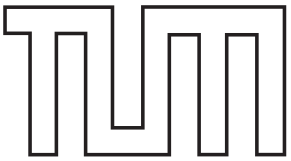

Fakultät für Elektrotechnik und Informationstechnik

Hyperspectral Imaging Microscopy for Atomic Layer Mapping of Two-Dimensional Materials

Xingchen Dong

Vollständiger Abdruck der von der Fakultät für
Elektrotechnik und Informationstechnik
der Technischen Universität München
zur Erlangung des akademischen Grades eines

Doktors der Ingenieurwissenschaften

genehmigten Dissertation.

Vorsitzender:		Prof. Dr.-Ing. Christian Jirauschek
Prüfer der Dissertation:	1.	Prof. Dr.-Ing. Dr. h.c. Alexander W. Koch
	2.	Prof. Vasilis Ntziachristos, Ph.D

Die Dissertation wurde am 17.02.2021 bei der
Technischen Universität München eingereicht und durch die Fakultät für
Elektrotechnik und Informationstechnik am 18.10.2021 angenommen.

Abstract

Two-dimensional (2D) materials including graphene, transition metal dichalcogenides (TMDs), and black phosphorus (BP) show unique physical properties when controlled to mono- and few-layer thickness, and therefore are promising for optic and photonic devices. The optical, electrical, and mechanical properties of 2D materials are largely dependent on their atomic layer numbers. Optical microscopy is widely implemented to distinguish 2D flakes but the lack of abundant spectral information makes it difficult to confirm the exact layer number. Spectroscopic techniques such as Raman and photoluminescence microscopy are time-consuming when applied for large-area flake searches due to the point-scan mode. Ellipsometry microscopy is an industrial-standard measurement technique, but modeling and interpretation of spectral ellipsometry data require previous knowledge of the properties and structures of the measured materials. Line-scan hyperspectral imaging microscopy which combines both spectroscopy and imaging techniques provides both spatial and spectral information, realizing a satisfying trade-off between the measurement speed and accuracy in layer number identification within a large-area sample. This work studies the suitability of hyperspectral imaging microscopy for rapid and accurate atomic layer mapping of 2D materials.

First, a hyperspectral imaging system including a line-scan hyperspectral imaging microscope, system control, data acquisition, and data processing was custom built. The control and image acquisition of the system worked in MATLAB. The image processing for reconstructing layer maps was developed from manual interpretation (MATLAB environment) to the machine-learning-based method (Python environment). The spatial and spectral parameters of the system were calibrated and the details of the system were introduced for rebuilding such a system.

Second, to interpret the multidimensional data set acquired by the hyperspectral system for 2D materials layer mapping, manual interpretation methods including spectral unmixing and peak position mapping were developed. A comparative study was conducted to process the multidimensional data set of multi-layer molybdenum disulfide (MoS_2), showing advantageous performances of the spectral unmixing method. A complete hy-

perspectral analysis, including single-band analysis, pixelwise spectral analysis, and image classification were conducted using MoS_2 and hexagonal boron nitride (hBN) with mono- and few-layer thickness. To test the identification limit of the system for layer mapping, the hyperspectral data set of MoS_2 flakes with monolayer, bilayer, trilayer, multi-layer, and bulk, was interpreted and spectral fingerprints of all flake categories were extracted to form a hyperspectral library. The reconstructed maps showed atomic layer maps with one-atomic-layer resolution.

Third, to further develop an intelligent system for fully automated large-area atomic layer mapping, a deep fusion neural network based on the U-Net architecture was proposed for imagery fusion of hyperspectral microscope data sets and RGB microscope images, with monolayer, bilayer, trilayer, and multi-layer MoS_2 employed as a demonstration. After multimodal information acquisition, data sets co-registration, network training and testing, the deep fusion neural network realized one-layer precision and accurate profile outputs. A quantitative comparison showed advantageous performances of the deep fusion network over the state-of-the-art single-stream U-Net model solely based on RGB microscope images. This deep-learning-supported technique with high speed, high spatial resolution, and high accuracy is prominent for fully automated 2D materials characterization.

Contents

Chapter 1

Introduction

With the development of technical instrumentations, we humans can observe and view objects of the world in largely different scales from nanometer to thousands of kilometers away. The invention of the microscope opens a new view to observe the world of micrometer and even nanometer scales which cannot be realized by naked eyes, while the telescope enables us to observe the far-away world in a large field of view, both largely extending our understanding in the spatial domain. Spectroscopy, which studies the interaction between matter and electromagnetics by splitting the light and analyzing the radiation intensity with wavelengths, enables us to interpret our world in the spectral domain. Spectroscopic imaging is the combination of imaging and spectroscopy, and thus possesses more advantageous performances as a measurement tool.

As a sub-class of spectroscopic imaging, hyperspectral imaging technology has developed rapidly since it was first employed for remote sensing in the late last century [1–5]. Nowadays, the application of hyperspectral imaging technology is not only in the field of remote sensing and earth observation, but also in other wide fields such as agriculture, food processing, surveillance, eye care, environment, and chemical imaging [6–11]. A hyperspectral data set can contain both spatial and spectral information of the detected substance with very high resolution. Due to a large number of spectral bands, sufficient spectral information can be extracted from hyperspectral data sets [12]. Hyperspectral data sets use wavelength as the z-axis, x and y as the spatial axis. Spatial information of hyperspectral images is useful to analyze the distribution of detected microscale and nanoscale materials, whereas the spectral information of these images is important for property analysis. Hyperspectral imaging can reduce both time and resource consumption, and provide abundant information at the same time. The combination of microscopy and spectroscopy, which is called microscale spectroscopic imaging, provides microscale spatial information with high resolution and extra spectral information, and therefore

provides more detailed quantitative information. Hyperspectral imaging microscopy has been employed in many fields such as materials science and biological imaging.

1.1 Motivation

2D materials possess unique optical properties as compared to their bulk counterparts, specifically when the thickness is controlled within a few layers. Prominently, a direct to indirect bandgap transition occurs for the family of semiconducting TMDs when the layer thickness is increased from monolayer to bulk [13–15]. Van der Waals stacked devices made of individual materials and layers have attracted interests for next-generation optics and photonics applications [16–18]. 2D materials family can be roughly categorized as semimetals such as graphene, semiconductors such as TMDs, and insulators such as hBN from the aspect of bandgap differences [19]. Ultrathin graphene film shows excellent performances for applications in flexible transparent conductors (FTCs) and field-effect transistors (FETs) [20, 21]. FTCs made of graphene can be used for flexible touch screens and displays, printable electronics, and thin-film photovoltaics [22], while FETs made of graphene can be used for highly-sensitive biosensors [23]. Another 2D material MoS_2, a direct-bandgap semiconductor, has applications in ultrasensitive photodetectors, transistors, and gas-sensing devices [24–27]. Other 2D materials have also shown potential in photovoltaic devices, memory, and light-emitting diodes (LEDs) [28, 29]. In the molecular structures of these materials, the atoms are bonded hard in the same plane, but the bond effect between two lateral layers is weak due to van der Waals forces [30]. Due to the experimentally practical manipulation of mono- and multi-layer 2D materials, remarkable optical performances can be realized for a wide range of optical applications.

A conventional method to fabricate individual mono- and few-layer 2D structures is micromechanical cleaving of bulk crystals using Scotch tape. Typically, this method produces a wide array of flakes with varying thickness over a macroscopic area. Although it is in principle possible to identify the thickness of the layers by optical contrast, searching for a specific flake of determined layer thickness is arduous and time-consuming [31]. CVD method is a method to grow large-area 2D materials with atomic-layer thickness [32–35]. For quick evaluation of the layer distribution to optimize parameters during the CVD process, there is a high demand to rapidly scan the large area and distinguish the layer number of crystals both in the laboratory and industrial applications.

Conventional optical techniques to determine the layer thickness of 2D flakes include optical microscopy, atomic force microscopy, Raman spectroscopy, photoluminescence spectroscopy, and ellipsometry. Optical microscopy is widely implemented in the laboratory to search the sample and distinguish 2D flakes from monolayer to few-layer based on the

optical contrast [36, 37]. The challenge is the lack of abundant spectral information because of the RGB-based design, which makes it difficult to confirm the exact layer number of flakes [38, 39]. Raman spectroscopic mapping has been used for automated identification of 2D materials on Au and Si substrates based on the relation between the Raman frequency shifts of E^1_{2g} and A_1g peaks (TMDs), and those of D and G peaks (graphene) [40–46]. However, the time-consuming scan due to small spot sizes of Raman imaging microscopes (around 1 µm) and the weak Raman signals make this technique not suitable for rapid large-area measurement. The same challenge exists for photoluminescence microscopy in 2D flakes search and layer number identification. Spectral ellipsometry is a standard technique used in the thin film industry and has been adapted for mapping the thickness distribution of graphene and MoS_2 with fast scanning speed [47–49]. An advantage of spectral ellipsometry is the versatility of imaging 2D materials with very low contrast such as hexagonal boron nitride. Nevertheless, modeling and interpretation of spectral ellipsometry data require previous knowledge of the properties and structures of the measured materials [50]. Time-domain Terahertz spectroscopic imaging is an emerging technique for 2D materials imaging, but the comparatively large spot size hinders the identification of laterally small flakes [51, 52].

With the fast development in both theory and practice, machine-learning techniques have shown advantages in addressing computer vision tasks such as image segmentation and object classification based on automated feature learning [53–56]. Optical microscopy has been further developed by combining fully convolutional neural networks to realize the pixelwise classification of the imagery for 2D materials layer number identification. Here, the state-of-the-art reports are updated. An unsupervised machine-learning clustering analysis based on feature extraction algorithms used the optical microscope images for thickness identification of exfoliated graphene flakes [57]. A deep neural network was applied for hBN flakes classification with “good” and “bad” labels [58]. U-Net was trained to distinguish monolayer and bilayer (together as one category) MoS_2 and graphene from the other flakes [59]. A convolutional neural network, Mask-RCNN, was implemented for image segmentation of 2D crystals (graphene, hBN, MoS_2, and WSe_2) with monolayer, few-layer (2-10 layers), and thick (10-40 layers) categories [60]. Another report implemented with VGG16 for thickness mapping of graphene, TMDs, and hBN uses also rough categories including monolayer, few-layer (2-6 layers), and multi-layer (>6 layers), making this technique suitable for initial scanning and screening of 2D materials identification [61]. Those methods have not reached one layer number accuracy when identifying few-layer flakes. The lack of abundant spectral data can be one reason for this limitation and the bottleneck of the RGB-based microscope images for more accurate identification. So far, automatic search and sorting of flakes within the haystack of a large number of randomly distributed thicknesses have not yet been realized.

1.2 Objective

The objective is to employ hyperspectral imaging microscopy for atomic layer mapping of 2D materials and study the suitability according to the laboratory and industry requirements. The development of the methodology can be summarized into three aspects:

First, a hyperspectral imaging microscopy system including optical setup, system control, and image acquisition needs to be developed. The system should be able to balance two contradictory requirements of a relatively large field of view for rapid scanning and relatively high spatial resolution for microscale 2D flakes identification. The working modes of transmission and reflection should be considered for specific circumstances. Furthermore, the system should be robust to different types of 2D materials with varying thicknesses fabricated by different methods (mechanical exfoliation and CVD).

Second, due to the large amounts of hyperspectral data sets acquired by the system, image processing algorithms need to be developed to interpret the multidimensional data sets, extract the characteristic spectral information of 2D flakes with varying thicknesses, and to conduct pixelwise classification to reconstruct the atomic layer distribution maps. A practical pixelwise classification method should be developed with a graphic user interface for laboratory interpretation of experienced operators in 2D materials research.

Third, the system should be intelligent for fully automated large-area layer number mapping of 2D materials. To realize this function, machine learning techniques can be implemented for automated feature learning using the data acquired from the hyperspectral imaging microscopy system. The trained network should provide accurate flake profiles and the identified atomic layer information.

1.3 Thesis Organization

Chapter 2 introduces the advances of microscale spectroscopic mapping techniques including photoluminescence spectroscopy, Raman spectroscopy, infrared (IR) spectroscopy, terahertz (THz) spectroscopy, and spectral ellipsometry for 2D materials characterization. Different forms of graphene, MoS_2, and black phosphorus including intrinsic and engineered structures made by different methods were selected as representatives, from bandgap and anisotropy perspectives.

Chapter 3 contains the principles of hyperspectral imaging and the multidimensional data set processing methods. A hyperspectral imaging microscope system including a line-scan hyperspectral imaging microscope, system control graphic user interface (GUI), data acquisition GUI, and the manual data processing GUI, was custom built and calibrated

for characterization of distinct micron-sized 2D materials. The hyperspectral data set processing studies were based on the discussed spectral unmixing method (Chapter 4, 5) and the deep fusion neural network (Chapter 6).

In Chapter 4, a comparative study to process multidimensional data sets using abundance mapping based on linear unmixing calculation, and peak position mapping based on differential reflectance spectra, was conducted. Multi-layer MoS_2 flakes fabricated on the SiO_2/Si substrate with 100 nm oxidation film were employed as a demonstration. The main work of this chapter is to find an effective multivariate data analysis method, linear unmixing.

In Chapter 5, to further investigate the suitability and robustness of the line-scan hyperspectral imaging microscope system with spectral unmixing for atomic layer identification, MoS_2 and hBN crystals with mono- and few-layers prepared by micromechanical exfoliation were employed. A step-by-step analysis including single-band analysis, pixelwise spectral analysis, and image segmentation was conducted. To further test the identification limit of the system, the spectral fingerprints of all the flake categories of a reference MoS_2 sample (monolayer, bilayer, trilayer, multi-layer, and bulk) were extracted to form a hyperspectral library. The library was implemented to quantitatively identify and map the distribution of distinct flakes from a new MoS_2 sample.

In Chapter 6, a dual-stream U-Net neural network was proposed to fuse RGB images (high spatial resolution) and hyperspectral images (high spectral resolution) for identification and segmentation of atomic layer flakes with monolayer, bilayer, trilayer, and multi-layer thickness grown by CVD. The deep fusion network was trained using a small number of samples, reaching high accuracy and one-layer precision for atomic layer identification. A quantitative comparison showed advantageous performances of the deep fusion network over the single-stream U-Net which used only RGB microscope images.

Chapter 2

Fundamentals and State of the Art

In this chapter, advances of microscale spectroscopic mapping instrumentations and methods covering a broad range of electromagnetic spectrum were introduced. 2D materials such as graphene, MoS_2, and black phosphorus including intrinsic and engineered structures made by different methods were selected as representatives from bandgap and anisotropy perspectives. A detailed discussion between the microscale spectroscopic images and the unique optical property findings including spatial adsorption and emission, excitonic behavior, light sensitivity, and plasmonic effects was carried out.

2.1 Microscale Hyperspectral Imaging

As an emerging technique, spectral imaging, which combines both advanced spectroscopy and imaging techniques, provides sufficient information for spectral and spatial analysis and is suitable for distribution and property investigation of microscale and nanoscale materials. Due to the small size of these materials, they are difficult to be located, characterized, and quantified [62–64]. To solve this problem, researchers have utilized different modalities including scanning electron microscope (SEM) [65], transmission electron microscopy (TEM), atomic force microscope (AFM) [66–68], X-ray diffraction (XRD)[69]. These are currently useful tools to obtain high-resolution images of surface morphology of nanoscale materials. Samples for these characterization methods should be specifically made, and the samples sometimes cannot be used for further research because of the damage caused by the equipment [70], which is a large waste of nanoscale materials, especially with respect to expensive and uncommon materials. Another drawback of these methods is that they are usually time-consuming and expensive. The third demerit lies in the fact that, when one sample is damaged by characterization methods, a new sample has to be

used to finish the complete characterization, which cannot avoid the effects caused by a small difference of samples on the final results.

Optical modalities can be the alternatives for nondestructive microscale and nanoscale characterization. Hyperspectral imaging is a combination of spectroscopy and imaging techniques, containing both spatial and spectral information of the detected substance with very high resolution, where sufficient spectral information can be extracted. A comparison among conventional imaging, conventional spectroscopy, and spectroscopic imaging is shown in Figure 2.1.

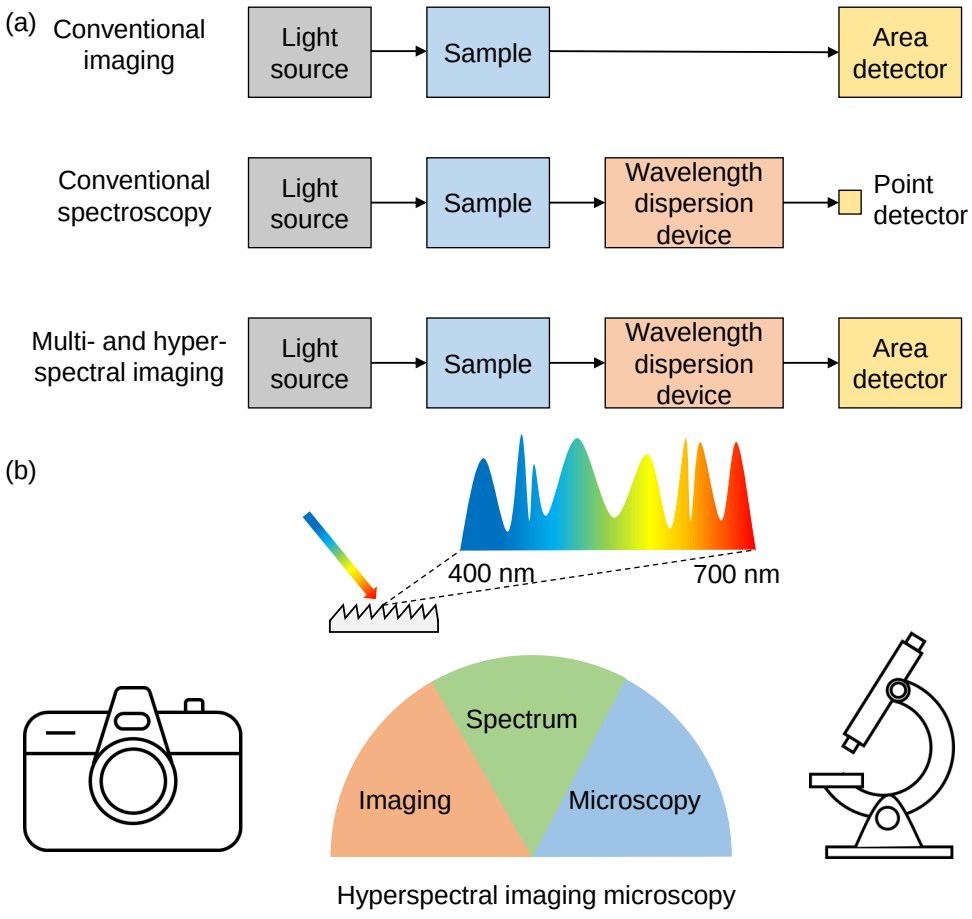

Figure 2.1: Hyperspectral imaging microscopy. (a) Comparison among imaging, spectroscopy and spectroscopic imaging. (b) The combination of imaging, spectrum, and microscopy.

Because of the enhancement of both spectral and spatial resolution when using hyperspectral imaging technology, researchers have found many applications of this technique. For example, M. S. Kim et al. built a hyperspectral imaging system for food quality and

safety purposes [71]. Using the abundant information offered by hyperspectral images, it is applicable to find disease and defects in apples. Anton J. Tremmel et al. developed an online hyperspectral system for thickness measurement of thin films [72]. It is suitable for industrial applications to obtain thickness distribution of the polymers used for electronic devices. The application fields of this technology have transferred from macro objects to nanoscale materials [73–75]. Spatial information of hyperspectral images is useful to analyze the distribution of detected nanoscale materials, whereas the spectral information of these images is important for property analysis. Hyperspectral imaging can reduce both time and resources consumption, and provide abundant information at the same time [76, 77].

Although there are differences between spectroscopic methods, a hyperspectral imaging system typically consists of a light source, a wavelength modulation system, and a detector [78]. Figure 2.2 shows a typical hyperspectral imaging system [79, 80]. The light source can be halogen lamps (broadband illumination sources), LEDs, and lasers. A wavelength modulation module consists of different dispersion devices such as imaging spectrographs and acousto-optic tunable filters. The detector can be a charge-coupled device (CCD) and complementary metal oxide semiconductor (CMOS) cameras. In order to analyze characteristic optical spectra of different materials, a wide range of wavelengths (visible, near infrared, far infrared) can be selected according to physical and chemical properties of the tested materials. Working modes (transmittance, reflectance, and luminescence) are changeable depending on the specific measurement requirements. Furthermore, some special techniques have also been utilized specifically for nanoscale materials imaging based on the unique optical performance caused by the really small size. Systematic introductions to components of a hyperspectral imaging system can also be found in published articles and books [81–85].

Reflectance was the working mode of hyperspectral imaging systems in the 1980s for remote sensing and earth observation [86], which has been developed as an effective way for identification in the visible and the near-infrared (VNIR) range. This non-destructive imaging method has proven to be effective for materials and paint layers diagnosis [87]. Transmittance with similar systematic arrangements is also a way for hyperspectral image acquisition. Studies show that hyperspectral transmittance imaging works efficiently for internal damage detection such as insect-damaged vegetable soybeans and internal quality of blueberries [88, 89].

Furthermore, photoluminescence (PL) and Raman hyperspectral imaging are employed for measuring nanoscale materials. Materials such as single-walled carbon nanotubes (SWNTs) possess excellent photoluminescent property, which means photoluminescence can be emitted when the material is photoexcited [90]. Researchers including Jack A.

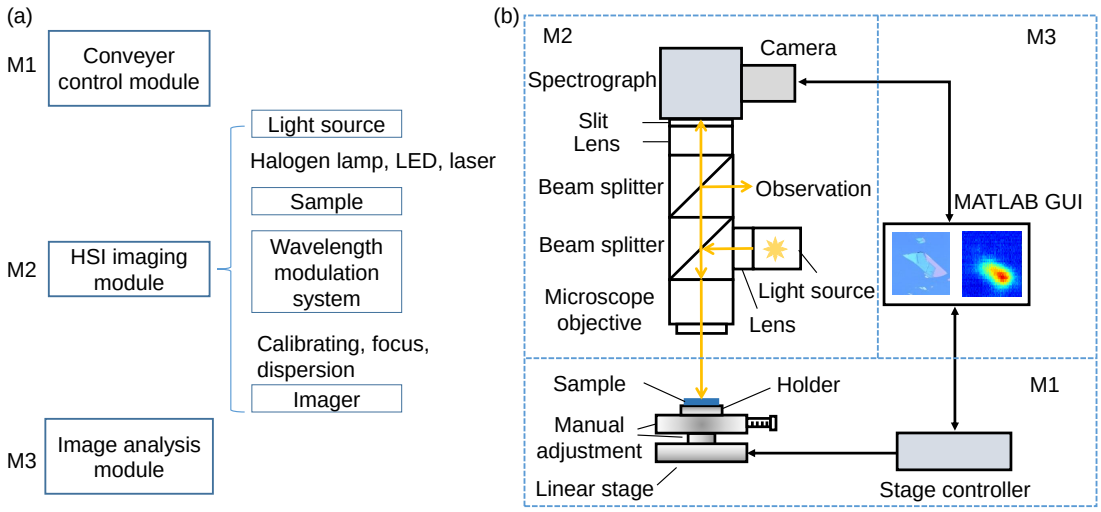

Figure 2.2: Diagram of a typical hyperspectral imaging system.

Alexander-Webber and Jacques Lefebvre have adopted PL for hyperspectral imaging of carbon nanotubes, proving PL mapping a significantly powerful tool to characterize SWNTs [91]. Such research ideas can also be conducted on other fluorophores like ultrathin MoS_2 films of which the PL property has also been studied [14]. Although Raman signals are very low, Raman spectroscopy can provide characteristic information like molecular components and defects of materials. With some special techniques such as surface-enhanced Raman, stimulated Raman, and coherent anti-stokes Raman scattering [92, 93], Raman hyperspectral imaging becomes more popular among experimental studies of nanoscale materials. Brandon M. Davis et al. built a Raman hyperspectral imaging system which greatly enhanced the operational speed by utilizing programmable optical filters and thus producing a high-throughput spectrometer [94].

Some techniques have been adopted to improve the signal-to-noise ratio (SNR) of hyperspectral imaging. For example, hyperspectral imaging with an enhanced darkfield method is currently an advanced image acquisition way of nanoscale materials. Due to the small size of nanoscale materials, imaging them faces many difficulties, especially when there are many types of materials with different sizes. The brightness of particles in darkfield environment can be largely enhanced to reach 150-fold, providing a solution to the above problem. Darkfield shows its useful suitability in nanoscale materials measurement [95]. Surface plasmon resonance (LSPR), where a strong interaction between metal nanoparticles and light leads to a specific spectrum, has enabled the recognition of chemical components [96–98]. For example, J.-S. Bouillard et al. developed a hyperspectral scanning near-field optical microscope using a gold-sputtered fiber probe for image

acquisition. Experiments were conducted on plasmonic crystals, a square array of circular holes made of gold, showing that near-field spectral behavior is suitable for physical mechanism interpretation [99]. Dominic Lepage et al. employed the hyperspectral technique to directly map the diffracted surface plasmons of semiconductor substrate in a buffered solution, allowing for implementing full dispersion mapping. A pseudo coni approach was also applied to simplify the hyperspectral imaging system, which greatly enhances the monitoring speed [100]. Additionally, surface-enhanced spectroscopy for hyperspectral image acquisition possesses higher SNR when detecting nanoscale materials. Microfilms with drug content over nanostructured gold substrates were fabricated, with hyperspectral images acquired for qualitative and quantitative analysis. Surface enhanced Raman spectroscopy (SERS) has proven a powerful thermometric tool for distribution assessment of analyses [101]. Because infrared vibrations of molecules can be enhanced at the nanometer scale due to resonant excitation of metal nanostructures, Frank Neubrech et al. reviewed surface-enhanced infrared spectroscopy using resonant metal nanoantennas [102], in which hyperspectral infrared chemical imaging is demonstrated to be an ideal characterization method for molecular species.

2.2 2D Materials and Applications

2D materials have shown unique optical properties due to their ultrathin layered structures, and are emerging as promising materials for optoelectronic devices. Graphene, MoS_2, and black phosphorus were chosen as representatives of the 2D materials family. Figure 2.3 shows the electronic structures of graphene, MoS_2, and black phosphorus. Graphene is a one-layer, zero-gap semimetal material with all the carbon atoms arranged in the same plane. MoS_2 is a wide-bandgap semiconducting 2D TMD material with a typical X-M-X unit in its molecular structure. M refers to the transition metal atoms in the same plane; X is the chalcogen atoms in the same plane, and two X planes are in the upper and lower positions of M plane to form a sandwich structure [103]. Black phosphorus is another 2D material with a narrower bandgap, and the phosphorus atoms are arranged in a puckered honeycomb lattice to form one layer sheet [104]. Figure 2.4 shows the diagrams of preparation methods of 2D materials including mechanical exfoliation and CVD grown method (MoS_2 is taken as an example).

Three typical 2D materials can be compared from the perspective of band structure and interaction with the electromagnetic spectrum. Graphene is zero-bandgap 2D material and therefore can interact with a broad range of electromagnetic spectrum from visible to infrared to terahertz range. MoS_2 has a wide bandgap from 1.0 eV to 2.5 eV showing excellent optical performances in the visible and near-infrared ranges. The bandgap of

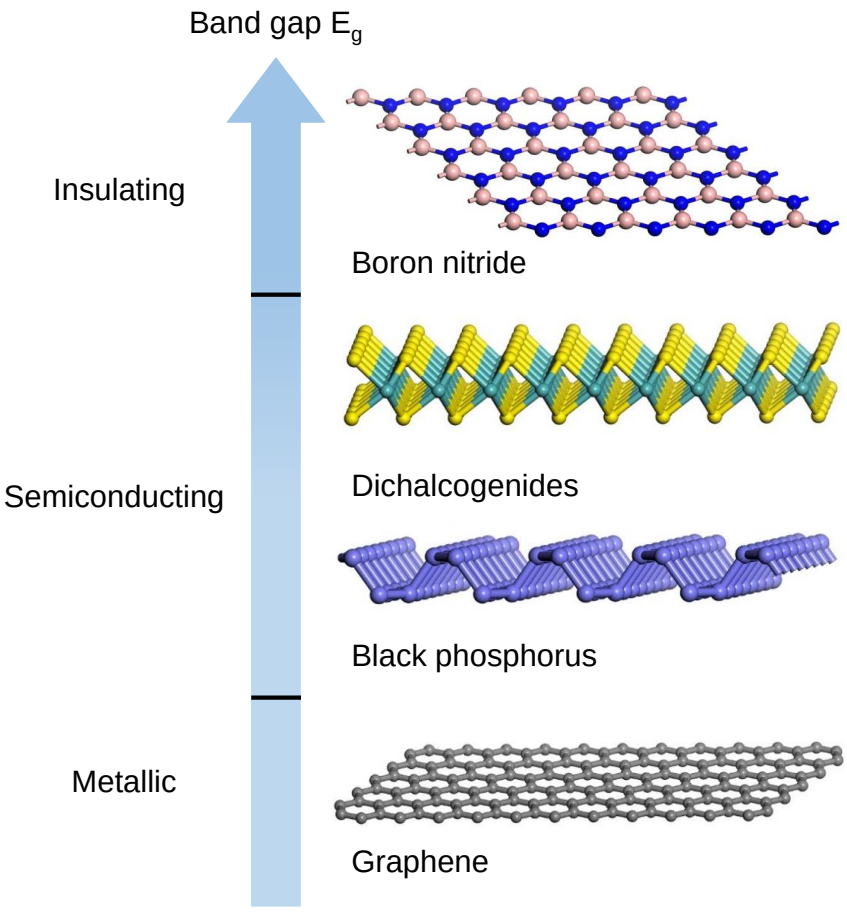

Figure 2.3: Electronic structures of 2D materials including boron nitride, MoS_2, black phosphorus, and graphene.

black phosphorus is a value between those of graphene and MoS_2, making black phosphorus suitable for mid- and far-infrared ranges. A unique property of BP different as compared to graphene and MoS_2 is the anisotropy, which has drawn considerable attention for direction-dependent optical devices. However, due to the zero-bandgap property, graphene is not suitable for some applications such as logic switches, in which both MoS_2 and black phosphorus can be utilized. The selection of these three representatives covers both the bandgap range and also satisfies the necessity of involving the studies of anisotropic 2D materials.

Optical and optoelectronic applications of these three types of 2D materials are broad in device development. Layered 2D graphene or TMDs are deposited on substrates of Si/SiO_2 or hBN and then transferred to flexible substrates such as polyimide for device fabrication. Graphene and graphene-based heterostructures have shown potential as candidates for conventional semiconductor devices including flexible photodetectors and

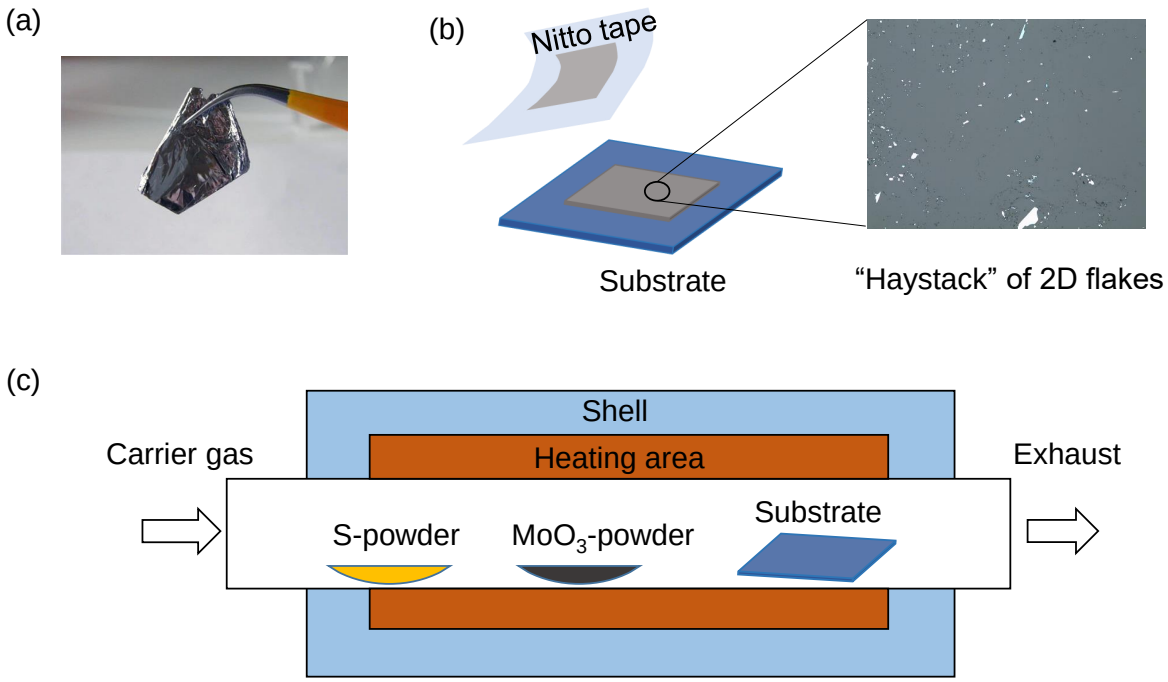

Figure 2.4: Preparation methods of 2D materials using Mechanical exfoliation and CVD grown method (MoS_2 is taken as an example).

modulators [105, 106], energy-related units such as photovoltaic devices [107], as well as LEDs, polarizers and saturable absorbers [108]. TMDs have been studied for optical and optoelectronic devices including photodetectors, excitonic LEDs, flexible optoelectronics, tunable excitonic devices, and optical generation of spin-valley currents. Two typical examples are the applications of monolayer MoS_2 for phototransistor devices with high photoresponsivity in a broad spectral range and in the integration with CMOS imaging sensors. As a revisited 2D material, BP is considered a suitable candidate for graphene and TMDs due to the flexible bandgap modulation and anisotropic property and has been studied for phototransistors [109], photodetectors [110], and solar cells [111].

The broad potential of 2D materials for optical and optoelectronic applications are generally based on the newly-discovered optical properties. Due to the unique molecular structure of 2D hexagonal lattice [112], graphene can interact with a wide range of the electromagnetic spectrum and possesses high carrier mobility. The unique property of physical flexibility has also rendered graphene an ideal choice for flexible optoelectronics, which is a strong advantage as compared to other 2D materials. The optical bandgap values enable 2D TMDs to show remarkable performances for near-infrared absorption and emission. When 2D TMDs are controlled in monolayer form, they could become direct bandgap material from indirect bandgap material in bulk form, showing strong

photoluminescence performance. 2D TMDs have been modified to make their bandgap tunable, which promotes the suitability for optical and optoelectronic devices. Strong and long-lived excitons from 2D TMDs is another advantage for applications like LEDs. The suitability of BP used for optical and optoelectronic applications lies in its properties of high carrier mobility, moderate on/off ratio at room temperature, and tunable bandgap [113, 114]. As compared to the zero bandgap of graphene and direct bandgap of monolayer MoS_2, the bandgap of BP could be changed with the thickness, showing an improved thickness-bandgap dependence [115]. Due to the changeable bandgap, BP possesses higher photoresponse performances in near- and mid-infrared ranges [116].

Optical and optoelectronic performances tightly rely on the electronic structure and unique physical properties. For example, experimental observation of photoluminescence property in single- and few-layer 2D TMDs may lead to applications in optoelectronic devices. The spectral range of primary emissions of photoluminescence is currently limited to visible and near-infrared, restricted by the excitons, energy bandgap, and the number of layers [117]. The range of photoluminescence in 2D materials has been extended by modifying intrinsic band structures [118, 119]. To overcome the limitations of intrinsic layered 2D materials and expand the optical and optoelectronic applications, the optical properties are modulated by linear tuning of Schottky barrier height, photoexcited electron transfer, and uniaxial tensile strain to realize better tunable bandgaps [120–122].

2D materials have been used for various optical and optoelectronic applications due to their unique optical, mechanical, and electrical properties [123]. The broad application potential of 2D materials in optoelectronic devices, photonic devices, and optical sensors is mainly based on their unique optical performances [124]. 2D materials can be fabricated based on their layered structure. In the molecular structures of these materials, the atoms are bonded hard in the same plane, but the bond effect between two lateral layers is weak due to van der Waals forces. 2D materials can be roughly categorized as semimetals like graphene, semiconductors like TMDs, and insulators like hBN from the aspect of bandgap differences. Due to the experimentally practical manipulation of mono- and multi-layer 2D materials, remarkable optical performances can be realized for a wide range of optical applications. For example, the number of layers of 2D materials can strongly influence the photoluminescence performance.

The unconventional optical performances including adsorption and emission, light sensitivity, as well as plasmonic effects of 2D materials are closely related to their physical properties such as carrier mobility, density of states, and band structure based on the interaction of atoms, structural symmetry, and stacking patterns [125, 126]. Through the control of layer number which could influence the bandgap value, 2D materials could react to the different spectrum ranging from ultraviolet to infrared light [127]. Doping strate-

gies are also effective to modify intrinsic 2D semiconductors and improve the response with respect to an extended range of spectrum [128]. The assessment of the optical properties of 2D materials is indispensable for device and sensor development [129]. Based on detailed surface mapping and spectral information, the suitability of 2D materials for optical devices or sensor applications can be thoroughly studied. Microscopy, direct 2D mapping of materials, can provide basic spatial information [130], while spectroscopy can offer one more dimensional spectral information which is called the fingerprints of materials [131]. Both microscopy and spectroscopy are essential approaches for analysis based on the interaction of light and materials including absorption, reflection, luminescence, and fluorescence [132].

2.3 Microscale Spectral Imaging of 2D Materials

To characterize and study the properties of 2D materials, spectral imaging microscopy has been developed to provide abundant spatial and spectral information. This part introduces the applications of spectral imaging microscopy for 2D materials characterization. Advances of both mature and developing methods covering broad ranges of the electromagnetic spectrum were introduced (Figure 2.5). A detailed discussion between the microscale spectroscopic images and the unique optical property findings including spatial adsorption and emission, excitonic behavior, light sensitivity, and plasmonic effects was carried out. The analysis also provides a generic view of microscale spectroscopic mapping selections in 2D materials imaging.

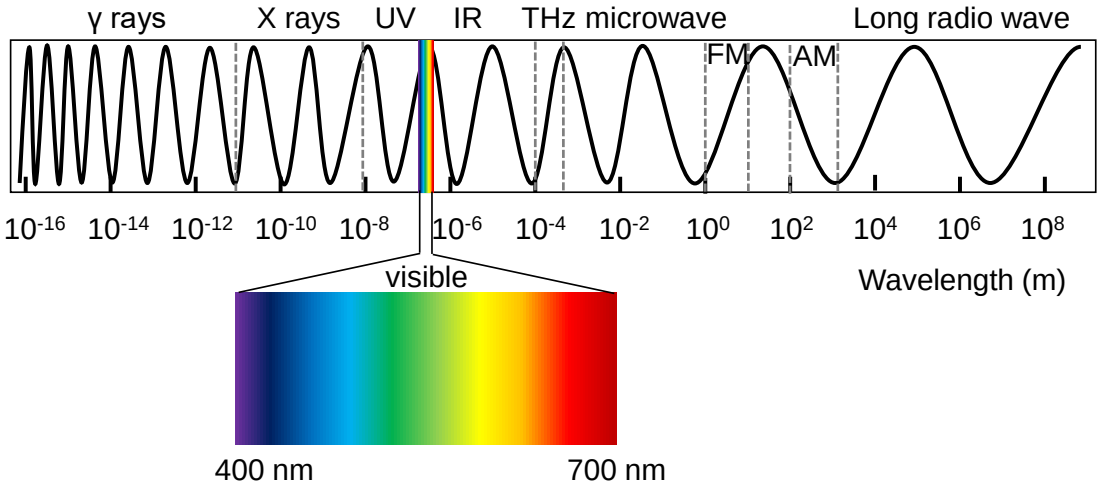

Figure 2.5: Electromagnetic spectrum.

The 2D material family includes zero-gap structures (graphene), semiconducting structures (TMDs), and insulating structures (hBN) from the bandgap perspective. Due to the large bandgap, insulating hBN is mostly utilized as substrates for semimetal or semiconducting 2D materials which perform unique optical properties to form heterogeneous structures [133, 134]. Therefore, this part focuses on semimetal and semiconducting 2D materials including intrinsic and engineered structures by CVD and mechanical exfoliation. Three typical representatives of the 2D material family, graphene, MoS_2, and BP were chosen to discuss how the microscale spectroscopic mapping techniques are used to promote the unique optical and optoelectronic properties findings such as spatial photoluminescence, long-lived excitons, anisotropic absorption, and excitons. The reviewed spectroscopic imaging techniques cover a wide range of the electromagnetic spectrum, sufficient for showing spatial performances of light-matter interactions.

2.3.1 Spectral Imaging Techniques for 2D Measurements

Microscale spectroscopic mapping techniques including PL excitation spectroscopy, Raman spectroscopy, infrared (IR) spectroscopy, THz spectroscopy, and spectral ellipsometry are described.

Based on the working position between the light source and the imaged sample, there are three types of working modes including reflectance, transmittance, and absorptance for spectroscopic imaging. Reflectance, transmittance, and absorptance spectroscopy can be utilized individually based on these three types of working modes. For example, differential reflectance has been adopted for thickness-dependent optical property investigation of intrinsic and chemically doped MoS_2 across the electromagnetic spectrum. The setup of micro-reflectance spectroscopy could be upgraded from reflectance microscopy for studying MoS_2 flakes [130]. Micro-reflectance and transmittance spectroscopy has been used to acquire spectra of a wide range of single- and multi-layer TMDs such as WS_2, MoS_2, WSe_2, and $MoSe_2$ on different substrates. Individual reflectance and transmittance spectroscopies have been used to examine samples grown by the CVD method. A laser scanning reflectance microscope with an acousto-optic tunable filter to acquire the images of an area at different specific wavelengths [135]. Furthermore, these three modes are also working modes of other spectroscopies such as IR absorption spectroscopy, THz transmission spectroscopy, and spectral reflectance ellipsometry [136].

Photoluminescence measurement exhibits fundamental spatial 2D excitons of the interlayer, in which molecules emit narrow-band light when they are excited to active states. Based on this unique natural property, different materials can be detected and imaged for measurements and analyses, especially in biotechnology and medical diagnostics [137, 138]. By photoluminescence imaging, the localization and distribution of materials

on the detected surface can be revealed [139, 140]. Figure 2.6 shows a combination of both photoluminescence and absorption spectroscopy. For photoluminescence working mode, a 355 nm pump laser was used as the excitation source, and the laser beam was focused onto the film by a focus lens, with the luminescence signal from the sample into a spectrometer and luminescence decay profiles recorded by a multichannel scaler [141]. This setup can also be used as absorption spectroscopy with minor changes.

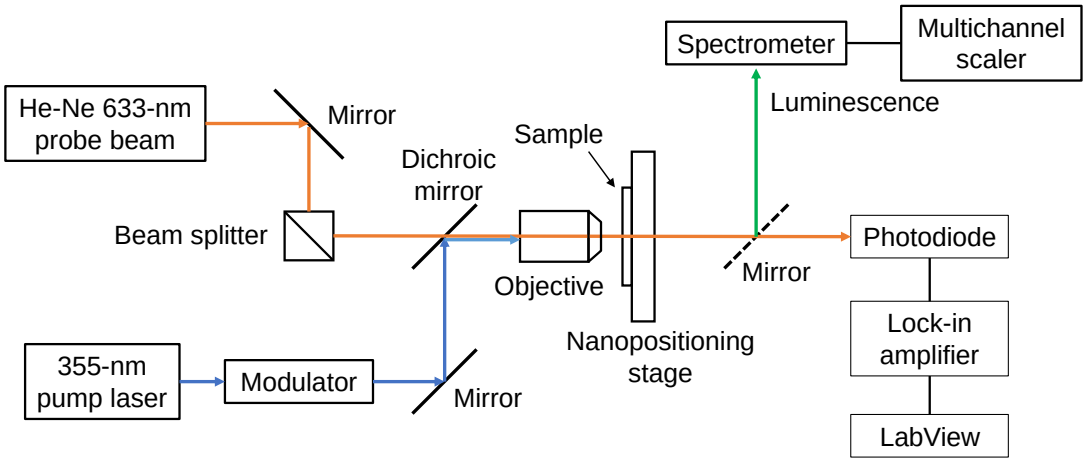

Figure 2.6: Schematic of the absorption imaging and luminescence setup.

As a robust characterization method for molecular structure and inner group determination based on the off-resonance interaction of light and material, Raman spectroscopic imaging has been widely used in chemical analysis, drug studies, and biomedical imaging [142]. It has also been proved effective in the property analyses of 2D materials, such as confirmation of layer number, defect density, and doping level [143]. Raman spectroscopic imaging has been proven a ubiquitous evaluation technique in optical- and optoelectronic-property modulation of 2D materials, and is often used as a standard reference to evaluate the performances of other new setups [121]. As the Raman signals are weak and difficult to detect, surface enhancement methods are usually adopted to improve imaging performance [144], which is also taken into consideration when evaluating the setup design. Figure 2.7 shows the design of a hyperspectral Raman spectroscopy setup for imaging of graphene and other low-dimensional materials [42]. A laser beam with a shaping module is used to illuminate the sample on the stage and the scattered light from the sample is propagated through the field of view of the microscope objective and across the beam splitter. By using tube lenses and Bragg tunable filters, the scattered light from the sample is then filtered and directed to the camera. This hyperspectral Raman imaging setup realizes global imaging with high efficiency as compared to point-by-point mapping.

IR spectroscopic imaging is based on the molecular vibration of materials and has been

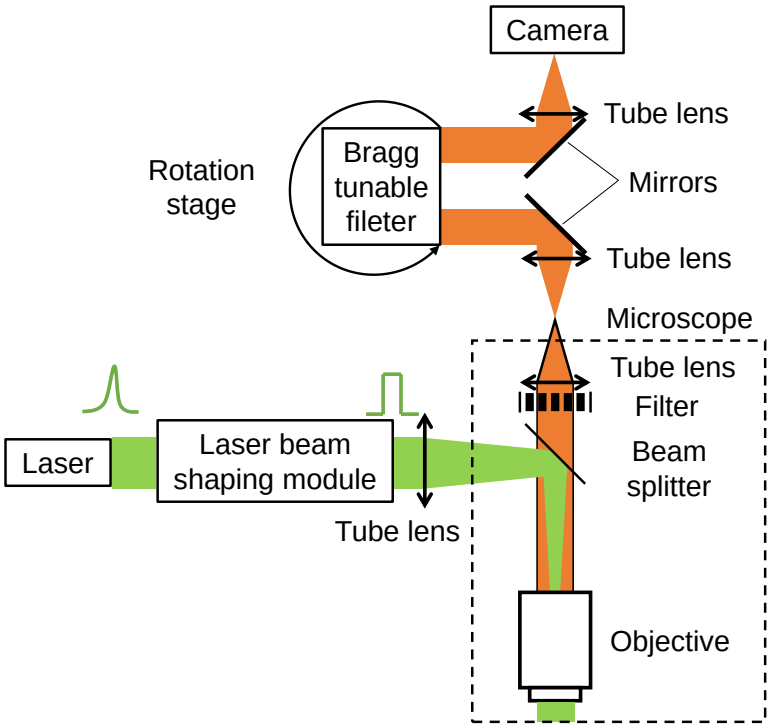

Figure 2.7: Raman spectroscopy hyperspectral imager with the excitation (green) and collection (red) beams.

widely used for chemical identification and analysis depending on the characteristic spectra of materials in the infrared frequency region. Because most materials show unique spectra in the infrared range, IR spectral imaging has shown the great usefulness as an analytical tool, especially in chemical and biological imaging [145–147]. The advances of IR spectral imaging have thus been pushed over years, and as a mature technique, there are many types of FTIR-based commercial products. Currently, the developing trend of IR spectral imaging involves maximizing the spatial resolution, improving image acquisition speed, and understanding the obtained data [148, 149].

To overcome the diffraction limit from long IR wavelengths and realize beyond-diffraction-limit spatial resolution, IR spectral imaging has been improved by combination with AFM [150]. Up-to-date researches focused on scattering-type scanning nearfield optical microscopy (s-SNOM), photothermal-induced resonance (PTIR), and discrete frequency infrared (DFIR). For example, to improve the spatial resolution of IR spectroscopic imaging to micro- and nanoscale, an asymmetric Michelson interferometer with a beam splitter (BS) and a reference mirror (RM), and an AFM cantilever are combined to build an s-SNOM (Figure 2.8). A difference frequency generator (DFG) and a nonlinear crystal produce continuum infrared light source. Nanoscale IR spectroscopic mapping of poly-

mer sample with a spatial resolution of 20 nm in 1000-1500 cm^{-1} and 1500-1900 cm^{-1} ranges was realized by scanning the sampled area in one direction [151]. Quantum cascade laser (QCL) based DFIR spectroscopic microscope working at point-scan mode has been recently proposed for faster spectral imaging by optimizing the optical parameters and reducing the overlapped data [152]. Supercontinuum source also promotes the design of a mid-IR multispectral imaging system for the imaging of component distribution within a tissue, showing satisfying imaging quality and acquisition speed compared to a commercial instrument [153], which provides new ideas for microscale spectroscopic mapping of 2D materials.

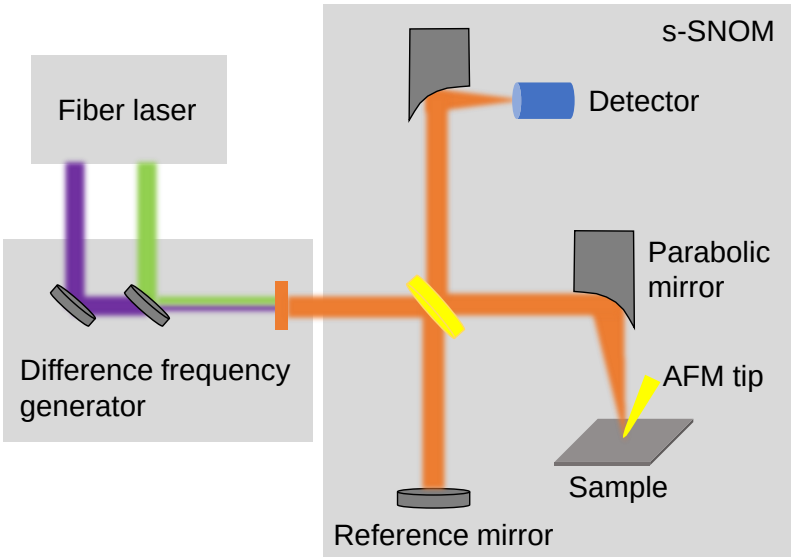

Figure 2.8: Experimental setup of FTIR operated with a coherent mid-infrared continuum source [151].

The active research activities of IR spectroscopic imaging in life sciences, polymers, perovskites, and plasmonic metasurfaces have paved the way for spatial optical property mapping of 2D materials [154–156]. The development and applications of AFM-IR have been reviewed in polymers, cells and tissues, and energy materials [157]. For 2D materials, IR spectroscopic mapping has led to the findings of many unique properties such as thickness measurement and plasmonics and now has become an indispensable analytical tool [158, 159]. For example, an s-SNOM with synchrotron radiation was utilized for plasmonic property study of single- and double-layer MoS_2 grown by the CVD method, showing the ability to detect distinctly local excitations [160]. A review about infrared vibrational nano-imaging has been finished concerning the better control of localized excitons, by focusing on s-SNOM and PTIR [161].

Due to the development of femtosecond laser, it became possible to expand the spec-

trum range to terahertz. Most materials have specific spectra signatures in near- and mid-infrared ranges, which has been widely used for material identification and characterization. For the terahertz range, materials might show different spectroscopic effects as compared to those of the visible and infrared ranges due to the unique photon energy range of THz frequency [162]. Conventional THz spectroscopy is terahertz time-domain spectroscopy (THz-TDS), and the principle of THz-TDS is based on the methods designed for FTIR. Figure 2.9 shows the diagram of a typical THz-TDS method for material measurement. A BS propagates the laser pulses direct in two ways of THz generation and gate path. The generation of THz pulses relies on the optical rectification (OR) of femtosecond laser pulses in the nonlinear crystals such as ZnTe, GaP, and GaAs [163]. The laser beam in the THz generation path is delayed and focused on the emitter. The THz pulse is then collected and focused onto the sample by off-axis parabolic (OAP) mirrors and transmitted through the sample and the transmitted pulse is measured by the detector with the pulse of the gate path [164].

THz spectroscopy has been utilized for studying optical and optoelectronic properties of a wide area of 2D materials, including characterizing the charge carrier mobility of 2D InSe, GaAs, and InP nanosheets under photoexcitation [165, 166], evaluating the factors that affect the optoelectronic properties of 2D perovskites such as charge transport properties, thickness, and excitonic effects [167], and also probing the conductivity and carrier dynamics of other types of layered 2D materials [168]. The spatial resolution of THz spectroscopic imaging, however, is limited by the diffraction of THz wave, which means more solutions to improving the spatial resolution are of importance when adopting THz imaging.

Spectral ellipsometry has been applied for studying the properties of various films and layers for applications in semiconductors and biology [169–171], and it has become another effective optical technique for the optical- and optoelectronic-property study of 2D materials [172]. Fundamental optoelectronic properties such as absorption efficiency, optical transitions, and excitonic properties could be measured based on the light-matter interaction [173]. The ellipsometric angles covering a spectrum range could be obtained to construct a model of the sample [174]. Figure 2.10 shows an imaging ellipsometry setup used for layer number and optical constants measurements of 2D materials [175]. The light from the light source is polarized and then illuminates the sample after passing through the compensator as an elliptically-polarized state. The reflected light from the sample as a linearly-polarized state is collected by a lens system with an objective. The ellipsometric angles are then measured by the analyzer and the region of interest is recorded by a CCD camera.

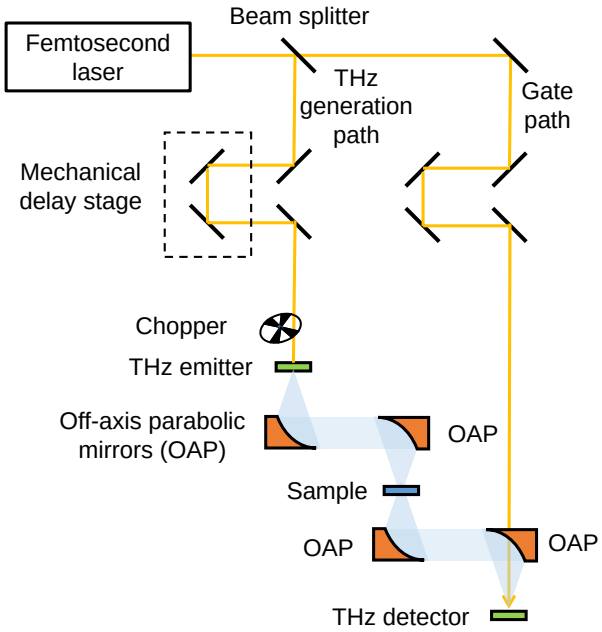

Figure 2.9: A typical terahertz time-domain spectroscopy (THz-TDS) system.

2.3.2 Spectroscopic Imaging of Graphene

Techniques utilized for studying material characteristics rely on the electronic structures of materials. Graphene is a gapless 2D material with all the carbon atoms arranged in one plane. Several planes can interact with each other to form multi-layer graphene by van der Waals forces. Therefore, graphene can interact with a wide range of electromagnetic waves without being limited to the visible or near-infrared range, but also in far-infrared and terahertz range. Graphene has been characterized and studied by spectroscopic mapping over the widest range of electromagnetic waves.

Reflectance and transmittance spectroscopies were used for studying the optical properties of graphene in combination with simulated models. For example, the optical constants of monolayer graphene on SiO_2 films have been studied, by comparing the reflectance and transmittance spectra with the calculated results [176]. Other studies focused on the optical absorption spectra, and the wavelength ranges from visible light to terahertz [177]. A laser scanning microscope has been utilized in the visible range from 545 nm to 700 nm to obtain the plane images of few-layer graphene. The spectral information analysis of monolayer, bilayer, and trilayer graphene implied a nonlinear relation between optical conductivity and the number of graphene layers [135]. Due to the interactive ability of graphene with a wide range of the electromagnetic spectrum, reflectance spectroscopy in the terahertz and the mid-infrared range was also conducted to study the carrier property of graphene layers on various substrates [178].

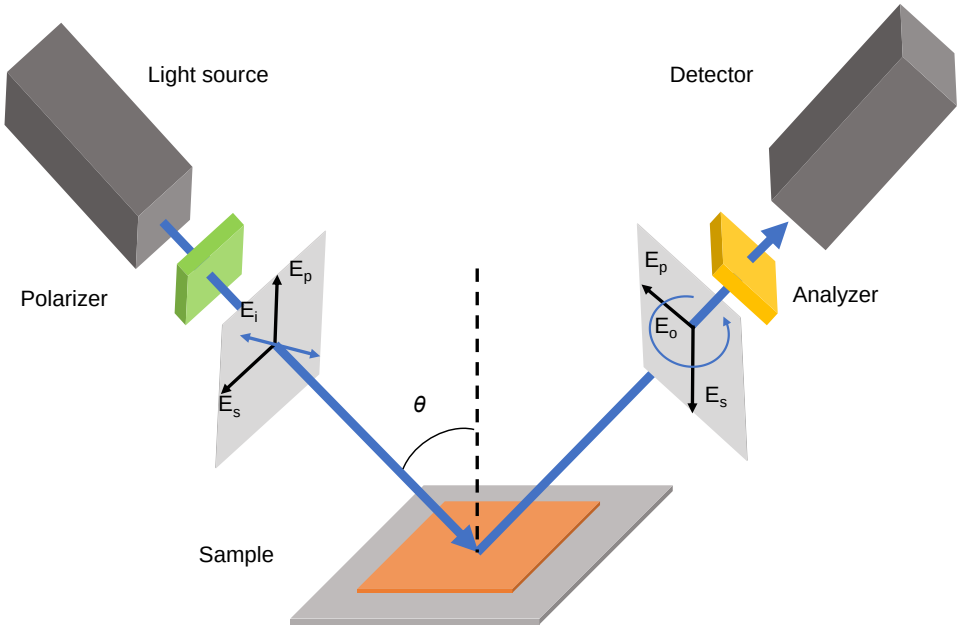

Figure 2.10: Spectroscopic imaging ellipsometry setup.

Raman imaging is a powerful technique for optical property analysis of single-layer and multi-layer graphene. A tip-enhanced Raman spectroscopy (TERS) working at the line-scan mode verified the localization of D peak enhancement at the edge of graphene [179]. A hyperspectral Raman imaging was developed by combining Raman spectrometer with Bragg tunable filter (BTF) for global mapping of graphene, with Raman images and spectra of layered graphene obtained. Spectroscopic Raman imaging with BTF shows better efficiency and higher throughput compared to the commercial point by point system and confocal scanning Raman imaging system with a continuum laser source. Compared with Raman spectroscopy, Raman spectroscopic imaging has been improved with the mapping ability for spatial quantitative and qualitative material characterization.

The interlayer rotation and interactions of twisted bilayer graphene (tBLG) which is the dominant form of production by the CVD method, have been studied [180]. The Raman spectrum of two single layers, artificial bilayer, and CVD bilayer graphene of different layer contacts were obtained and quantitatively analyzed by Raman imaging based on the precise imaging of the twist angle. The direct optical imaging of key parameters including twist angle and optical transition strength provided tBLG with potential applications in optical and optoelectronic devices. Such quantitative data demonstrates the utility of spectroscopic imaging to study the correlation between optical properties and electronic structure.

IR spectroscopic imaging plays a key role in understanding the surface plasmonics and

plasmon-phonon coupling of graphene heterostructures. The localization of surface plasmons and coupled excitations in graphene were spectroscopically studied, and based on that, the researchers realized active control of plasmon resonance through the tuning of the excitation wavelength [181]. A novel practical method was proposed to image the modulated hyperbolic polaritons of monolayer graphene/h-BN metastructure, based on the nano-infrared imaging and s-SNOM. The broadband spectroscopic data of the interaction region was obtained by tip- and line-scan modes [182]. To better understand the plasmon-phonon coupling of graphene and substrates and promote fast, compact, and efficient optical devices fabrication, commercial FTIR microscopy, and s-SNOM have been utilized to demonstrate the enhancement of phonon lifetime. A new plasmon-phonon interaction of graphene and hBN plasmonic nanostructures on SiO_2/Si substrates was revealed. A new method for tuning plasmon performance of van der Waals heterostructure was offered [183]. The plasmon reflection of graphene on SiO_2/Si substrate and sandwiched hBN flakes was studied based on an infrared s-SNOM, with the infrared light from an AFM tip exciting the edge reflection of graphene. Based on the experimental phase shift and peak oscillations, theoretical analysis of modeling and simulation was developed for 2D polaritons [184]. The enhancement of IR active phonon bands of graphene/h-BN and graphene/SiO_2 heterostructures with different graphene layer numbers were observed and studied based on the morphological and spectroscopic information offered by s-SNOM [185]. Besides, the combination of IR spectroscopic imaging with THz spectroscopy can provide information over a larger wavelength range.

Due to the wide optical and optoelectronic applications in photoconductive detectors, terahertz emitters, and modulators within terahertz range [186], THz transmission imaging of graphene on Si substrate was conducted using local free carrier dynamic analysis in a sub-mm resolution in a large area [187]. Other studies mainly focused on the conductivity imaging of graphene using THz conductivity spectroscopic imaging to assess electrical parameters such as charge carrier mobility, ionized dopant density, charge carrier lifetime, and surface recombination velocity of graphene [188]. The transmission properties of large-area graphene films have been studied through time-domain THz and FTIR spectroscopy in a frequency range from 10 to 10000 cm^{-1} [189]. The external gate voltage and thermal annealing influenced the dynamic conductivity change of single-layer graphene devices due to their effects of moving the Fermi level. A comparison of photoconductivity maps with Raman maps also suggested eliminating spatial inhomogeneities in optoelectronic fabrication. This study provided both experimental and theoretical basis for the potential application of graphene devices in optoelectronics [190]. Such studies not only show the significance of THz spectral imaging in optical property control, but also offer ideas of improving the spatial resolution of THz imaging system by spatial modulation.

Spectroscopic imaging ellipsometry in the visible-range reflectance mode has been utilized for studying the optical properties including optical constants and complex refractive index of mechanically exfoliated graphene flake and large-area graphene produced by CVD [191, 192]. The optical properties of exfoliated graphene have been studied by spectroscopic imaging ellipsometry in the visible range [193]. Angle maps of graphene and the Cauchy water layer on Si substrate with a fixed angle 60° at the wavelength of 430 nm were measured. After a whole map fitting, the thickness distribution and corresponding cross sections of graphene and water layer were obtained based on the Fano model of graphene. The optical properties of mono- and multi-layer graphene such as refractive index, extinction coefficient, and absorption peaks, have been also studied over a broadband energy range from 0.7 eV to 9.0 eV [194]. The refractive index and extinction coefficient were extracted and compared, with absorption peaks and layer-number dependence observed and analyzed. Spectroscopic imaging ellipsometry working in the range of 250-1700 nm was used for the imaging of graphene on SiO_2/Si substrate, covering an area about 1.5×1.2 mm^2. Both simulation and experiments were conducted for monolayer graphene search. Ellipsometric contrast micrography (ECM) mode within spectroscopic imaging ellipsometry was also used for fast imaging of graphene layers on SiO_2/Si, Si wafers, and rough Cu catalyst foils. This technique could be used for 2D characterization of graphene on different substrates and also other 2D structures as a standard approach. Obvious improvements of this report are the quantitative analysis and systematic suitability for different 2D heterostructures.

2.3.3 Spectroscopic Imaging of TMDs

Bulk MoS_2 is an indirect bandgap semiconductor, with a bandgap value of 1.35 eV which changes with the number of layers [195, 196]. When the thickness of 2D MoS_2 decreases to monolayer, MoS_2 will become a direct bandgap semiconductor, with a bandgap value of 1.85 eV. As a result, the photon energy usually ranges from visible to near-infrared at 400-900 nm (1.4 eV-3.1 eV). As one of the most promising van der Waals semiconductor, MoS_2 has been studied by advanced informative methods for intrinsic and enhanced property performance like surface excitons.

Reflectance optical setups have been used to study the spatial exciton properties of MoS_2 on SiO_2 films of different thickness [197]. The reflection spectra were compared to analyze the relation between emission wavelength of A and B excitons and MoS_2 layer number based on different reflection spectra of bare SiO_2 substrate and 1-layer, 3-layer, 10-layer MoS_2 on SiO_2 substrates of different thickness. The reflection and antireflection properties of MoS_2 flakes and SiO_2 substrates were measured. Additionally, the dependence of exciton property and layer number was studied using reflectance setup and the exci-

tonic features were analyzed based on the band structure of different layer number [198]. Confocal absorption spectral imaging was also used to study the absorption property of both intrinsic and doped MoS_2 layers on glass substrates, and to quantitatively obtain the shift of absorption spectra peaks as the atomic thickness changed. The dependence of the optical transitions and thickness of MoS_2 was explained based on band scheme and simulation results.

The imaging results obtained from reflectance and absorptance modes are usually compared to the information acquired by photoluminescence excitonic imaging setups. For example, the photoluminescence properties of 2D MoS_2 with a thickness of the unit cell were studied. Normally the ultrathin-layered MoS_2 was fabricated on quartz or Si/SiO_2. For spatial identification, reflected optical microscope and atomic force microscopy were utilized to distinguish the number of MoS_2. A combination of photoluminescence and Raman spectroscopy showed extended photoluminescence of monolayer MoS_2 even if the Raman signal was weak due to a relatively small local field effect. In the following studies, exciton peaks of ultrathin layered MoS_2 were confirmed at photo energies $\sim$1.90 eV, $\sim$2.05 eV, and $\sim$2.3 eV, respectively. The dependence between the positions of these three peaks and the number of layers was studied based on micro-reflectance and transmittance spectroscopies. A hyperspectral spectroscopic imaging setup working in transmission mode was built with a tunable light source with a wide range of illumination wavelengths, and the spatial C and A exciton peak positions of single- and few-layer MoS_2 were obtained and analyzed from layer number perspective. The imaging results including absorption wavelength and exciton peak wavelength are consistent with previous studies obtained from scanning photoluminescence.

Photoluminescence spectroscopic imaging was utilized to study the excitonic performances of MoS_2 through defect engineering and oxygen bonding, with strong PL enhancement observed at a high spatial resolution of $\sim$300 nm [199]. Also, optical property of Er-doped MoS_2 was studied by micro photoluminescence spectroscopic imaging using a continuous-wave (CW) diode laser with the excitation at 980 nm, covering an area of $200\mu m \times 100\mu m$. Er doping extended the range of photoluminescence of MoS_2 . In this research process, PL spectroscopic mapping plays an essential role in optical property finding of newly-developed 2D materials. Study of optical-property improvement of single- and few-layer MoS_2 not only involves photoluminescence spectroscopic imaging, but also Raman spectroscopic imaging. The results obtained by Raman spectroscopic imaging has been used as the reference of photoluminescence property. By experimentally induced defects and oxygen bonding, the photoluminescence property was largely enhanced after imaging and spectroscopic analysis. Tip-enhanced PL microscopy was utilized to study the influence of Ag- and Au-coated AFM tips on the excitonic performances of monolayer MoS_2, further

exciton emission mapping and analysis promoted the observation of PL quenching center [200]. Not limited to the research of MoS_2, photoluminescence imaging has also been demonstrated in the spatial PL intensity imaging and excitonic property study within local strain engineering of WSe_2 [201].

Raman spectroscopic imaging was used to study the optical and optoelectronic properties of MoS_2 with high reliability. By studying the local optical and electrostatic properties of mono- and multi-layer MoS_2, Raman frequency shift and intensity maps of two most pronounced features, E_{2g} and A_{1g} modes, showed the influence of thickness on the mapping identification and also the quantitative influence on Raman shifts of MoS_2 caused by Si and Au substrates [40, 42, 202]. Vibrational modes and peak width of MoS_2 depended on the layer number, and the influences of substrates on redshift were also observed. Besides, TERS was proven strong plasmonic imaging tool in revealing the quantum coupling and inhomogeneous structural features of few-layer MoS_2 on a gold substrate [203]. The shear and breathing modes in related TMDs like $MoSe_2$ and $ReSe_2$, and the spatial excitation features were also observed, expanding the suitability of hyperspectral Raman imaging in few-layer TMDs [204].

As one of the most informative tools for chemical imaging, IR has been widely adopted for spatial optical properties of MoS_2. Based on the advantageous performances of s-SNOM in spatial resolution and high reliability, anisotropy of MoS_2 on SiO_2/Si substrates was studied by determining the full dielectric tensor based on the real-space mapping [205].

The lateral homogeneity of optical constants of exfoliated MoS_2 mono- and few-layer flakes on sapphire has been analyzed using ECM and spectroscopic imaging ellipsometry (SIE) [173]. A comparison of ECM and SIE images with an optical microscope image and a monochromatic reflectivity map showed the excellent imaging performance and speed of ECM and SIE. SIE was combined with Raman spectroscopy to visualize the flakes and show the layer-sensitive energy difference. To further analyze the dielectric function of in-plane and out-of-plane components, an anisotropic model was utilized for fitting the ellipsometric spectra with critical points. This report provides a new idea of minimizing the influence of backside reflection caused by thin transparent substrates by using a beam cutter, expanding the universality of SIE to image 2D materials on different substrates.

2.3.4 Spectroscopic Imaging of Black Phosphorus

As a new member of 2D material family and potential candidate for broadband materials especially in the range of mid-infrared, black phosphorus has been studied for optical and optoelectronic devices such as photodetectors and on-chip spectrometers [206]. Currently, its unique properties are studied in combination with theoretical analysis of electronic

structures. Because of the strong in-plane anisotropy of 2D BP, the analysis of the relation between its optical properties and surface anisotropy is a research hotspot, where spectroscopic imaging techniques including angle resolved and polarized spectroscopy for systematic study of area BP are emerging as strong methods. Besides, the degradation of BP which hinders the implementation as optoelectronics has also drawn much research attention.

Absorption-mode spectroscopic imaging in visible range was conducted by focusing polarized white light on BP flakes on a quartz substrate for measurement, and the anisotropic absorption features of BP of different thickness are obtained [207]. The anisotropic optical absorption method adopted in this report can be a reliable and simple way for the identification of BP crystalline orientation. Also, polarized reflectance-mode spectroscopic imaging was utilized for both on-substrate BP and suspended BP on 2.2 µm deep trenches, illuminated by 532 and 633 nm lasers [208]. This report shows large potential of polarized reflectance for current academic research and future various device applications.

The anisotropic excitons of monolayer black phosphorus have been also observed by polarization-resolved photoluminescence spectral mapping, with a clear emitted light signature observed [209]. To show the exciton binding energy, photoluminescence excitonic spectroscopic mapping was utilized to map the relation between excitation and emission photon energies in combination with photoluminescence spectra and density functional calculation. Researchers recently revealed the mid-infrared PL emission of thick-film BP with a thickness of 46 nm, and the thickness-dependent PL emissions were also thoroughly studied [210].

For infrared spectroscopic imaging, polarization-resolved infrared spectroscopic imaging which combined a FTIR spectrometer and a microscope system was used for the investigation and analysis of anisotropic property of multi-layer BP [211]. The relative extinction spectrum and angle-resolved DC conductance were compared, showing the matching crystalline orientation. This report demonstrated the advantages of BP like narrow bandgap and excellent carrier mobility, and also highlighted the strong potential of BP in infrared optoelectronics applications. The influence of passivation coatings on the degradation of mechanically-exfoliated BP was investigated by s-SNOM, and the results showed consistance with the geometric patterns obtained by model simulation. By spectroscopic mapping, the degraded region and the change of area with time can be identified and quantitatively analyzed [212]. To better understand the precise structure and oxidation degrees of the formed phosphorus oxides, synchrotron infrared nanospectroscopy (SINS), combined with the DFT modeling, was used to acquire the point spectra of the exposed BP under different conditions [213].

The optoelectronic property of BP was enhanced from infrared to terahertz wavelength. Terahertz absorptance characteristic spectra and emerging peaks of monolayer BP-based structure were obtained. By the combination of BP sheet with substrates and structural parameter changes, different coupling states of the system could be realized and light-matter interaction could be improved, promoting the development of BP based optoelectronic devices in terahertz range [214, 215]. As the fabrication techniques develop, the requirement of large-area spectroscopic imaging of BP will advance terahertz signal detection and imaging.

For development of optoelectronic devices, the armchair and zigzag edges of black phosphorus flakes were characterized by Raman spectroscopic imaging and the A_g, B_{1g}, B_{2g}, B_{3g} symmetry modes were observed, indicating the presence of edge phonon modes in BP [216]. The performances of edge phonons in black phosphorus were analyzed and explained based on density functional theory, confirming the new mode arising in the hyperspectral Raman imaging. Raman performances and electronic band structures of BP have been reported for optoelectronic performance analysis [217]. Since the stability of BP remains an issue before BP can be used for optoelectronic devices because of oxidation, confocal fast-scanning Raman imaging was performed to map the layered black phosphorus during degradation. The effect of thickness owing to surface and edge degradation of black phosphorus was involved in the Raman intensity modulation, indicating the usefulness of PMMA passivation [218].

Due to the limit of environmentally sensitive monolayer BP and low photoluminescence emission of multi-layer BP, organic molecules were chemically doped to enhance the photoluminescence performance of multi-layer BP in the visible range at room temperature [219]. Photoluminescence and Raman imaging were adopted for influence evaluation of dopants, and the emergence of intense photoluminescence was compared with theoretical calculations and explained from the perspective of gap states. The doping methodology was a useful method to apply multi-layer BP for a broad range of optoelectronic applications.

Most of the reported spectroscopic mapping of BP are commercial setups, only a few comprise homebuilt setups. A possible reason lies in the fact that as a revisited 2D material, in the early stage of new optical property investigation, the most concerning thing is the reliability of experimental information. Commercial spectroscopic imaging like IR imaging and micro-Raman systems can provide more standardized information. However, with the optical and optoelectronic properties of BP being more reported and generally recognized, especially with the requirement for real applications, microscale spectroscopic mapping of BP working at different modes will be developed and paid more attention.

2.4 Discussion

The interaction of materials with electromagnetic waves is a critical factor. For example, FTIR and THz spectroscopic mapping methods are adopted for imaging graphene and black phosphorus, while spectral ellipsometry is optimized for visible-range imaging of graphene and MoS_2. Raman spectroscopic imaging is the most utilized technique for optical property analysis of 2D materials and is also used as a reference technique when testing other imaging techniques. Therefore, for optical and optoelectronic property measurement and analysis of 2D materials, a combination of two or more spectroscopic mapping techniques can be advantageous.

Technical challenges of microscale spectroscopic mapping techniques are higher spatial and spectral resolution, higher mapping efficiency, and advanced image post-processing algorithms. Compared to spectroscopy which focuses on one point of the sample, microscale spectroscopic mapping techniques could obtain the distribution of one area. This technical challenge relates to the movement control of scanning probes and fast area scanning, meeting the requirements of spatial resolution at the same time. Among different scanning modes for microscale spectroscopic mapping, point-scan mode mainly adopted in commercial systems and area scanning mode mainly adopted in in-house systems, are both widely-utilized modes. Point-scan systems possess higher spatial resolution but post image construction and processing are needed to obtain spectral map of the whole area. Area-scan systems can realize higher efficiency but the resolution is limited because of a relatively larger imaging area. Up-to-date reports show the trend of newly-designed systems working in area-scan and single-shot modes [220, 221]. When point-scan mode was proposed, the imaging points were not continuous in the plane. The spectral information, therefore, did not cover every point of the area. To meet such challenges, both in-house and commercial systems use the point-scan mode with image combination software to realize continuous imaging [222]. Both the precise control of moving stage and image combination algorithms can help to solve this technical challenge. For high spectral resolution, hyperspectral imaging can be realized to improve resolution to several nanometer. Multispectral and hyperspectral mapping techniques might become the development trend in materials and devices imaging in the micro scale [223]. The use the abundant spectral information and maintain high efficiency at the same time is a key challenge, which require advances in data and image processing.

For microscale spectroscopic mapping, at least three dimensional data including spatial and spectral information will be acquired by the imaging setup at high efficiency. To select and obtain the most useful information which is usually the characteristic spectral information for each point, deep learning is showing large potential for classification and

feature data extraction. From remote sensing to medical microspectroscopy, researchers are developing better algorithms to classify objects and biological materials.

2.5 Summary

Microscale spectroscopic mapping techniques have been intensively discussed to show how the optical imaging setups could be utilized for studying the optical properties of 2D materials, including intrinsic, doped and defect engineered graphene, MoS_2, and BP of different layer numbers. Key optical and optoelectronic properties involve layer number confirmation, optical conductivity, optical transition, lateral homogeneity, macroscopic defect density, contamination, photoluminescence, and edge phonon modes. These spectroscopic mapping techniques and studied optical and optoelectronic properties are also suitable for investigation of other 2D materials. Technical challenges of the current spectroscopic imaging microscopy techniques are also discussed to meet the requirement of speed and accuracy for 2D materials characterization. Multivariate analysis methods of the multidimensional data acquired by the optical modalities are demanded to further extract the characteristic spectra of 2D materials categories for analysis and understanding.

Chapter 3

Hyperspectral System and Data Analysis Methods

This chapter introduces the newly-developed methodology, line-scan hyperspectral reflection microscopy system for 2D materials atomic layer mapping. The introduction includes hyperspectral imaging components, system calibration, data acquisition, and data processing methods.

3.1 Hyperspectral System

3.1.1 Hyperspectral Data Acquisition Modes

There are four working modes including point-scan, line-scan, area-scan, and snapshot to acquire the three-dimensional hyperspectral data set. Point-scan (also called "whiskbroom") mode captures the spectrum of one pixel from the sample, and the sample or the imager moves pixel by pixel to collect the spectrum of all the pixels. Line-scan (also called "pushbroom") mode is an expansion of the point-scan mode. The spectrum of many pixels along one line can be detected and recorded by one capture, and the sample or the imager moves line by line to acquire the whole area spectrum. The point-scan and line-scan modes are spatial scan methods, which means the whole spectral dimension of a hyperspectral datacube can be obtained once, but the two spatial dimensions cannot be obtained once. Area-scan mode is a spectral scan method, where the two spatial dimensions of a hyperspectral datacube can be obtained once, but the whole spectral dimension cannot be obtained once. Snapshot mode means the spectrum of each pixel within the region can be captured at one time. Figure 3.1 shows the four working modes.

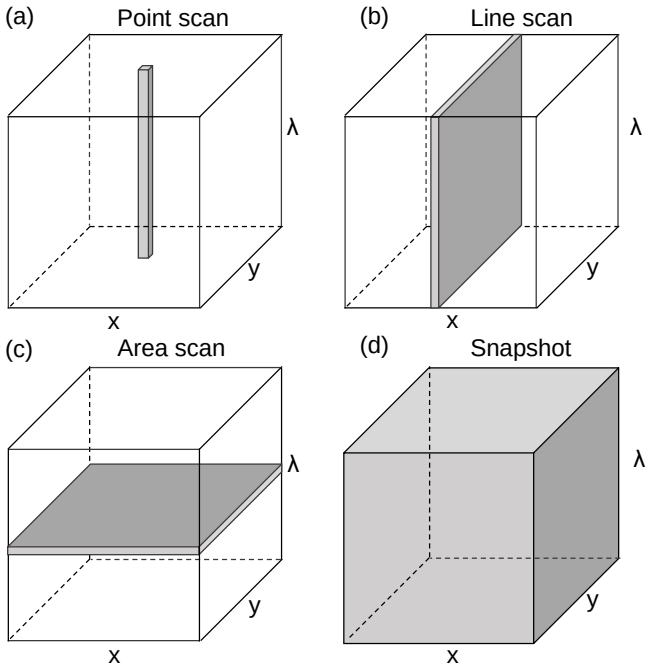

Figure 3.1: Acquisition modes of hyperspectral 3D data sets.

Light dispersion components are the main components of a hyperspectral imaging setup. Figures 3.2(a)-(b) illustrate the imaging spectrograph which disperses the light based on reflection and transmission gratings. Figure 3.2(a) shows a Czerny-Turner spectrograph and Figure 3.2(b) shows a prism-grating-prism spectrograph. These two designs are usually used for line scan mode by combining with an area charge-coupled device (CCD) detector. An entrance slit is installed before the light goes into the imager, and the spectral information along the slit direction can be captured once. The point scan mode is usually realized by the combination with a spectrometer. Figure 3.2(c) shows a Fourier transform imaging spectrometer (Michelson interferometer) which uses the interference of two beams for spectral information acquisition. This design can be used for area scan acquisition by moving the mirror. Figure 3.2(d) illustrates another area scan acquisition method using a filter wheel. A broadband beam from the object can be filtered by the filter wheel with many narrowband filters, and the spectral information of the whole area can be obtained. There are also other light dispersion devices such as acousto-optic tunable filters and liquid crystal tunable filters for area scan data acquisition.

The advantage of the point-scan mode is the high spatial and spectral resolution but this mode requires more time to scan the whole area. The speed of the line-scan mode is higher than the point-scan mode, but the spatial resolution is lower than that of the point-scan mode. The area-scan mode has a large field of view to cover more samples but

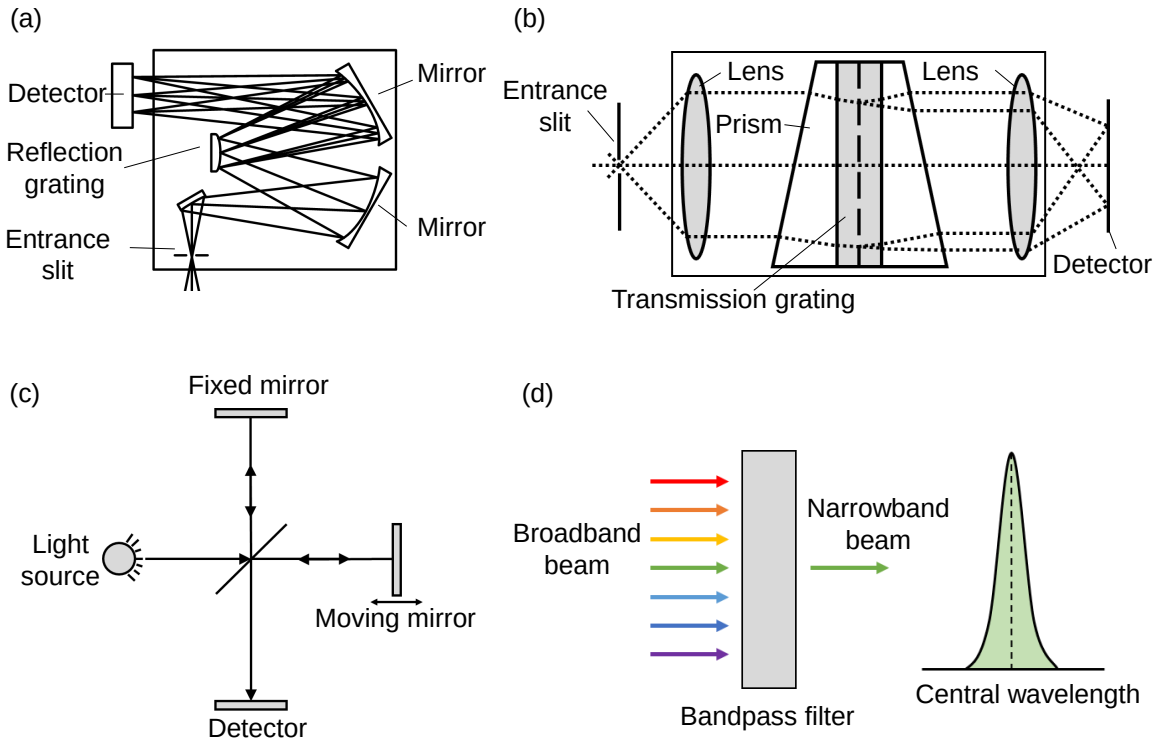

Figure 3.2: Light dispersion of the hyperspectral imager.

the spectral resolution of area scan is lower than point scan and line scan modes which use gratings for light dispersion. Snapshot requires no moving parts in the system and captures a 3D hyperspectral datacube at one time, but the spatial and spectral resolution, as well as the speed, are much lower than other modes.

3.1.2 Line-scan Hyperspectral Reflection Microscopy

Line-scan hyperspectral imagin microscopy realizes a satisfying trade-off between the measurement speed and resolution, compared to its counterparts such as point-scan, area-scan, and snapshot. Therefore, a line-scan hyperspectral imaging microscopy setup was built for surface characterization and thickness mapping of 2D materials, with high spectral resolution, high image acquisition speed, and relatively high spatial resolution. Figure 3.3 illustrates the diagram of the line-scan hyperspectral imaging microscopy system. The system contained a hyperspectral imaging microscope, a stage control, and an image processing unit. A broadband LED light source (MBB1L3, Thorlabs, Inc.) with a collimating lens was used as the illumination source in the visible range of 470-850 nm. A beam splitter (BS 016, 50:50 non-polarized cube, 400-700 nm, Thorlabs, Inc.) was used to divide the light to a 60× magnification infinity corrected microscope objective

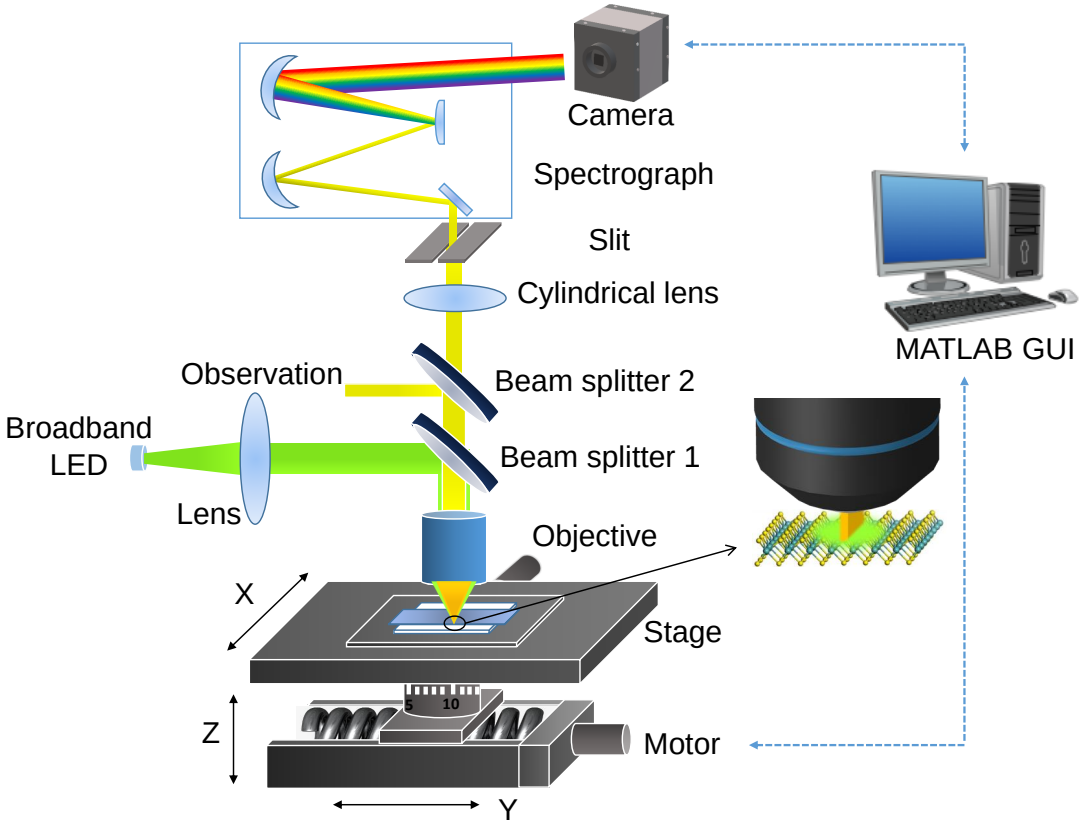

Figure 3.3: The diagram of the line-scan hyperspectral imaging microscopy system. The inset shows the illuminated area (in green) and the captured line-shape light by the camera (in yellow).

(working distance 0.3 mm, numerical aperture 0.85, Newport Corporation). The light (in green) from the light source was reflected (50%) by beam splitter 1 and projected onto the microscope objective as illumination. The reflected light (in yellow) from the sample went through the objective, beam splitter 1 and beam splitter 2, and was focused by the cylindrical lens to the spectrometer; the reflected light by beam splitter 2 was used for visual observation. When the area of interest was positioned, the second beam splitter was excluded to enhance the light throughput to the following lens and spectrograph. A cylindrical achromatic doublet (50 mm focal length) was used to focus the light in the direction of the slit with minimal chromatic aberration. The incoming light passed through a slit with 16 µm width, and was dispersed by gratings in the spectrograph (Headwall Photonics, Inc., G4-330).

The hyperspectral imager includes a spectrograph (G4-330, Headwall Photonics, Inc.) using an aberration-corrected convex reflection grating which eliminates smile and keystone aberrations, and a CCD camera (RA1000m/D, Adimec) which has 1004 × 1004 pixels

Table 3.1: Components list of the hyperspectral imaging microscope system

Module	Description	Part number	Distributor
Light source	Booadband mounted LED	MBB1L3	Thorlabs
	Collimation optics adapter	COP1-A	Thorlabs
	SM1 to SM2 adapter	SM1A2	Thorlabs
	SM2 coupler	SM2T2	Thorlabs
	4-pin connector	CON8ML-4	Thorlabs
	Slip ring	SM1RC	Thorlabs
	Power supply	325DLBN	H.G.L.
Linear stage	Motorized linear stage	VT-80-DC	PI miCos
	Compact lab jack	LJ750	Thorlabs
	Manual positioning stage	350-541-30	Owis
Hyperspectral microscope	Objective 100×/ 0.85	566073	Leica
	Objective 60×/ 0.85	LI-60X	Newport
	Adapter	SM1A12	Thorlabs
	Beam splitter	BS 016	Thorlabs
	Cylindrical lens	ACY254-050-A	Thorlabs
	Spectrograph	G4-330	Headwall Photonics
	CCD camera	RA1000m/D	Adimec
	NI camera link	PCIe-1433	NI

with the pixel size of 7.4 µm. The corresponding wavelength distribution of the dispersed light was recorded, with a frequency-spatial dispersion value of 0.74 nm/pixel. A high-precision motorized positioning platform (PI miCos GmbH, VT-80, DC) with the 50 nm resolution was controlled to move to the next step along the y direction by a MATLAB algorithm. After the area of interest was scanned by the microscope line by line, the spectra of every point within the area was captured and recorded for image processing. The photograph, the simplified configuration, and the components list of the line-scan hyperspectral imaging microscope are shown in Figure 3.4 and Table 3.1.

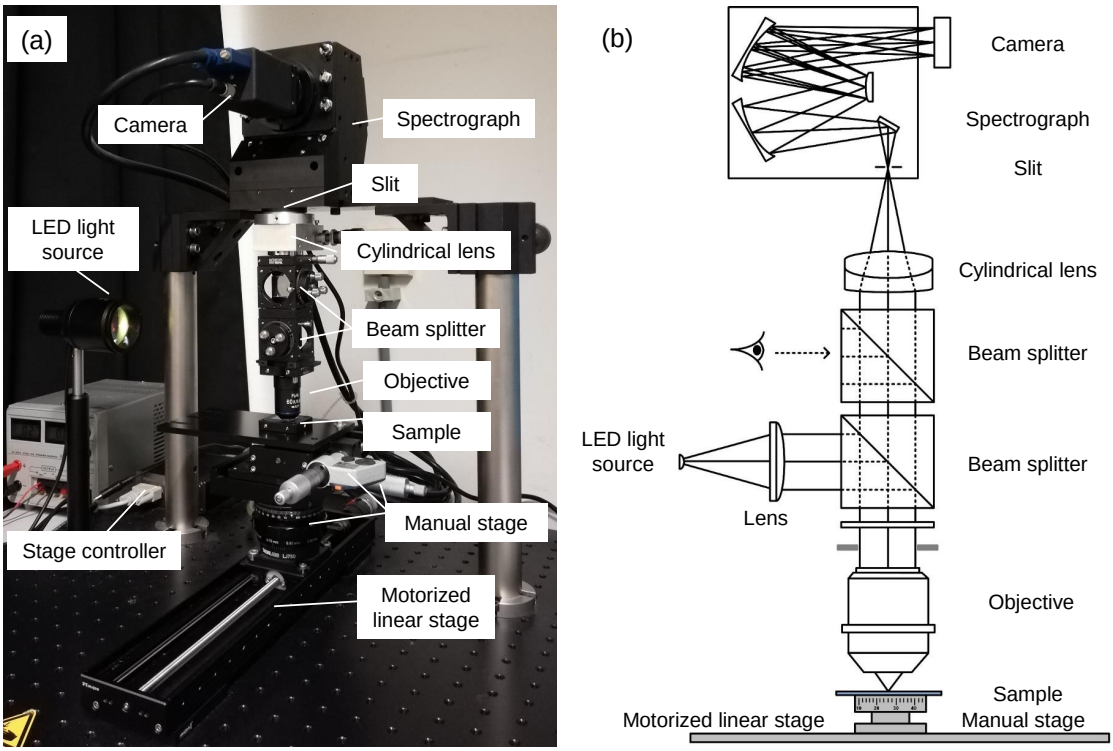

Figure 3.4: Photograph of the line-scan hyperspectral imaging microscope configuration.

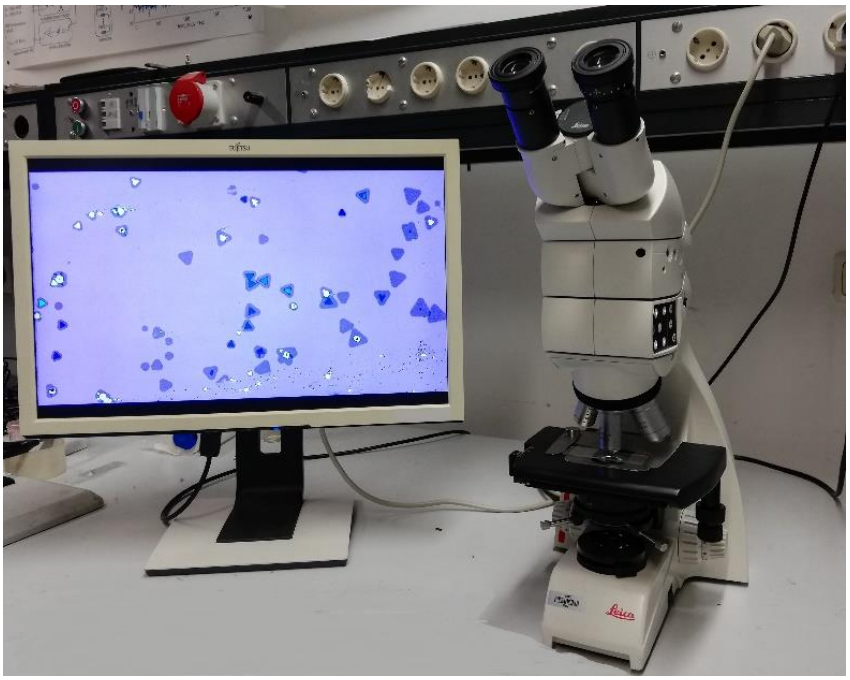

Figure 3.5: Photograph of the Leica optical microscope.

3.1.3 System Calibration

The spatial resolution represents the resolving power of one imaging system to distinguish minimum spatial differences. To test the resolving power of the line-scan hyperspectral imaging microscope, the spatial calibration in both x (horizontal) and y (vertical) dimensions was conducted using a negative NBS 1963A test target and a negative 1951 USAF test target, separately (Figure 3.6). The spatial resolution of point-scan and area-scan modes is generally the same in both dimensions when x- and y-directions of the camera have the same binning; while the spatial resolution of the line-scan mode in both x- and y-dimensions can be different.

For the line-scan mode, the horizontal resolution (along the slit direction, x) is determined by a combination of the objective, lenses, and the imager, and the vertical resolution (along the scanning direction, y) is determined by the line-shape field of view. The spatial resolution in the y-direction is determined by the width of the line-shape field of view of the system (equal to the step size). Spatial calibration is used to estimate the spatial detection limit of the system. In the horizontal direction, the line pairs of 228 lp/mm (highest spatial frequency of the negative NBS 1963A test target) was captured by one camera frame and could be clearly distinguished by the system (Figure 3.6(d)). The horizontal resolution was higher than 228 lp/mm. Along the vertical direction, the system scanned a line group of the negative 1951 USAF test target.

According to the reconstructed single-band image, the step size (5 µm) was consistent with the width of the line-shape field of view of the line-scan hyperspectral imaging microscope, without overlapping while scanning (Figure 3.6(e)). The vertical resolution was 5 µm/pixel. In this thesis, the slit was fixed with a length of 12 mm and a width of 16 µm. Therefore, the spatial resolution (both X and Y) and the spectral resolution were constant for all the measurements. The single and averaged intensity distribution of reflected light from the bare SiO_2/Si substrate with the direction along the scanning line at the wavelength of 543 nm indicated the inhomogeneous illumination, which was eliminated by excluding the spectra of the substrate from the original 3D data set (Figures 3.7(a)-(b)). The pixel-wavelength response of the hyperspectral imager was calibrated using a HeNe laser at 632.8 nm and a Hg lamp at 546.1 nm (Figure 3.7(c)). The spectral resolution was 0.726 nm/pixel.

3.2 Hyperspectral Data Acquisition

In Figure 3.8, the spectral information of pixels in the imaged line-shape area could be obtained by one capture of the hyperspectral imager. After a continuous scan, the

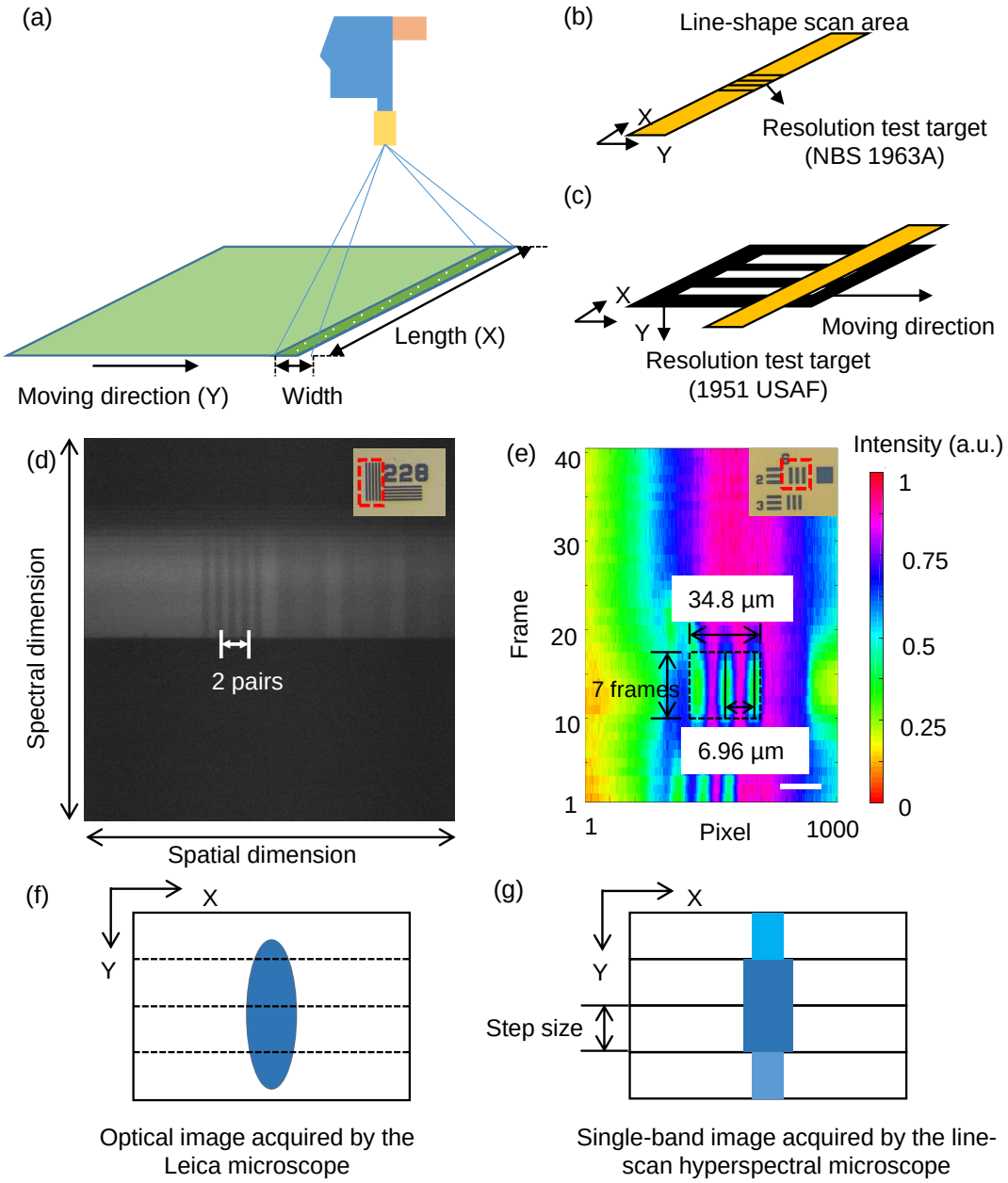

Figure 3.6: Spatial calibration of the hyperspectral imaging system. (a) The working mode of the line-scan hyperspectral imaging system. (b) Spatial calibration in the horizontal direction (x) using a negative NBS 1963A test target. (c) Spatial calibration in the vertical direction (y) using a negative 1951 USAF test target. (d) One capture of the camera with 228 lp/mm spatial frequency using the method in (b). (e) The reconstructed single-band image of the three lines with the space of 6.96 µm using the method in (c). (f) The diagram of an optical image acquired by the conventional microscope. (g) The diagram of a single-band image acquired by the line-scan hyperspectral imaging microscope.

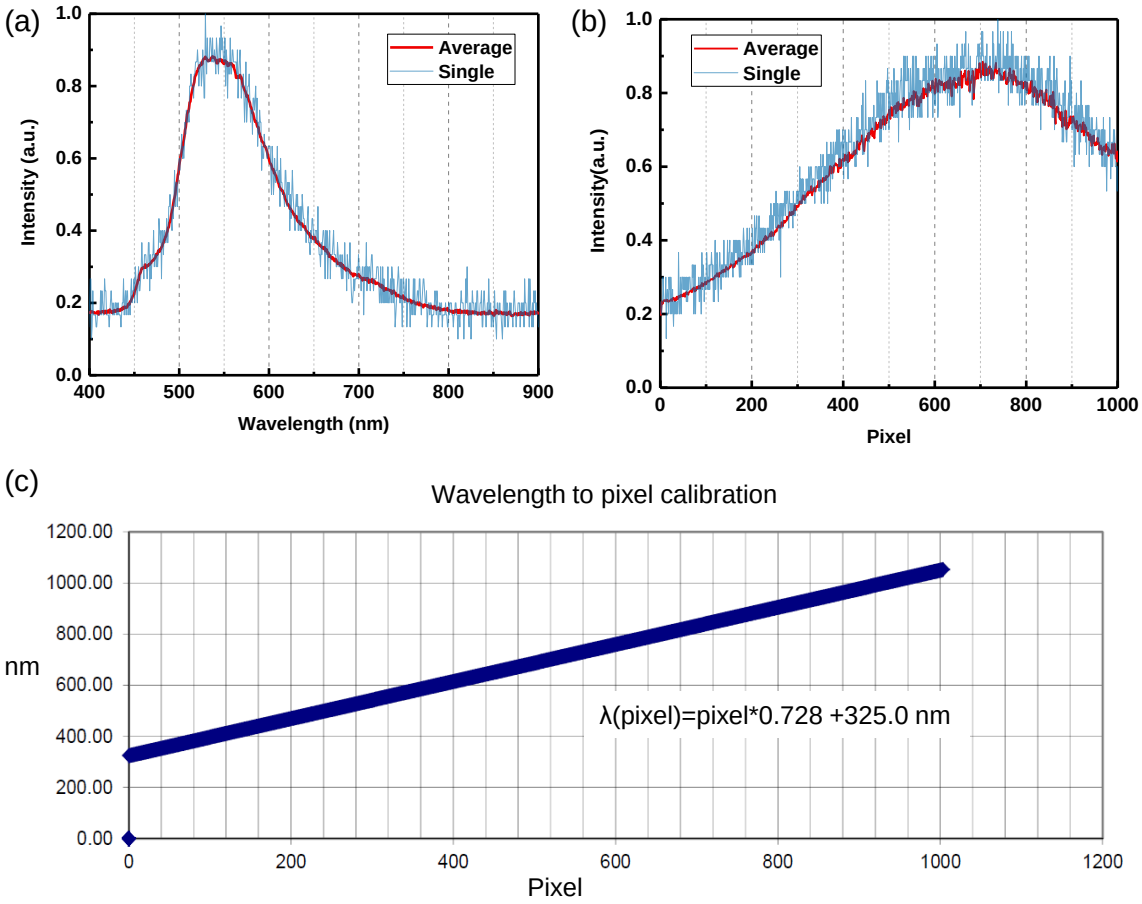

Figure 3.7: Measured reflected spectrum and the spectral response of the hyperspectral imager. (a) The single and averaged spectra of reflected light from the bare SiO_2/Si substrate. (b) The single and averaged intensity distribution of reflected light from the bare SiO_2/Si substrate along the slit direction. (c) The spectral response of the hyperspectral imager.

spectra of each pixel within the sample area were obtained. To control the movement of the stage along y-direction with the motorized line scan, two movement modes were designed. "Move relative" meant that the stage moved step by step, and the sample was scanned line by line. For every step, the reflected light from the sample was captured by the camera and recorded. "Move absolute" meant that the stage moved to the set position, and the camera captured no image, which was designed specifically to realize fast movements of the stage in searching for the region of interest before starting the line scan. When the region of interest was selected, the stage was controlled to scan and record the spectral information of all pixels using the designed GUI (Figure 3.9). To achieve high-speed scanning, the hyperspectral microscope was designed to work at the line-scan mode, which meant the spectrum of all the pixels along the line-shaped area

(5×80 µm^2) could be captured at one frame. The control software of the hyperspectral system was based on MATLAB. In this chapter, the parameters were controlled as follows, scanning speed as 100 µm/s, step size of 5 µm, the waiting time of 0.1 s for camera capture. The scanning time for a region of 200×80 µm^2 was 30 s. The acquired hyperspectral data set covered a range of 325-1056 nm.

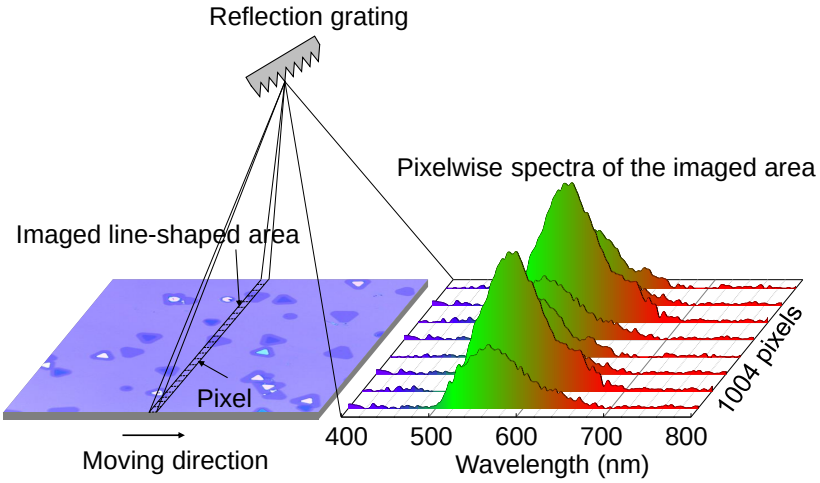

Figure 3.8: The schematic of pixelwise spectra acquisition of the whole scanned area by the line-scan hyperspectral imaging mciroscopy.

3.3 Hyperspectral Data Analysis

3.3.1 Conventional Analysis Methods

The hyperspectral data set is a three dimensional datacube which contains two spatial dimensions and one spectral dimension. The spatial information provides the localization and profiles of objects in the field of view, and the spectral information contains the unique features for property studies and components identification.

For the line-scan mode, hyperspectral data sets can be built by combining the spectral information line by line (Figure 3.10(a)-(b)). A hyperspectral data set contained spectral information of all the pixels of the scanned region. The hyperspectral data set can be described by:

$$p_k = [x_k, y_k, I_k(\lambda_1, \lambda_2, \ldots, \lambda_n)] \tag{3.1}$$

When the hyperspectral data set is obtained, three functions can be realized by direct operations of the data set. The first function is same as that of conventional RGB images

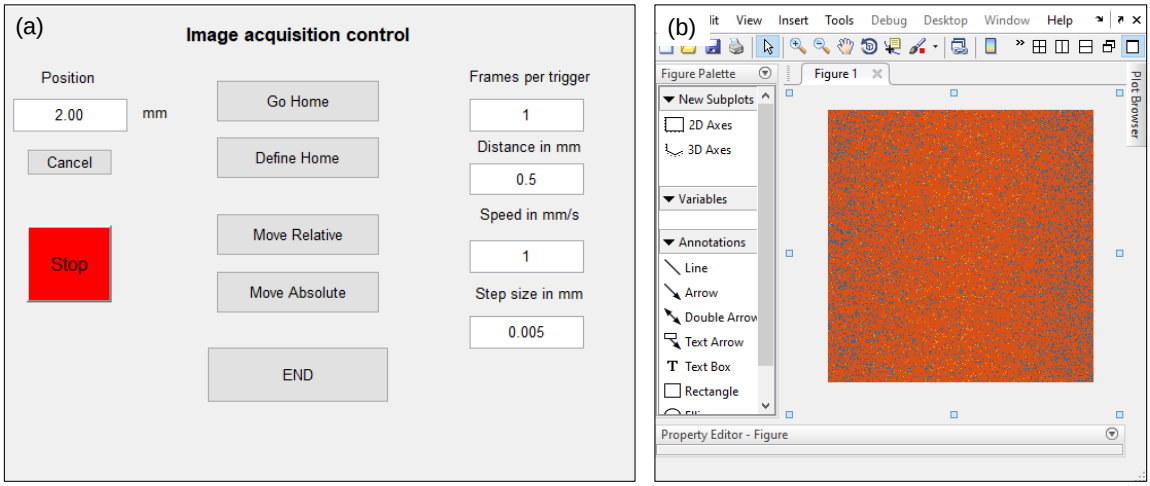

Figure 3.9: MATLAB user interface used for line-scan hyperspectral data acquisition. The left figure is the stage and camera control user interface, and the right figure shows the live spectral information of the scanned line.

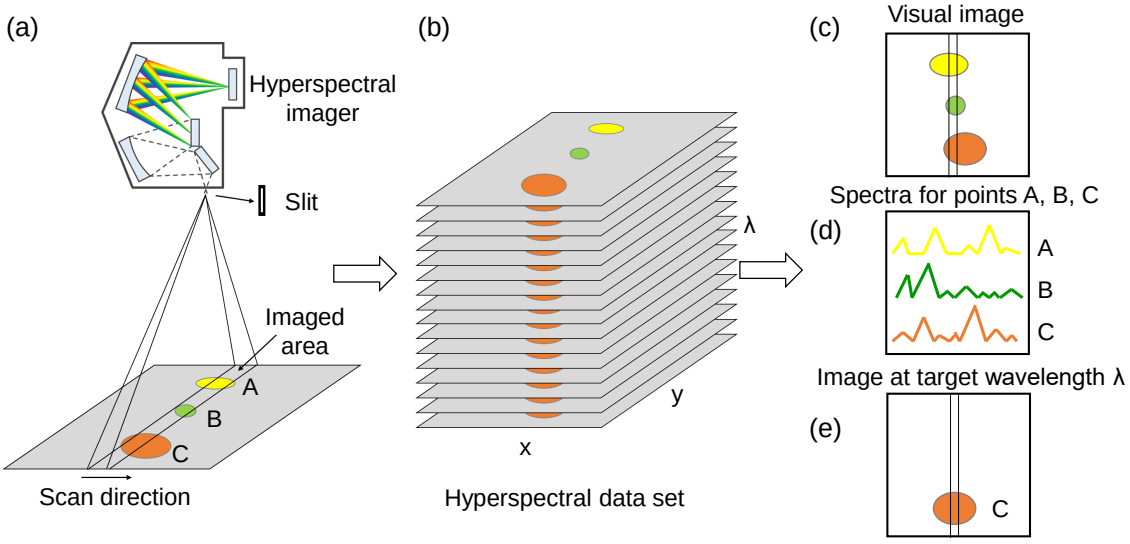

Figure 3.10: Multidimensional data set. (a) Image acquisition of the line-scan hyperspectral imaging microscope. (b) Hyperspectral data set with a size of $60 \times 1004 \times 1004$, which means that the camera captures 60 frames in one measurement and each frame consists of 1004 spectral channels and 1004 spatial pixels.

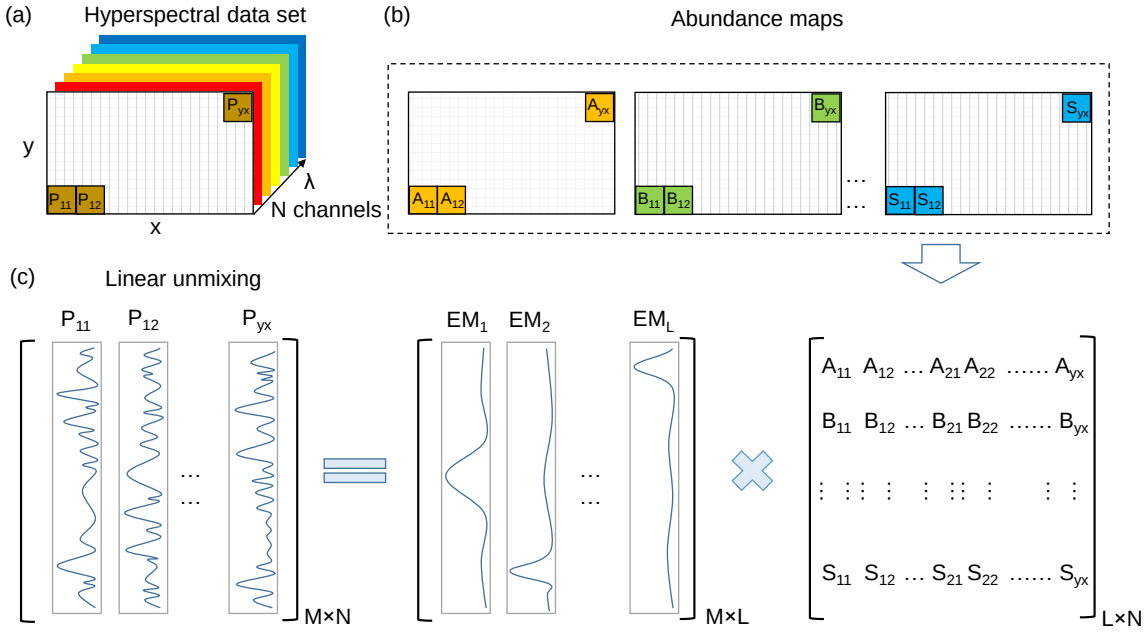

Figure 3.11: Linear unmixing of the multidimensional data set acquired by hyperspectral imaging microscopy. EM represents different end members.

to visualize the spatial distribution of all the objects (Figure 3.10(c)). The second function is the characteristic spectra extraction of different components. The representative spectra of A, B, and C objects can be extracted by averaging the lateral pixels (Figure 3.10(d)). Based on the extracted representative spectra, one composition can be visualized at some specific wavelengths to eliminate the influence from other compositions, which enables a better understanding of the light-matter interaction (Figure 3.10(e)). This function is called single-band analysis.

However, it is a normal case that the spectra of different compositions exist at the whole spectral range and no specific wavelength can be selected to visualize one composition. To further identify the components and visualize their distributions, multivariate analysis methods have been developed to deal with the spatially resolved spectroscopic information. Principal component analysis (PCA), vertex components analysis (VCA), and independent component analysis (ICA) are strong tools to extract the pure spectra (also called "end members") of different components and widely used for spectral unmixing of multidimensioanl data acquired by electron energy-loss spectroscopy and scanning transmission electron microscopy [224–226]. Another versitile method, multivariate curve resolution-alternating least squares (MCR-ALS), was applied to FTIR and Raman spectroscopic images to distinguish biological materials [227–229]. A hierarchical multivariate curve resolution method was developed to image the trace compounds with

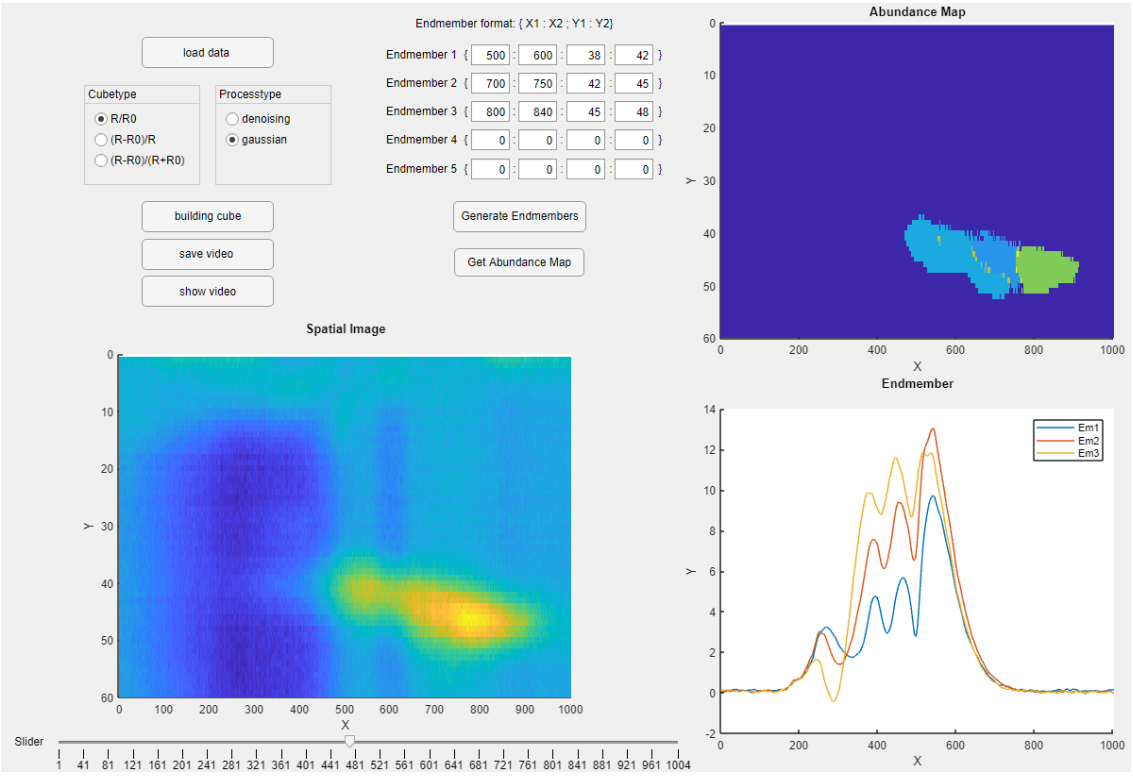

Figure 3.12: MATLAB user interface for hyperspectral data set analysis including single-band analysis, pixel-level spectral analysis, end member extraction, and abundance map reconstruction by linear unmixing.

low SNR [230]. These multivariate analysis methods can also be employed to deal with the spectral unmixing of hyperspectral microscopic images of 2D materials and 2D-based structures.

In this work, linear unmixing, a sub-class of spectral unmixing methods, was employed to calculate the abundance map (A_i) of different end members and estimate their contributions based on a linear relation between measured spectra and end members [231]. The contributions from the known end members were estimated by the least-square approximation. A primal-dual interior-point optimization method was used for linear unmixing calculation. The spectra of each pixel (I_k) could be considered a linear mixing of different pure spectra (I_i) which were extracted from pixels with only one object, shown in the Equation (3.2).

$$I_k(\lambda) = \sum_{i=0}^{n} A_i \times I_i(\lambda) \tag{3.2}$$

Here, I_i is called end member, and A_i, called abundance, is the contribution of the corre-

sponding end members.

Figure 3.11 illustrates the principle of linear unmixing for estimating the abundance maps of end members. With the acquired hyperspectral data set and the extracted end members, the abundance map of these end members could be calculated and the distribution could be visualized [232]. Based on the previsously developed linear unmixing method [233], the algorithms were adapted in our case to process the hyperspectral data set acquired by the measurement system. The algorithms worked in MATLAB environment, and a GUI was developed to conduct single-band analysis, pixelwise spectra extraction, and thickness distribution calculation using linear unmixing (Figure 3.12).

3.3.2 Machine Learning Methods

Artificial intelligence (AI), machine learning (ML), and deep learning (DL) are functioning all over the places in human daily life and they are bringing great changes in technological fields to automate the system for higher efficiency and better performances. Machine learning is one way to realize artificial intelligence, while deep learning is a sub-field of machine learning and it can provide great advantages in addressing traditional computer vision challenges such as object detection, localization, segmentation. One important factor to realize these tasks is to extract the unique features between different objects and between the object and the background. Previously, the conventional hand-crafted methods are largely dependent on the feature quality finished by the domain experts. The advantage of machine learning is automated feature learning, which reduces human participation in feature extraction.

Here, machine learning categories including supervised learning, unsupervised learning, semi-supervised learning are introduced. These categories are different according to the tasks, input data, and output data. Supervised learning uses labeled data as desired network output. The parameters of the network are optimized during training process to output results as much as similar to the labeled data. Unsupervised learning is used to find the characteristics of unlabeled input data. Common methods of unsupervised learning are principal component analysis and cluster analysis. Semi-supervised learning is one category between supervised learning and unsupervised learning, with a limited number of labeled data and a large amount of unlabeled data. These machine learning methods are suitable for specific tasks according to the availability of labeled data.

Figure 3.13(a) shows a simple example of the neural network architecture, where the neural network is constructed from three types of layers including an input layer, hidden layers, and an output layer respectively. Figure 3.13(b) illustrates the mathematical relation of inputs and outputs in one neuron of the network. The inputs (x_1, x_2) are

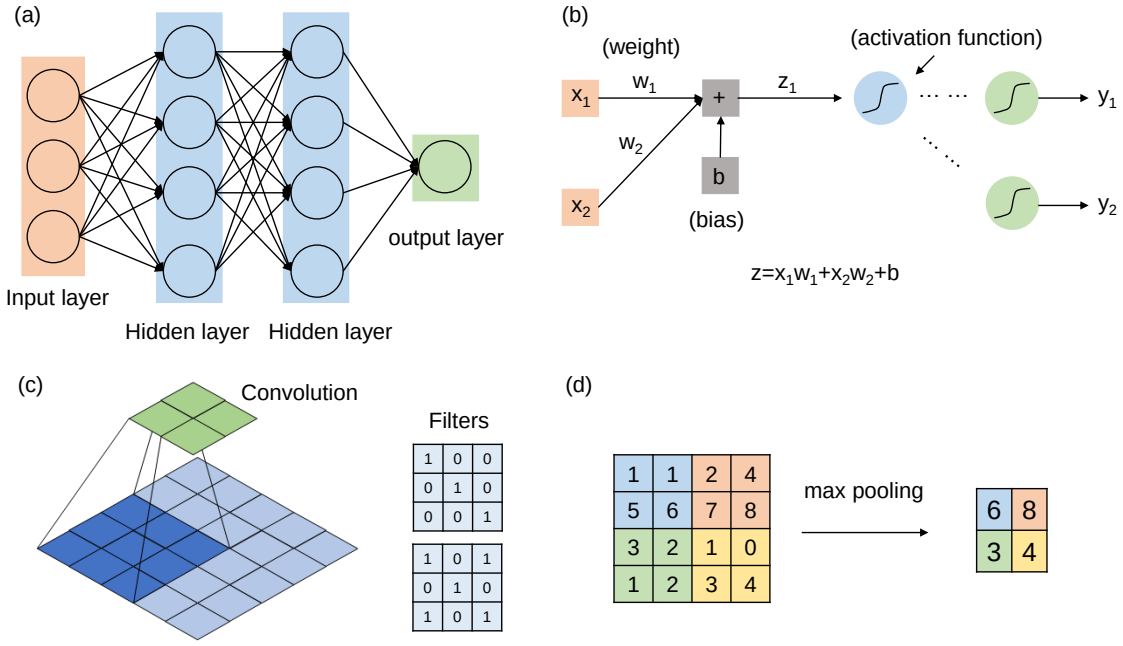

Figure 3.13: Machine learning basics. (a) A fully connected neural network. (b) A simplified neuron from the network. (c) Principle of convolution. (d) Principle of max pooling.

multiplied by two weights (w_1, w_1), and the calculated value is added by the bias (b_1) to get z_1. An activation function is employed get the output of the neuron (y_1, y_2). The outputs of one neuron are used as the inputs of the following neurons until the final outputs of the network. In this thesis, a convolutional neural network (CNN) is employed for image processing of 2D materials, and therefore, the mathematical operations of the layers of CNN network, convolution and max-pooling, are introduced in Figures 3.13(c)-(d). The features of one image matrix can be extracted by convolution operation with filters (kernels), which is usually followed by pooling operations. There are different pooling operations such as average pooling which calculates the average value of each patch and max-pooling which calculates the maximum value of each patch. The dimensions of the data can be reduced by pooling operations to extract the average or largest values of small clusters. In the network training process, backpropagation is used to calculate the local gradient of the loss function, to minimize the loss, and to update the parameters of each layer of the network (gradient descent). Backpropagation is widely used in supervised learning.

Machine learning has been applied to four types of computer vision tasks including image segmentation, classification and localization, semantic segmentation, and instance segmentation, with the goals of tasks shown in Figure 3.14. For image classification, the

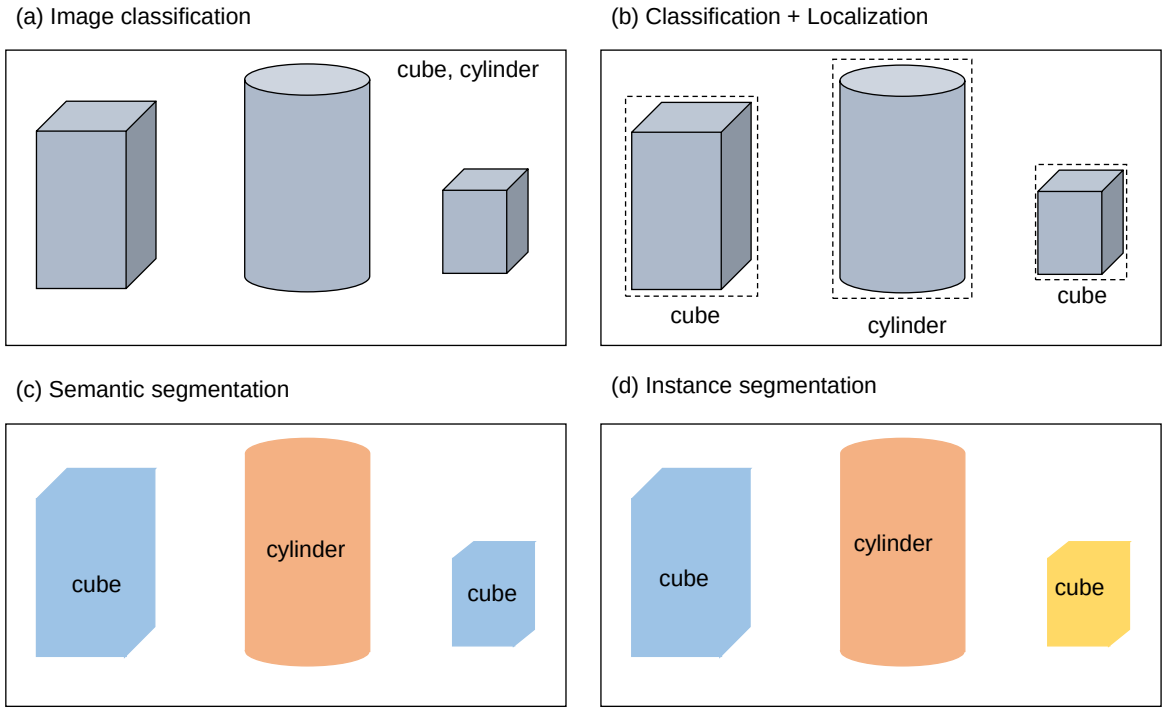

Figure 3.14: Deep learning applications in computer vision tasks.

input of the neural network is a picture and the output is a single class label; while segmentation is pixelwise classification, where each pixel is labeled as a single class and the pixels with the same class are classified as one type. Localization is used to label the position of each classified object.

CNN is usually used in image classification tasks such as dog and cat classification. Figure 3.15 demonstrates the basic structure of CNN. Through a series of convolutional layers, pooling layers, and fully connected layers, different features are extracted from low to high level by CNN. That means, every hidden layer increases the complexity of the learned image features. The network outputs a vector to classify the input into one sub-class.

There is a specific type of convolutional neural network named fully convolutional networks (FCNs) for image segmentation tasks. Different from image classification tasks conducted by CNN which outputs only one class, FCN outputs a picture with the same size as the input picture, and each pixel of the input picture is labeled with a single class. In another word, classification only needs to understand what is in the input, segmentation needs to recover not only what is in the input, but also where these subjects are. Developed from CNN, FCN uses the same convolution layers in the encoder stage, but uses deconvolution layers in the decoder stage instead of fully connected layers in CNN. Therefore, the semantic segmentation can be realized by classifying each pixel of

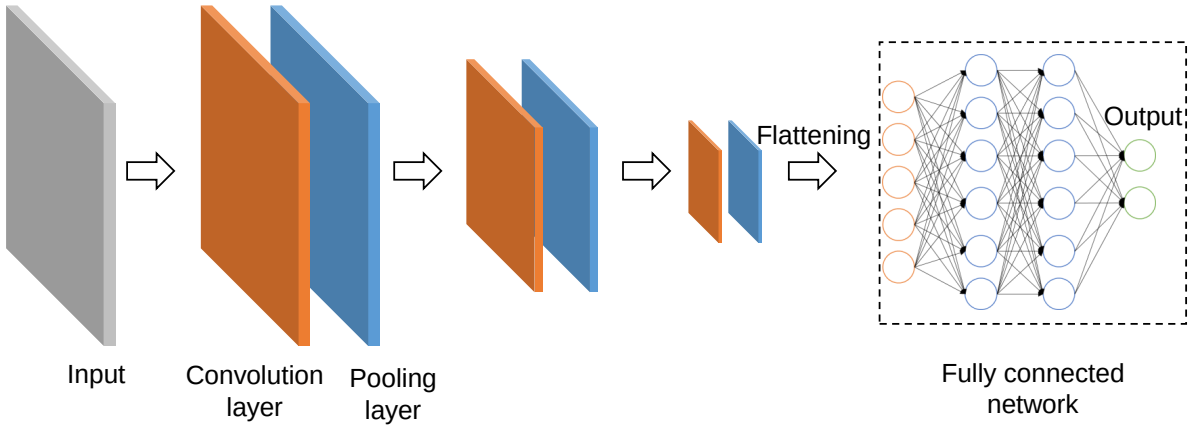

Figure 3.15: Architecture of CNN with encoder-decoder structure.

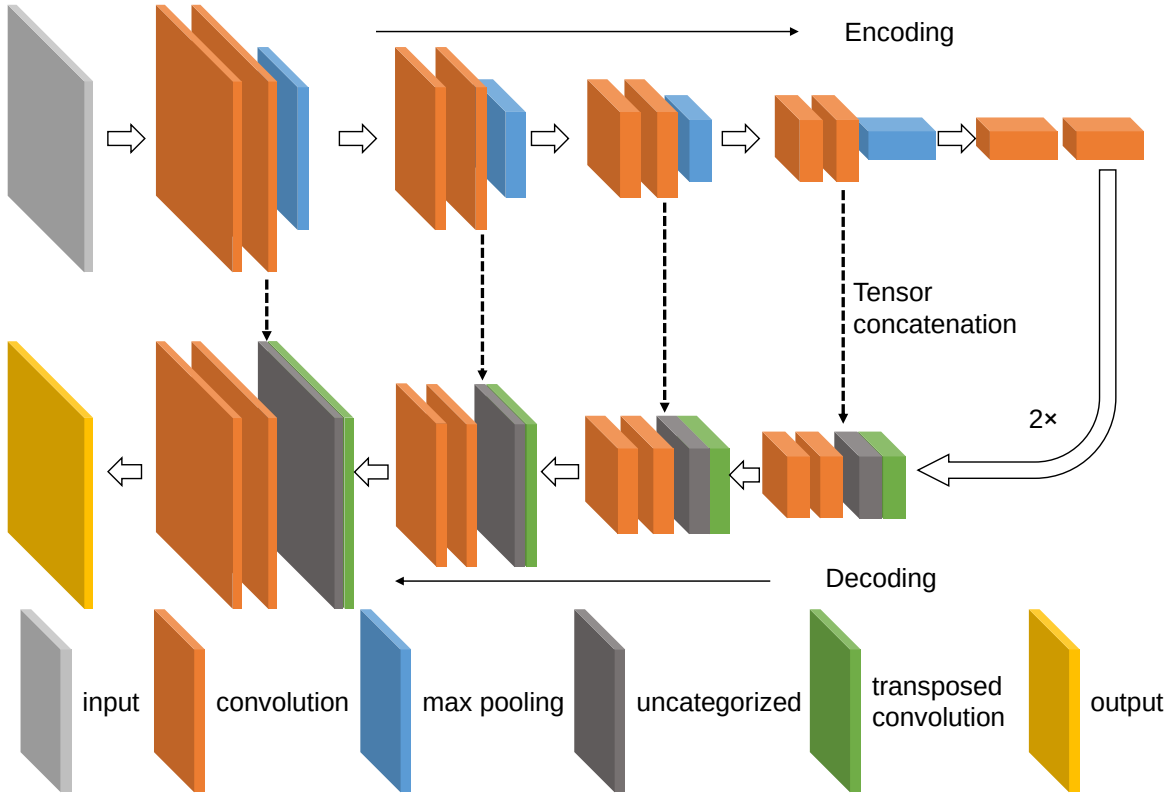

Figure 3.16: U-Net Architecture.

the image into one-subclass. Figure 3.16 shows the architecture of U-Net, which is composed of a contraction section (downsampling path) and a expansion section (upsampling path). The contraction section includes convolution layers and max pooling. Through the downsampling path, the context (the type of subjects) information can be extracted and interpreted. The expansion section consistes of concatenation, convolution, and upsampling layers. Through the upsampling path, the precise localization information (the position of subjects) can be acquired.

In machine learning tasks for image processing, there are also such cases where the same sample needs to be measured by two or more modalities, because these modalities can provide useful information from different perspectives and no one can replace another function. Fusion networks have been applied to many applications such as remote sensing (multispectral and hyperspectral imagery fusion), super-resolution, and medical imaging. To better use the data from dual- and multi-modal modalities, a fusion network is normally employed to combine the multi-modality information and output one combined image which possesses the advantages of all the inputs. A deep fusion network for image segmentation is conducted in Chapter 6, and the structure of image fusion is shown in Figure 3.17. Convolution and pooling operations are conducted separately in two input streams, and the extracted features from both encoders are fused, followed by one decoder stream as the upsampling path. The network recovers better vision of both inputs.

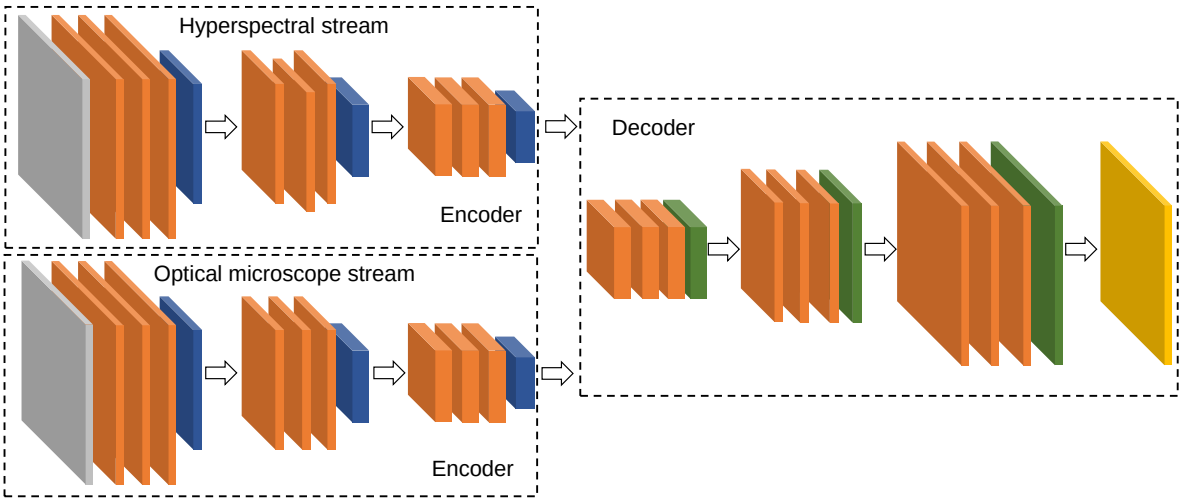

Figure 3.17: Architectures of stream-fusion segmentation used in this work.

3.4 Summary

This chapter introduces the principles of hyperspectral imaging and the multidimensional data set processing methods. For layer number identification of 2D materials, a line-scan

hyperspectral imaging microscope system including a hyperspectral imaging microscope, system control, data acquisition GUI, and the manual data processing GUI, was custom built and calibrated. The control and image acquisition of the system work in the MATLAB environment. The microscale spatial resolution of the line-scan hyperspectral imaging microscope (horizontal resolution better than 228 lp/mm and vertical resolution of 5 µm/pixel) is sufficient for the characterization of distinct micron-sized 2D flake areas, considering that the sizes of few-layer and monolayer crystals are several to tens of microns in the lateral dimension. The hyperspectral data set processing will be based on the discussed spectral unmixing method and U-Net neural network in Chapters 4, 5, and 6.

Chapter 4

Pixelwise Hyperspectral Data Interpretation and Classification

To process and interprete the hyperspectral data sets acquired by the system, a comparative study was conducted to process the multidimensional data sets including abundance mapping based on linear unmixing calculation, and peak intensity and peak position mapping based on differential reflectance spectra. Multi-layer MoS_2 flakes fabricated on the SiO_2/Si substrate with 100 nm oxidation film was employed as demonstration. The performances of both strategies to identify the flakes of different thicknesses and to extract the spectral features were compared in detail, especially the accuracy after denoising, smoothing, and extracting of pixel-level spectra. The main work of this chapter is to develop an effective multivariate data analysis method with GUI.

4.1 Workflow of Spectral Unmixing and Peak Position Mapping

Figure 4.1 illustrates the process of thickness mapping for 2D semiconducting flakes using hyperspectral imaging microscopy combined classification strategies including linear unmixing and spectral peak mapping. The MoS_2 flakes fabricated on a SiO_2/Si substrate with 100 nm thick SiO_2 by mechanical exfoliation were measured to acquire the spectral data set of the region of interest (Figure 4.1(a)) [234]. The preprocessed hyperspectral data set was analyzed by two methods, linear unmixing (pure spectra extraction and abundance estimation) (Figure 4.1(c)) and peak position mapping after peak position search (Figure 4.1(d)) to obtain the thickness distribution of the sample (Figures 4.1(e)-(h)).

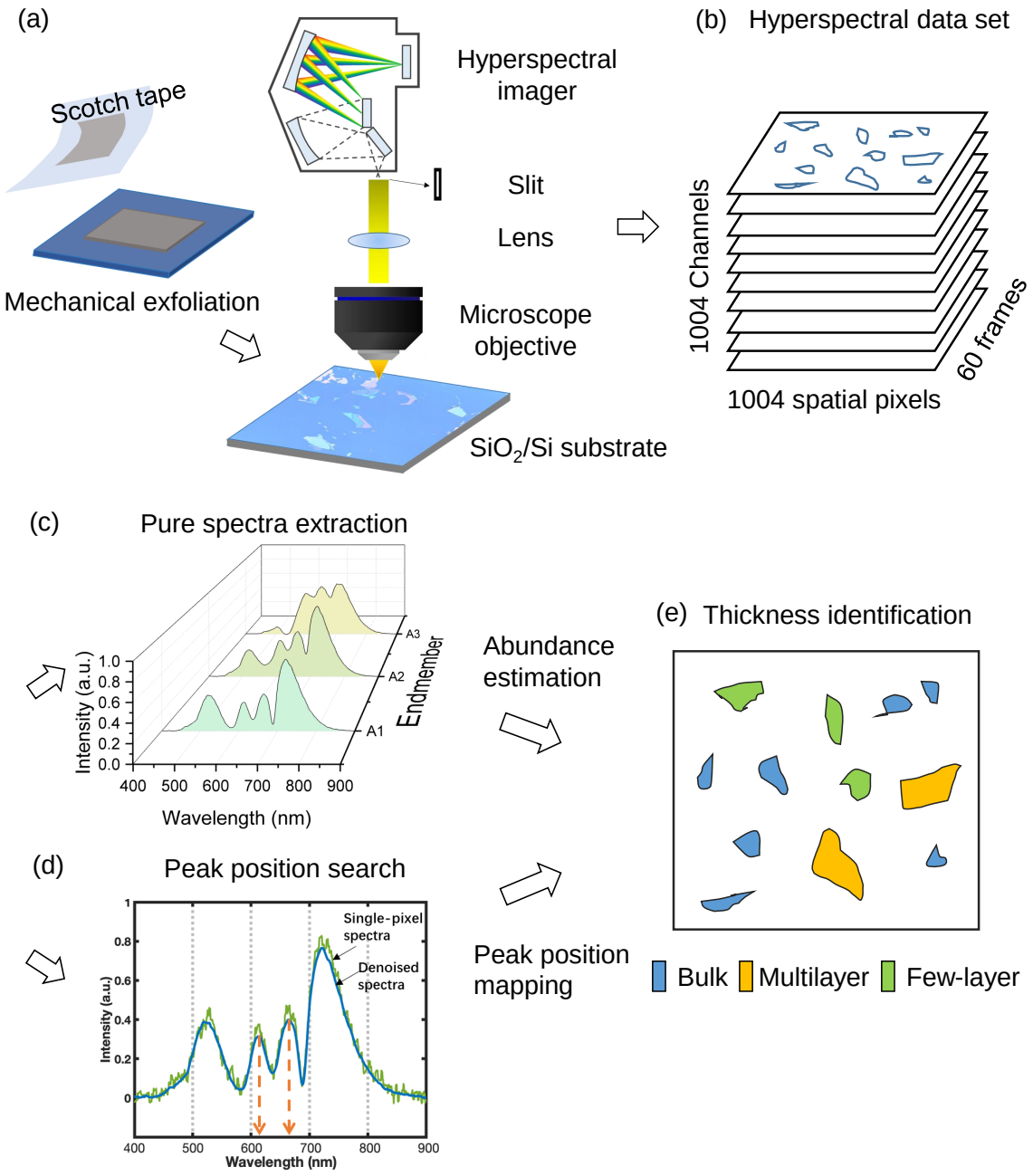

Figure 4.1: The whole process of 2D semiconducting flakes thickness mapping using hyperspectral imaging microscopy and two different classification strategies. (a) Sample fabrication and hyperspectral data set acquisition. (b) Hyperspectral single-band analysis. (c) Pure spectra extraction as end members. (d) Single-pixel spectra smoothing, denoising, and peak searching. (e) The reconstructed maps of flakes with different thicknesses.

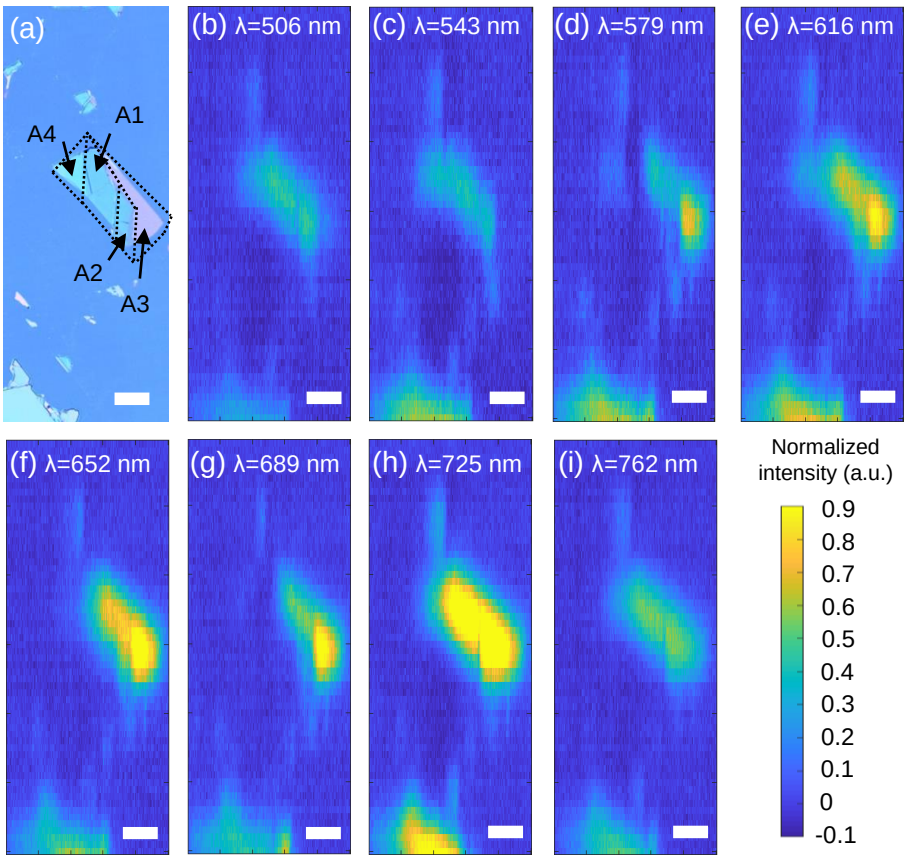

Figure 4.2: The reconstructed images of the region of interest from the hyperspectral data set at different wavelengths, with (a) the optical image as a reference.

4.2 Hyperspectral Reflection Measurements

The sample was fabricated by mechanical exfoliation with Scotch tape from bulk MoS_2 (2D Semiconductors Inc.) on a single-polished SiO_2/Si substrate with 100 nm thick SiO_2 coating (Microchemicals GmbH). The prepared sample was observed using an optical microscope (Leica) to select the flakes with different thicknesses. Figure 4.2(a) illustrates an optical microscope image of the sample with different thicknesses. The different thicknesses of MoS_2 flakes in this area were distributed into four parts. This sample was moved to the stage of custom-built hyperspectral imaging system for spectral scanning. A 3D datacube containing the spectrum of every point within the area was built. To obtain the correlation of spatial thickness distribution of the flakes with varying wavelengths, single-band analysis of reflectance intensity was conducted. Gaussian smoothing was first used to minimize the noise from the environment. Considering the reflection from the SiO_2/Si substrate, the intensity distribution of the reflected light from the bare substrate was measured by averaging the spectra of five frames.

The intensity distributions of single-band images can be calculated by:

$$R_{intensity} = R\left(i, j, \lambda\right) - R_0\left(i, j, \lambda\right) \tag{4.1}$$

where $R_{intensity}$(i, j, λ) is the calculated intensity distribution of pixel (i, j) at wavelength λ, R(i, j, λ) is the measured reflection spectra of every pixel, and R_0(i, j, λ) is the averaged spectra from the bare substrate.

After an elimination of the influence from the substrate, the intensity images of the area over a wavelength range of 400-700 nm were obtained and the spatial intensity change in a spectral view was analyzed. The spatial images at 506 nm, 543 nm, 579 nm, 616 nm, 652 nm, 689 nm, 725 nm, and 762 nm, are shown in Figures 4.2(b)-(i). These images were reconstructed from the acquired hyperspectral data set by background subtraction (R-R_0 calculation, R_0 was the reflected light from the bare substrate, and R was the reflected light from the flakes). The variables (x, y, I) of the 3D data set were $60 \times 1004 \times 1004$, which meant that the camera captured 60 frames in one measurement and each frame consisted of 1004 spatial pixels and 1004 spectral channels. To eliminate the influence of inhomogeneous illumination, the spectra of the substrate were excluded from the original 3D data set.

4.3 Feature Extraction and Pixelwise Classification

Two quantitative pixelwise classification strategies including linear unmixing and spectral peak mapping were conducted to characterize the multi-layer semiconducting MoS_2 flake with nanoscale thickness variations. A competitive study was conducted to choose one method with better pixelwise classification performances.

4.3.1 Thickness Mapping with Spectral Unmixing

Figure 4.3 illustrates the characteristic spectra (end members) of the regions with different thicknesses The thickness distributions of the MoS_2 flake on the SiO_2/Si substrate could be observed over the full wavelength range (400-700 nm) by the spatial variations of the single-band images. Based on the observation of the spatial images, different regions could be located. The represetative spectra (end members) of the regions (A1-A4) were obtained by averaging the spectra of pixels in these regions, which was conducted in a MATLAB graphical user interface (Figure 3.12).

After the end members were extracted, linear unmixing was used to estimate the contributions (abundance) of different components (end members) based on the full-range

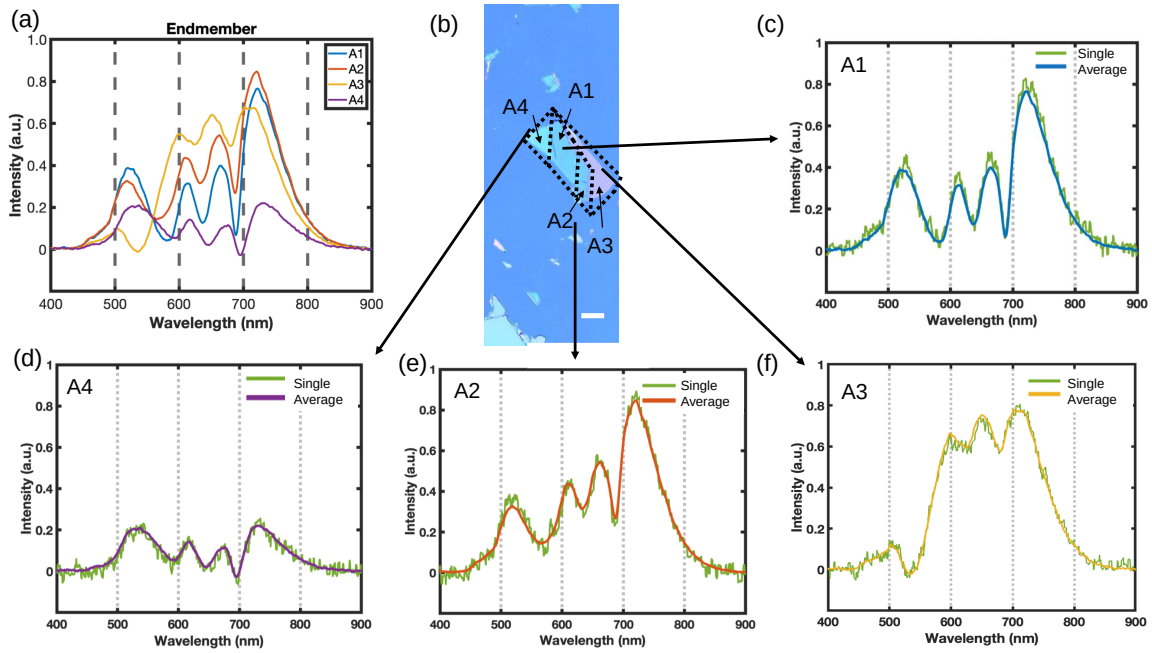

Figure 4.3: The extracted end members of the four regions with different optical contrast. Scale bar= 20 µm.

spectra of pixels. The reflected intensity was considered a combination of intensities from different end members [235]. When the reflection intensity $I_k(\lambda)$ and the end members $I_i(\lambda)$ were known, linear unmixing was employed to calculate the abundance of different end members:

$$\frac{\partial \sum_j \{I_k(\lambda_j) - \sum_i A_i I_i(\lambda_j)\}^2}{\partial A_i} = 0 \tag{4.2}$$

To estimate the contributions from the known end members by least-square approximation, a primal-dual interior-point optimization method was used. In the process of estimation, physical constraints including non-negativity ($A_i \geq 0$, i=0, 1, 2,..., n), sum less than one($\sum_{i=0}^{n} A_i$<1), and sum equal to one ($\sum_{i=0}^{n} A_i = 1$) were required. In this case, non-negativity and sum less than one were set as the constrains for linear least squares in abundance calculations.

As compared with the optical image (Figure 4.4(a)) using a conventional microscope (50× magnification), Figures 4.4(b)-(c) show the abundance maps of four end members after linear unmixing, before and after applying spatial-spectral denoising [236]. Different regions were illustrated in false colors, representing the contributions from different end members. In Figure 4.4(c), it is depicted that denoising of the multidimensional data sets reduced the influence of the substrate, realizing improved recognition of the flake

areas from the SiO_2/Si substrate. The contributions of different end members were not affected before and after denoising. The percentage of different regions were calculated by classifying labelled pixels (Figure 4.4(d)). Linear unmixing had the function of filtering, where the pixels with different spectra from the extracted end members were classified as background. Hence, the small flakes present in Figure 4.4(a) were not segmented in Figures 4.4(b)-(c).

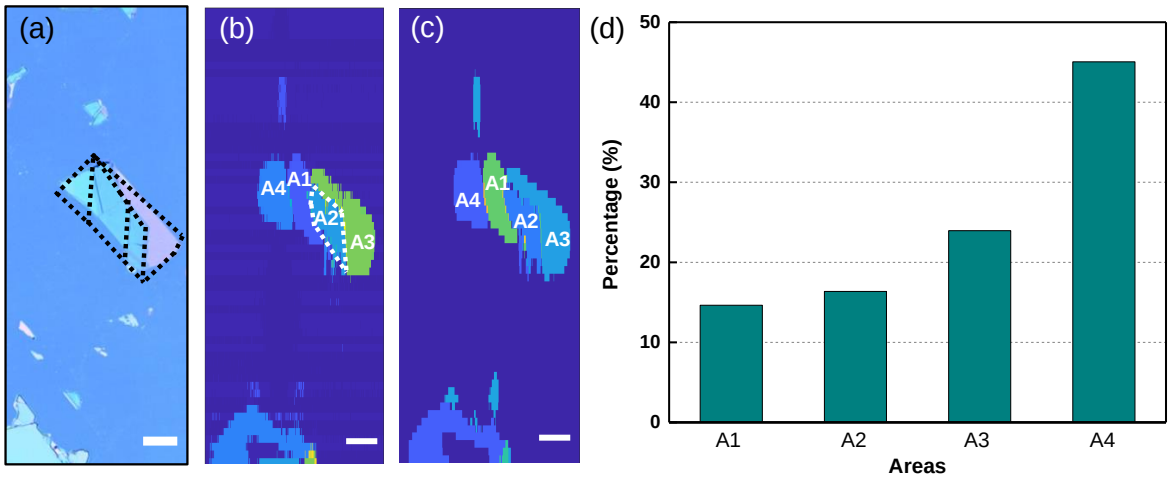

Figure 4.4: The pixelwise classification results using linear unmixing. (a) The optical microscope image of the region of interest. (b) The abundance map with end members (Figure 4.3(a)) without denoising. (c) The abundance map with end members (Figure 4.3(a)) after denoising. (d) The statistical information of different thicknesses among the whole sample area. Scale bar= 20 µm.

4.3.2 Thickness Mapping with Peak Positions

The second method, peak position mapping, was used to obtain the thickness distribution of different flakes based on the exciton peak features. Optical feature extraction through differential reflectance analysis is a widely used method which can realize precise determination of components. Former studies have revealed the A, B, and C type excitonic peaks of differential reflectance spectra of semiconducting 2D materials in the visible range [237]. When the thickness increases from monolayer to few-layer, and to multi-layer, excitonic peak positions shift based on the thickness variation. An automatic peak position search for all single-pixel spectra in the spectral domain was conducted within the observed region of different layer numbers. The successfully found peak positions were mapped in false colors. Figure 4.5 shows the mapping results based on the differential reflectance analysis of multidimensional data sets. Both A and B excitonic features were used for peak position mapping. The A and B excitonic peak intensity mapping are shown in

Figure 4.5(a)-(b), respectively. The A and B excitonic peak position mapping are shown in Figure 4.5(c)-(d), respectively, with Figure 4.5(e) as the reference. The corresponding single spectra from different areas are shown in Figure 4.5(f). The spectra of one pixel extracted from the c area in Figure 4.5(a) after Gaussian smoothing and denoising are shown in Figure 4.5(g). The peak position and peak intensity of one spectra after Gaussian smoothing and denoising had subtle changes. Spectral noises induced in the measurement process can lead to random minor peaks of the spectra and peak position shift of single-pixel level spectra. To lower such influence, all single-pixel spectra were denoised by a spatial-spectral total variation minimization method. Furthermore, measurement uncertainty in peak positioning cannot be totally averaged by the Gaussian smoothing function due to the noise induced in the single-pixel spectra. To reduce the uncertainty of peak positioning, a combination of peak positions and peak values was used for the determination of areas with different thicknesses. The areas within the MoS_2 flake can be distinguished according to the peak position features (Figure 4.5(c)-(d)). The original influence induced in the measurement process can affect the imaging performances such as the recognition of edges of the flake (Figure 4.5(a)-(b)). By comparing the exciton peak positions with the previously-reported results [198, 238], the thicknesses of the MoS_2 flakes can be roughly estimated using the popular optical contrast method. The B exciton peak position range from 616 nm to 624 nm, and the thickness of the flakes should be larger than 10 layers and the flakes are identified as multi-layer. The main goal of this work is to verify the capability of the hyperspectral data set analysis methods. Validation for thickness determination using atomic force microscopy or Raman spectroscopy are needed when studying monolayer, bilayer, and few-layer 2D materials.

In addition to differential reflectance spectra analysis, optical contrast analysis is also widely employed to study the optical response properties of 2D TMDs. The multidimensional data set was processed by optical contrast analysis. According to the spectra of extracted characteristic pixels, the A and B excitonic peaks were not clearly shown as compared to those of differential reflectance calculations (Figure 4.6(b)). Therefore, the spatial mapping by optical contrast analysis is not shown here. Peak position mapping by spectral features of differential reflectance spectra and optical contrast was theoretically based on the correlation between thin-film thickness and the featured peak position. However, the induced noise can influence the automatic searching of meaningful peaks. The utilization of smoothing and denoising methods which can eliminate the noise without peak shifts can improve the accuracy and imaging performance.

Hyperspectral image classification strategies including linear unmixing and exciton peak position mapping are used to reconstruct the thickness distribution of MoS_2 flakes. For linear unmixing, the least-squared calculation is based on the single-pixel spectra over the

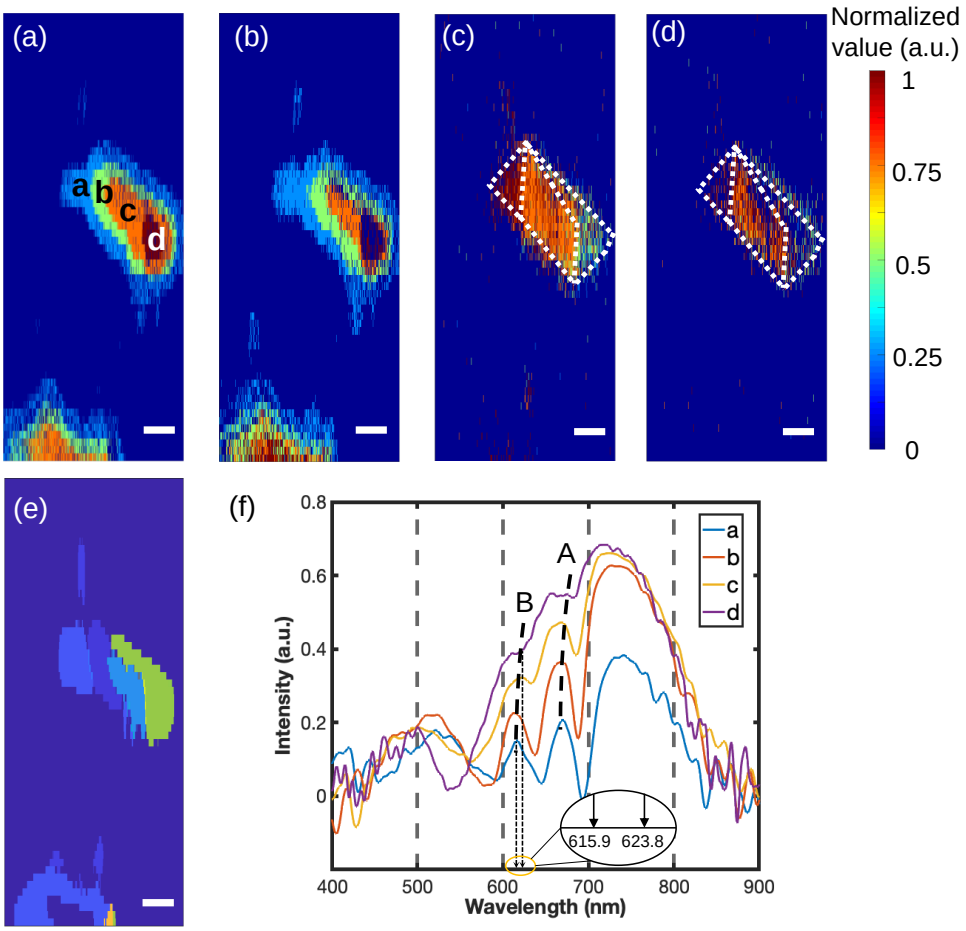

Figure 4.5: Analysis of the MoS_2 flakes with different thicknesses by peak position mapping. (a) Peak intensity mapping of A excitonic peak after the spatial-spectral denoising and Gaussian smoothing. (b) Peak intensity mapping of B excitonic peak after the spatial-spectral denoising and Gaussian smoothing. (c) Peak position mapping of A excitonic peak after the spatial-spectral denoising and Gaussian smoothing. (d) Peak position mapping of B excitonic peak after the spatial-spectral denoising and Gaussian smoothing. (e) The abundance map by linear unmixing as the reference (Figure 4.4(c)). (f) The differential reflectance spectra of different areas of the flake. Scale bar= 20 µm.

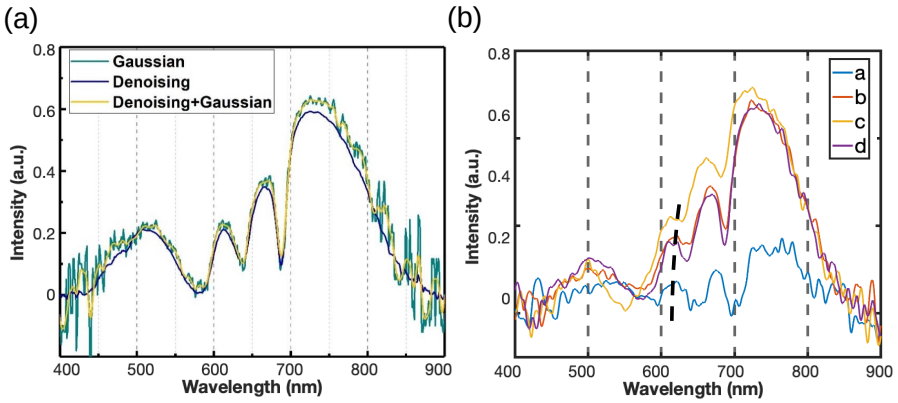

Figure 4.6: Analysis of the MoS_2 flakes with different thicknesses by peak position mapping. (a) The differential spectrums of one pixel in c area before and after spatial-spectral denoising and Gaussian smoothing. (b) The extracted spectra from different areas by optical contrast.

full wavelength range instead of the peak position or peak intensity. The influence of random noises on the performance can be lower than that of differential reflectance analysis. Therefore, the linear unmixing can provide the best image classification performance and evaluate the influence from the lateral regions. The limitation of linear unmixing strategy is that the end member selection can be largely determined by the researcher based on the single-band analysis and principal component analysis. This limitation can be further overcome by building a spectra library and using machine-learning-assisted determination. For exciton peak position mapping based on differential reflectance, the accuracy of peak intensity mapping is less than that of peak position mapping. Peak position mapping can provide spatial distribution of regions with different thicknesses, when the influence of noises on peak position searching is well dealt with by smoothing or denoising. Differential reflectance analysis based on exciton shifts can achieve quantitative thickness mapping which cannot be realized by the current scanning microscopes.

4.4 Summary

To process and understand the multidimensional data sets of semiconducting MoS_2 flakes acquired by the custom-built hyperspectral imaging microscope, two classification strategies including linear unmixing analysis, and differential reflectance and optical contrast analysis, were used to determine the spatial distribution of different areas with varying thicknesses. The comparative study proved the linear unmixing a promising tool for accurate thickness mapping. Additionally, the line-scan hyperspectral imaging microscopy with the linear unmixing possesses high speed for hyperspectral data set acquisition and

high spectral resolution (0.726 nm/pixel) to distinguish subtle spectral differences. Future studies focusing on the end member extraction of monolayer, bilayer, to few-layer semiconducting 2D materials and the abundance estimation, and the evaluation of the imaging performances, will be shown in Chapter 5.

Chapter 5

Hyperspectral-fingerprints-based Atomic Layer Mapping

In chapter 4, linear unmixing was proven an effective method to reconstruct the layer maps of 2D materials, to further investigate the suitability and robustness of the system, a step-by-step analysis including single-band analysis, pixel-level spectral analysis, and image reconstruction, was conducted onto 2D MoS_2 and hBN crystals (mono- and few-layer) prepared by micromechanical exfoliation. To further test the identification limit of the method, the spectral fingerprints of all the flake categories (monolayer, bilayer, trilayer, multi-layer, and bulk) of a reference MoS_2 sample were extracted to form a hyperspectral library. The library was implemented to quantitatively identify and map the distribution of distinct flakes from a new MoS_2 sample.

5.1 Layer Mapping of Mono- and Few-layer MoS_2

5.1.1 Spectral Unmixing for Atomic Layer Mapping

The workflow of the automated identification of 2D flakes by hyperspectral imaging microscopy and linear unmixing is presented in Figure 5.1. Briefly, the region of interest was scanned by the motorized stage while lines of spectra were recorded and assembled in a three-dimensional data cube. For each pixel, which represents a certain spot on the sample, the recorded spectrum was compared to a so-called end member spectrum. These spectra were those of flakes of known thickness. The comparison was done numerically by least-square approximation. Because the intensity and spectral contribution are recorded and numerically processed at each spot on the sample, an unambiguous identification

of layer thickness is possible, which is a distinct advantage compared to conventional RGB-type optical analysis [239].

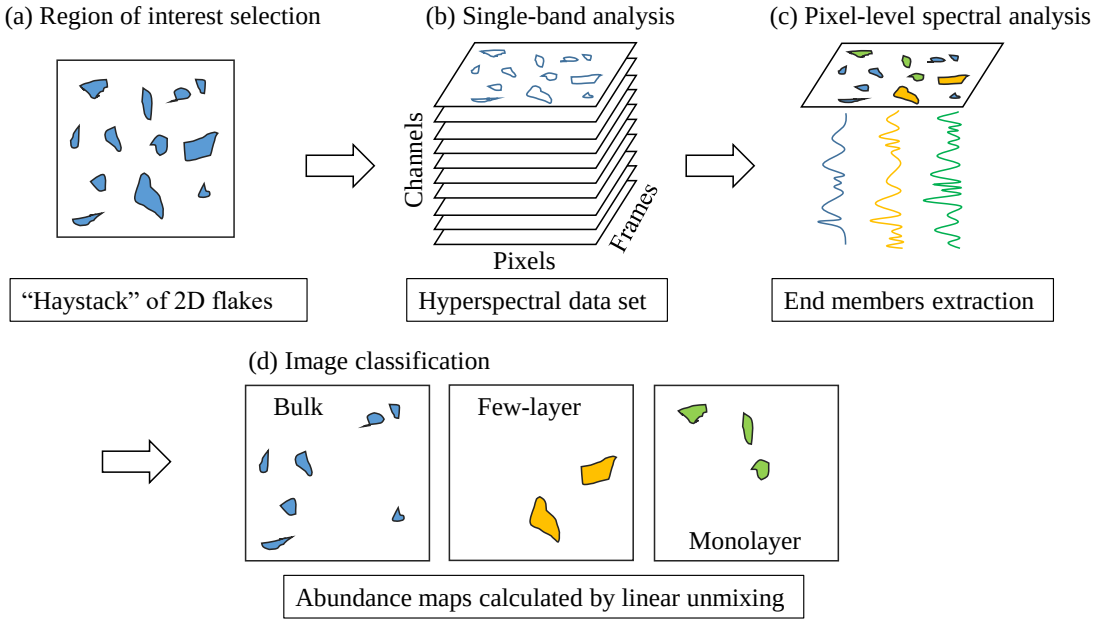

Figure 5.1: The principle, setup, and results of hyperspectral imaging microscopy with linear unmixing for automated 2D materials identification. The workflow of automated identification of monolayer and few-layer 2D flakes using hyperspectral imaging microscopy combined with linear unmixing.

5.1.2 Hyperspectral Measurement and Thickness Map Reconstruction

The MoS_2 sample with the SiO_2/Si substrate with 70 nm thick SiO_2 was observed using a conventional microscope and a region with a monolayer MoS_2 flake was chosen and scanned by the custom-built hyperspectral imaging microscope. Figure 5.2(a) illustrates the optical microscope images showing the distribution of all the flakes within a scanned region (120×330 µm^2). A-G were used to label different flakes including bulk, few-layer, and monolayer MoS_2. The monolayer flake (3 µm^2) with bulk and few-layer flakes around was found with the same objective with 100× magnification (the inset of Figure 5.2(a)). Figures 5.2(d)-(i) show the single-band images of the scanned region at specific wavelengths of 510 nm, 528 nm, 557 nm, 572 nm, 587 nm, 608 nm, separately. The intensities of flakes with different thicknesses varied with the changing wavelength, which provided a way of classifying different flakes. By comparing the hyperspectral images at different wavelengths, the flakes from multi-layer to bulk were roughly identified as compared to the images acquired by the conventional microscope. The monolayer MoS_2

(flake G in Figure 5.2(a)) can be distinguished in Figures 5.2(g)-(i), even though the signal detected by the camera was relatively lower than that of other flakes, due to the small size of the monolayer MoS_2.

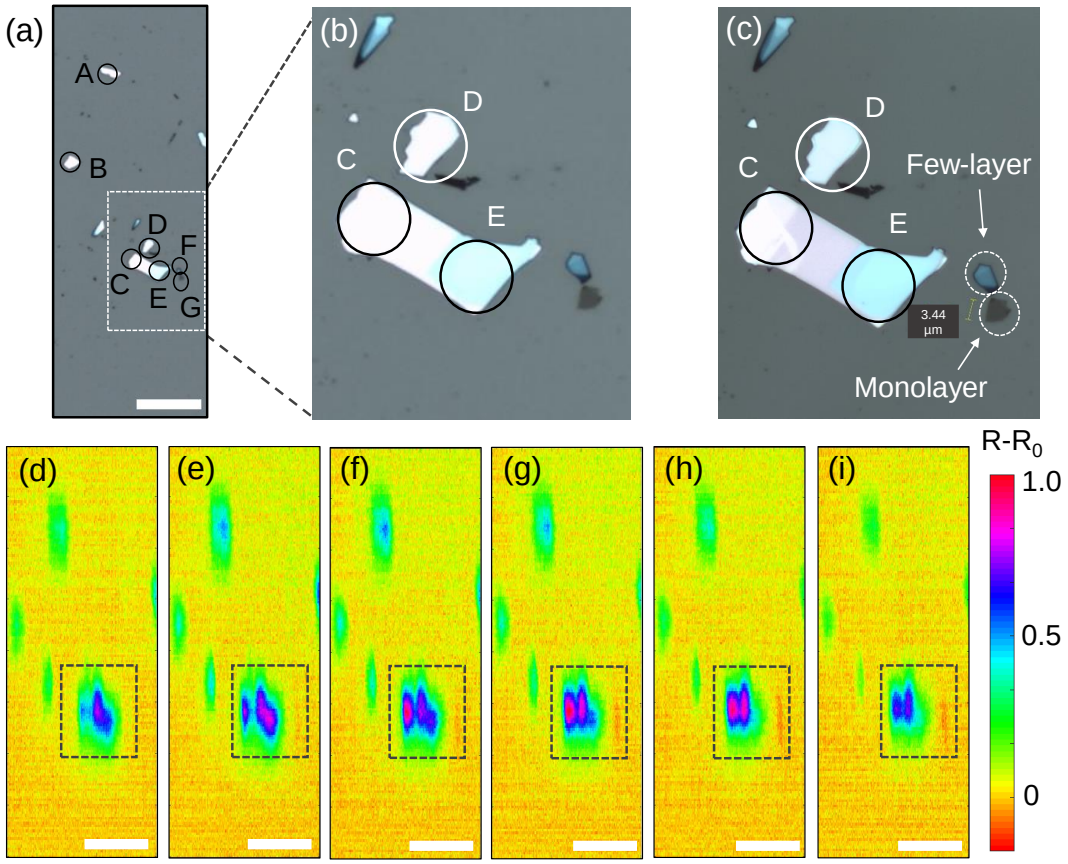

Figure 5.2: Optical images of the region of interest and single-band images reconstructed from the hyperspectral data set of the MoS_2 sample. (a) Optical microscope images of the region of interest (120×330 µm^2), and images with (b) 50× and (c) 100× magnifications. The region shown in (b) is the region labeled by white dots in (a), and the region shown in (c) is the region labeled by dots in (b). (d)-(i) The single-band images of the region shown in (a). Scale bar= 50 µm.

To investigate the spectral features of these flakes, single-pixel spectral analysis was conducted. Figures 5.3(a)-(b) show the corresponding spectra of the labeled pixels from Figures 5.2(a). A-C and D-E illustrates MoS_2 flakes with different thicknesses according to the spectral curves, which is consistent with the spatial variation of the hyperspectral single-band images (Figures 5.2(d)-(i)). The spectra of thin flakes labeled F and G were extracted and the intensities were lower than those of other flakes due to the small sizes (Figure 5.3(c)), where F flake (few-layer MoS_2) and G flake (monolayer MoS_2) showed distinct A and B exciton peaks due to strong absorption [238]. The differential reflectance

spectra of F flake (few-layer MoS_2) and G flake (monolayer MoS_2) showed distinct A and B exciton peaks due to strong absorption (Figure 5.4).

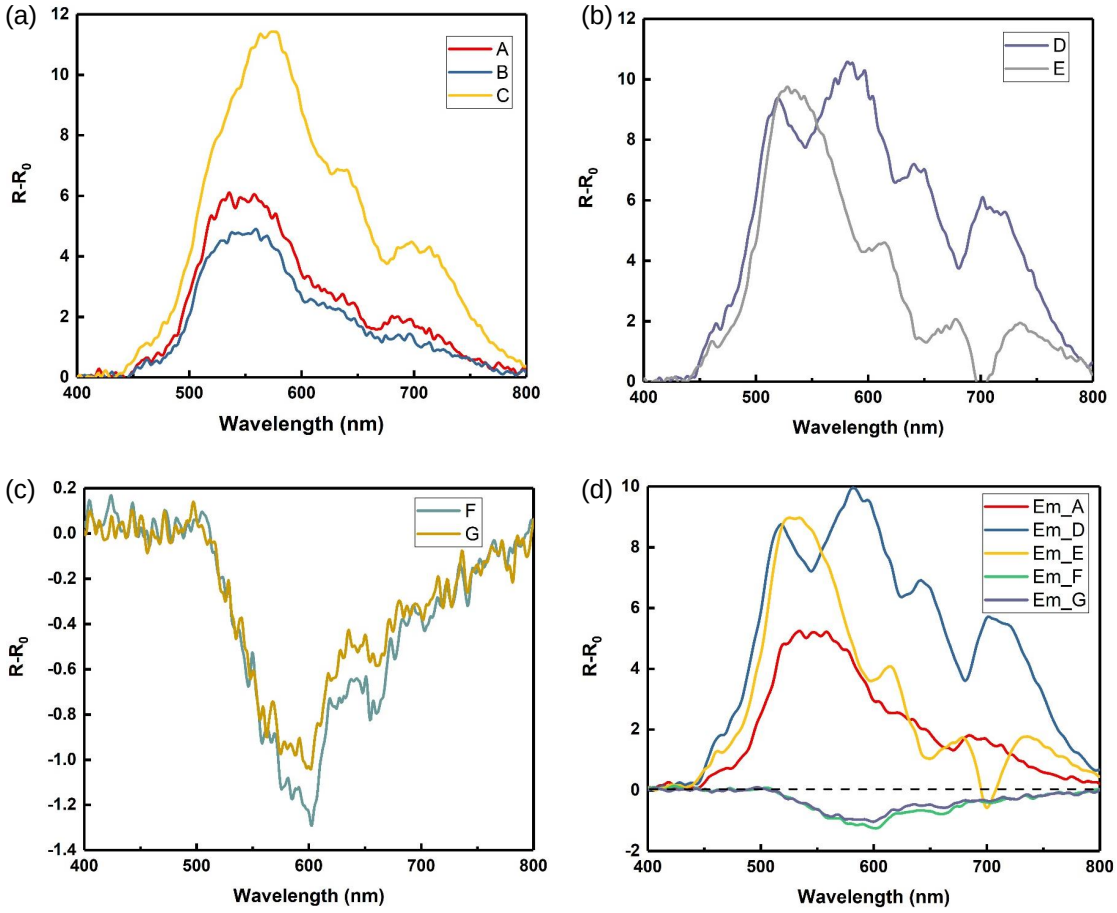

Figure 5.3: The extracted characteristic spectra of MoS_2 flakes with varying thicknesses. (a)-(c) The spectra of the corresponding labeled regions in Figure 5.2(a). To reduce the noise of the single-pixel spectra, the spectra in (a)-(c) are averaged from the lateral two pixels. (d) Five selected end members averaged from the spectra of corresponding flakes (A, D, E, F, and G in Figure 5.2).

To obtain the distribution of monolayer and few-layer flakes for stacking to form functional heterostructures, thickness mapping by linear unmixing was conducted based on the single-band analysis and pixel-level spectral analysis. The averaged spectra of these pixels were considered as the end members (Figure 5.3(d)). Using linear unmixing, the abundances of five end members were obtained and shown in Figure 5.5(b). Since the reflectance from F and G were lower than those of other areas, the abundance of F (few-layer) and G (monolayer) could not be easily distinguished in Figure 5.5(b). Another linear unmixing calculation using only end members of F and G was conducted, and the abundance map (Figure 5.5(c)) showed the distribution of F and G in false colors. Figure

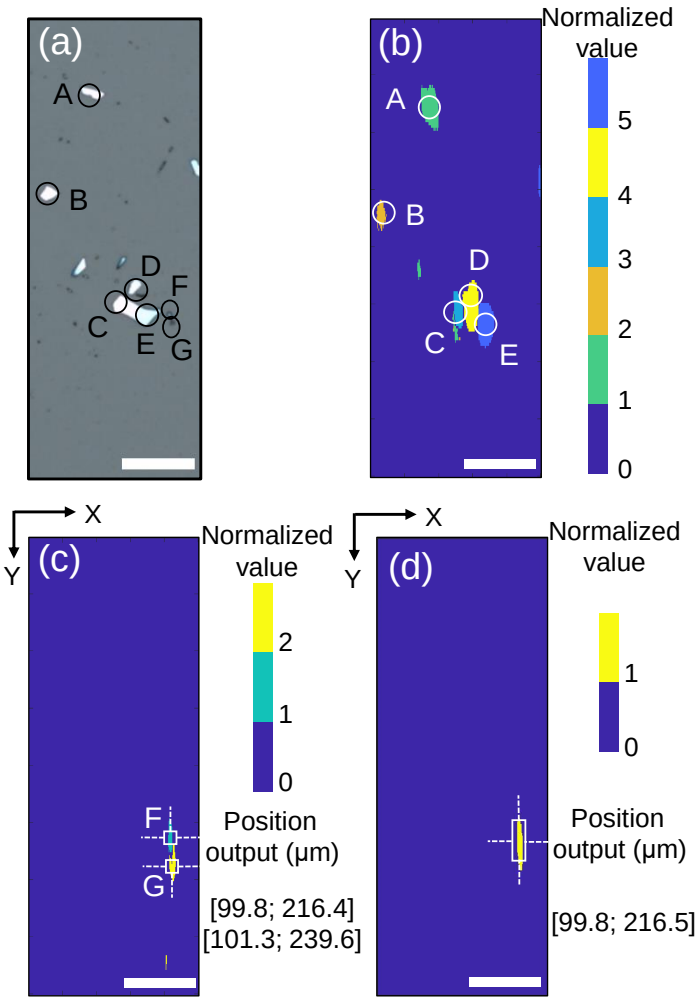

Figure 5.4: The differential reflectance spectra of monolayer and few-layer MoS_2 flakes calculated by $(R\text{-}R_0)/R$. A and B excitonic peaks are labeled with circles.

5.5(d) illustrates the abundance map of automated search of monolayer and few-layer MoS_2 flakes using the averaged spectra from F and G areas as the end member. This process is in practice very useful because both F and G flakes are interesting to researchers for further research. The identification of monolayer and few-layer MoS_2 flakes within the region of interest (120×330 μm^2) was realized using the hyperspectral imaging microscope system. Because the flakes F and G were small-sized (3 μm^2), the noise was induced to the extracted spectra, which leads to difficulty in directly distinguishing the spectra difference from monolayer and few-layer MoS_2 flakes. The spectra difference can be further combined with peak shifts for distinguishing monolayer and few-layer flakes. For 2D flakes for device applications, the size of monolayer and few-layer flakes should be larger than those of F and G flakes used in this chapter. Hence, the characteristic spectra of monolayer and few-layer MoS_2 can be extracted with a higher signal-to-noise ratio for

better classification performances.

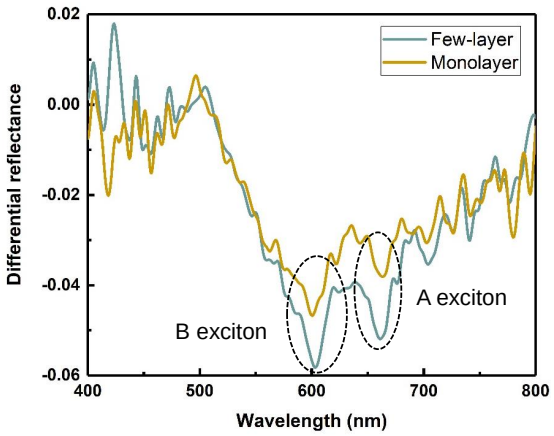

Figure 5.5: The pixelwise classification results after linear unmixing. (a) The optical image of the scanned region of interest with different flakes labeled A-G using the optical microscope. (b)-(c) The reconstructed abundance maps of the five end members extracted from different areas. (d) The abundance map of F and G areas as a whole. This image is useful in practice for showing the distribution of both monolayer and few-layer MoS_2 flakes. Scale bar= 50 µm.

5.2 Layer Mapping of Multi-layer hBN

5.2.1 Hyperspectral Measurement and Thickness Map Reconstruction

The fabrication method used for acquiring layered hBN flakes was the same as that for making MoS_2 flakes. Similarly, one region of interest was selected after observing the sample with a conventional microscope. Figure 5.6(a) shows the optical microscope images of the hBN flakes distributed on the SiO_2/Si substrate with 70 nm thick SiO_2. Different flakes including bulk and multi-layer hBN were labeled from A1 to F1. B1 and E1 flakes were multi-layer hBN with lower optical contrast. These flakes are, for example, more interesting for encapsulation of active 2D materials and heterostructures and potential devices. Single-band analysis of the hyperspectral data set can provide an overview of the distribution of different flakes according to the spatial distribution at changing wavelengths. Figures 5.6(b)-(f) show the background-subtracted images at five selected wavelengths of 572 nm, 601 nm, 645 nm, 660 nm, and 674 nm, separately. Different flakes show different intensities at specific wavelengths, which provides the local distribution information of these flakes. The distribution of the flakes labeled in Figure 5.6(a) from A1 to F1 can also be distinguished in Figures 5.6(b)-(f).

The pixel-level spectral analysis of hBN flakes was conducted based on the extracted spectra of different flakes. Figures 5.6(g) shows the extracted spectra of the five flakes by averaging the lateral two pixels to lower the noises, which the characteristic spectra from the corresponding regions in Figure 5.6 (a). B1 and E1 flakes were multi-layers based on the spectral features over the visible range. To show the extracted spectra and compare them to the spectral feature of hBN in a former report [38], R_0-R calculation was used for spectral analysis, which doesn't influence the abundance maps compared to those of R-R_0 calculation. To further analyze the spectra, the optical contrast by (R_0-R)/(R_0+R) calculation of these flakes were calculated (Figures 5.6(h)) [237]. Consistent with the former reports, there is a range of spectra lower than zero around 500 nm and the values are positive after this wavelength range [240]. To obtain the distribution of bulk and multi-layer hBN flakes based on the featured spectra, linear unmixing was employed to calculate the abundance of A1-E1 flakes. According to the spectra from Figures 5.6(g), A1, C1, and D1 possessed similar spectra and were classified as bulk hBN flakes based on the spectral characteristics. Figures 5.6(j) shows the abundance map of flakes A1-E1 in a single calculation using the extracted five end members. Figures 5.6(k) illustrates the abundance map of only E1 end member, indicating the distribution and position of the multi-layer hBN flake. The distribution of multi-layer hBN flakes was found by linear unmixing of the hyperspectral data set. The end members of A1, B1, and E1 are shown in Figure 5.6(i). To measure monolayer hBN flakes, the optical contrast should be maximized for the best imaging performance. It has been reported that the optical contrast varies with the change of the thickness of SiO_2 for graphene [241], MoS_2 [242], and hBN [243, 244]. Therefore, by building the relation between the optical contrast of monolayer 2D materials and the oxidation thickness of the substrate, monolayer 2D flakes can be distinguished in an optimized way, especially for hBN with low contrast, which should be conducted in the following work.

5.2.2 Hyperspectral Characterization of An Unknown Region

To test the capability of the proposed line-scan hyperspectral imaging microscope with the linear unmixing method, another hBN sample with 270×640 μm^2 region was studied. Because the horizontal size of the region of interest is larger than the length of the field of view of the setup, this area was scanned three times by moving the sample in x-direction manually after a single continuous scan. Three hyperspectral data sets were acquired and combined by eliminating the overlapped regions. The background-subtracted hyperspectral images were reconstructed at seven wavelengths (492 nm, 514 nm, 528 nm, 543 nm, 579 nm, 601 nm, and 630 nm, separately), shown in Figures 5.7(a)-(g). By comparing the changes of spatial images, one flake (white circled area in Figure 5.7(c)) was selected due

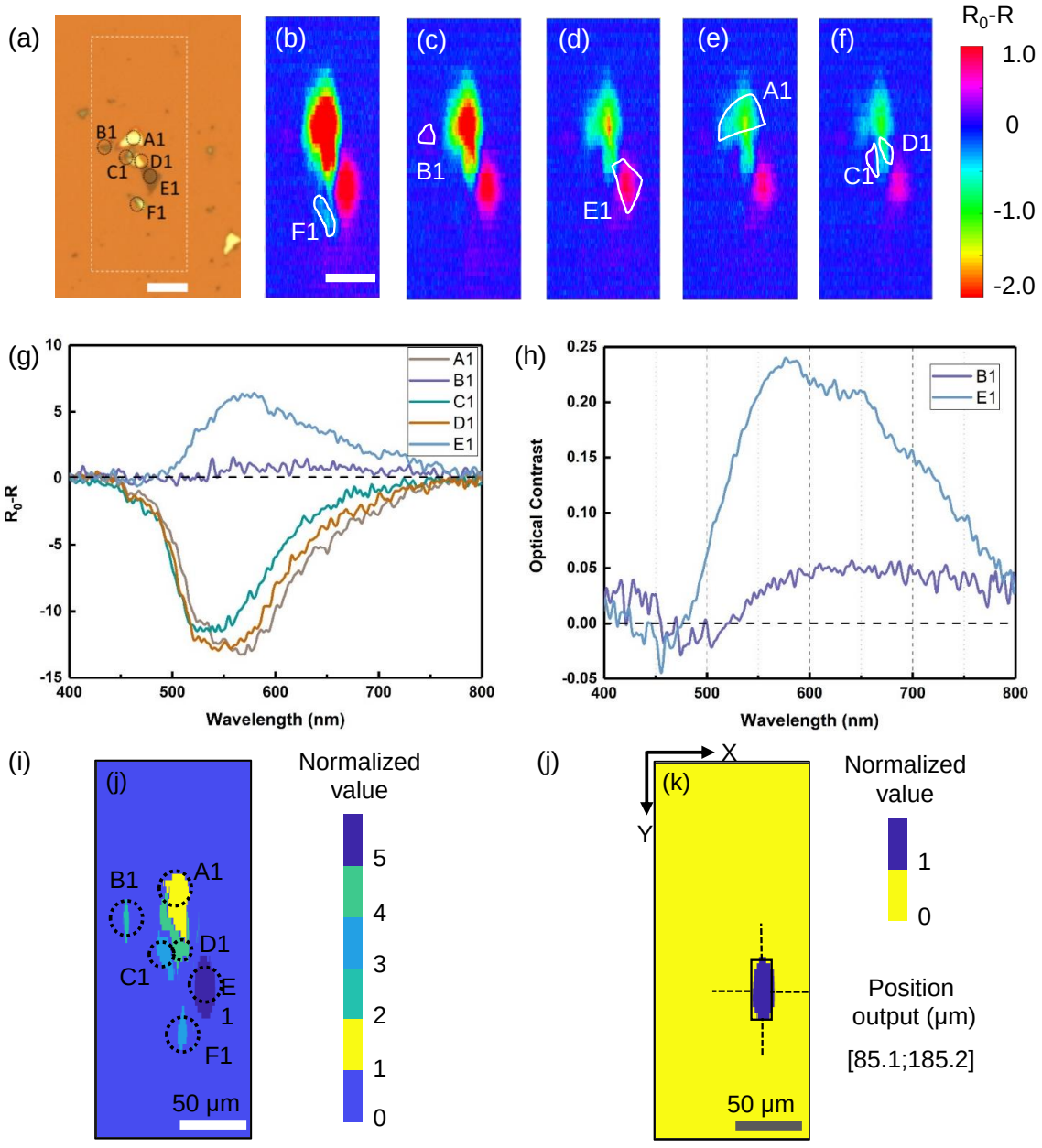

Figure 5.6: A step-by-step analysis including single-band analysis, pixel-level spectral analysis, and image classification for the automated search of the multi-layer hBN flake. (a) Optical microscope image of the region of interest. (b)-(f) Single-band images reconstructed from the hyperspectral data set of the hBN flakes. (g) The pixel-level spectral analysis of bulk and multi-layer hBN flakes. (h) The optical contrast of the multi-layer hBN flakes labeled with B1 and E1. (i) End members of corresponding A1, B1, and E1 flakes. (j) Abundance map of all flakes in a single calculation. (k) Abundance map of the end member E1. Scale bar= 50 µm.

to its negative reflectance, which is similar to that of E1 flake in Figure 5.6(d). The E1 end member was used to calculate the abundance map of the newly-acquired hyperspectral data set (Figure 5.7(h)). The abundance map (Figure 5.7(h)) and the microscope image (Figure 5.7(i)) display high consistency with each other, demonstrating the ability of this method for wafer-scale measurement.

The measured reflection spectra can be influenced by the NA of the microscope objective lenses, such as the peak position and the spectra magnitude [242, 245]. Here, the hyperspectral data sets of MoS_2 and hBN samples were measured using the same 60× magnification objective lens (NA 0.85). However, when the objective lens with a higher NA is used, the measured reflection spectra of the same region might differ from each other. Hence, the end members (averaged spectra from the flake regions) used for abundance calculation need to be consistent with the NA of objective lenses. If the previously-extracted end members are used for linear unmixing to calculate the abundance maps of another sample when the objective lens is changed, the abundance maps of different flakes can be influenced. For the measurement of other 2D materials using different objective lenses, optical modeling of the system such as NA correction by simulation and experimental results is required [50, 246].

There are two possible improvements to this method to realize better performances. Firstly, the single-band images extracted from the hyperspectral data sets are kind of stretched in the vertical direction. One reason is the relatively low vertical resolution. For the line-scan hyperspectral imaging microscope, the vertical resolution is less than the horizontal resolution, which is caused by the nature of the line-scan working mode and the way of light dispersion. Another explanation is the influence of the light out of the confocal line including the fluorescence, the scattered spectrum, and the diffraction of light originating from a convolution of the illumination spot with the slit aperture. In the present work, the stretched shape in the vertical direction was eliminated when choosing the representative spectra with higher criteria and the blurred areas were removed. The reconstructed abundance images show higher performances than the single-band hyperspectral images. To increase the imaging performance of the line-scan system may require to change the global illumination to line-shape illumination (laser illumination for hyperspectral photoluminescence imaging) [247], add an adjustable slit before the collimating lens to reduce the non-confocal-line light, and conduct the deconvolution of the hyperspectral images in the spectral domain [248, 249].

The second improvement is that the intelligent end member extraction needs to be achieved which can lower the errors of manual area selection for pure spectra acquisition. The ability of this technique of distinguishing the differences even between monolayer and bilayer flakes needs to be further tested. Figure 5.5(c) shows that monolayer and few-layer

MoS_2 flakes can be classified. Few-layer flakes (layer number less than 10) can in theory be differentiated based on their spectral profiles and can be imaged with methods like pixel-level denoising and machine learning. Based on the former research by spectroscopy techniques, there is a relation between the exciton peaks of optical contrast and layer number of flakes [250, 251], which can be employed as reference information for thickness identification. Like the former reports using spectroscopy technique to build the relation of peak shifts and layer thickness [252], hyperspectral imaging techniques can use this knowledge and realize better mapping performances of thickness distribution. A library of spectra ranging from monolayer to multi-layer flakes of different types of 2D materials is necessary for future applications.

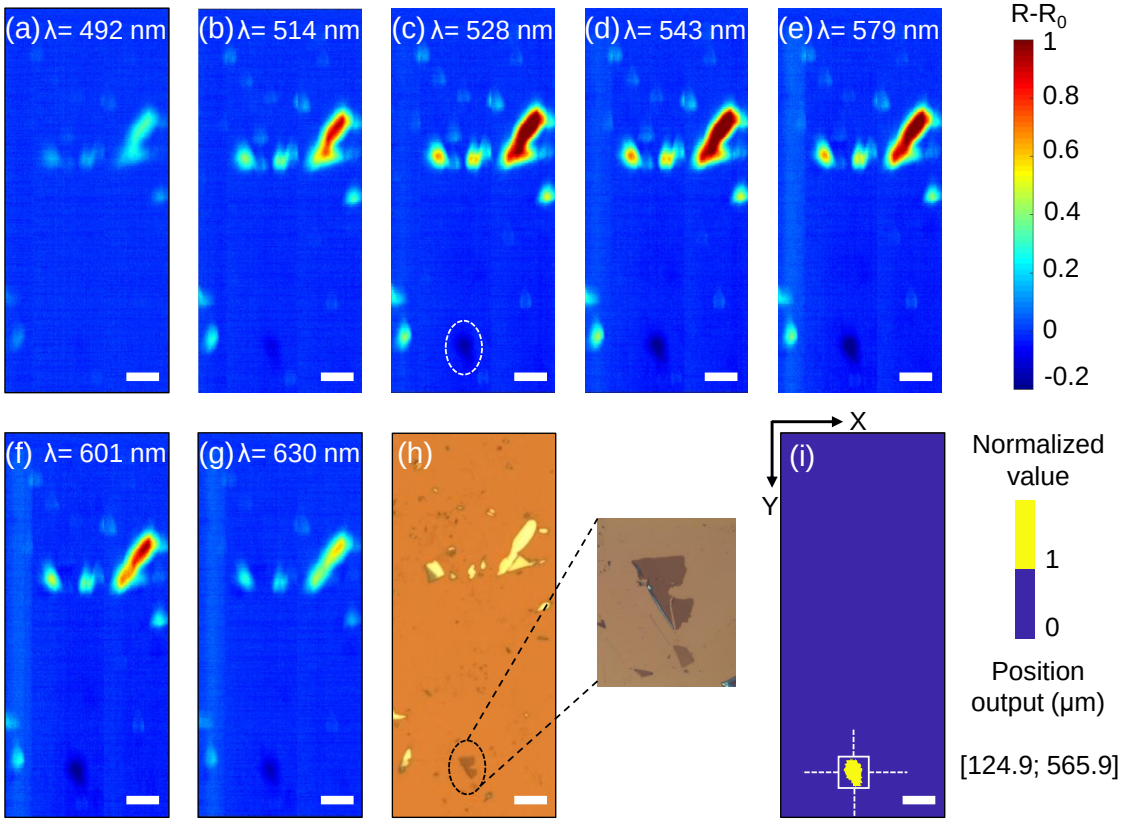

Figure 5.7: The single-band images, abundance maps, and the microscope images of a large unknown region of interest (270×640 µm^2). (a)-(g) The reconstructed hyperspectral images at different wavelengths. (h) The optical microscope image of an unknown region of interest and the magnified image of the multi-layer flake. (i) The reconstructed abundance map. Scale bar= 50 µm.

5.3 Identification Accuracy Evaluation using CVD MoS_2

In this part, to further evaluate the identification accuracy using hyperspectral imaging microscopy and spectral unmixing for rapid layer number mapping of 2D materials, characteristic hyperspectral fingerprints of CVD-grown MoS_2 flakes were extracted and implemented for atomic layer number reconstruction. First, the broadband hyperspectral fingerprints of mono- and bi-layer MoS_2 flakes with high spectral similarity were extracted for distribution map reconstruction using the constrained least-squares optimization, with cross-validation applied to new regions. Second, the method was generalized by mapping the distribution of mono-, tri-, and few-layer MoS_2 flakes. Third, to reduce the computational consumption, influence of dimension reduction of hyperspectral data sets on identification performances was investigated using mono- and bi-layer hyperspectral fingerprints with high spectral similarity.Finally, a multiline laser was used as the illumination source to measure exfoliated WSe_2 flakes which were not easily detected by the broadband illumination due to their small sizes.

5.3.1 Hyperspectral Fingerprints and Map Reconstruction of Mono- and Bi-layer Flakes

The characteristic spectra of CVD-grown MoS_2 flakes are dependent on the atomic layer number, oxidation thickness of the SiO_2/Si substrate, illumination conditions, and the numerical aperture of the microscope objective. MoS_2 flakes were grown on the SiO_2/Si substrate with an oxidation layer thickness of 270 nm. The layer number of flakes were manually identified based on the reflection optical contrast of 2D materials. The microscope objective and illumination conditions were kept unchanged during all measurements. Therefore, the measured spectra of MoS_2 flakes were directly dependent on the layer numbers. Figure 5.8 illustrates the process for extracting hyperspectral fingerprints and reconstructing distribution maps of the MoS_2 sample. A region of interest containing mono- and bi-layer MoS_2 flakes identified manually by optical contrast was selected for demonstration (Figure 5.8(a)). After a continuous scan by the hyperspectral microscope, the images of the region of interest at different wavelengths could be reconstructed. Figure 5.8b illustrates nine images at the spectral range of 543-609 nm from a total of 1004 channels covering a wavelength range of 325-1056 nm, showing the spatial variations of flake areas along with the wavelength change. The spectral range of 400-700 nm was used for fingerprints extraction and calculation. In the hyperspectral data set of the measured region of interest, each pixel had a specific spectra. Since the system captured the spectral information of 1004 px at a single capture, slight noise became a large portion of the

pixel-wise spectra. To avoid misclassification of pixels from lateral layer numbers, original hyperspectral data sets were processed by background subtraction which eliminated the influence of uneven illumination distribution, and hyperspectral denoising algorithms to remove spatial and spectral noises using the total variation minimization (Figure 5.8(c)). The intensity normalization reduced the inhomogeneous illumination by subtracting the signal from the substrates at each spectral channel. The denoising algorithm adapted from stimulated Raman spectroscopic images analysis provided representative spectra with high SNR. The optical image (Figure 5.8(a)) as a reference showed the position of each type of flakes, where the characteristic spectra were extracted by averaging the spectra of pixels (50-100 px) from the same flake in the hyperspectral data set. Figure 5.8(d) shows the characteristic spectra of mono- and bi-layer flakes used as the hyperspectral fingerprints. The extracted hyperspectral fingerprints were combined with spectral unmixing analysis to reconstruct the spatial distributions of monolayer (1L) and bilayer (2L) flakes (Figure 5.8(e)). The isolated monolayer MoS_2 island (bottom flake) and the monolayer MoS_2 flake surrounding bilayer flakes (top and middle flakes) were identified and mapped. The hyperspectral fingerprints of mono- and bi-layer flakes have high similarity to each other. Such hyperspectral similarity was a challenge for the algorithms to classify pixels with similar spectra. Monolayer and bilayer pixels with similar spectra were successfully classified with single-layer accuracy of the hyperspectral microscopy system for 2D materials identification (Figure 5.8(d)).

To analyze classification performances of pixels with various spectra using the fingerprints and spectral unmixing method, five pixels predicted as mono- and bi-layers (A-B as monolayer, C-E as bilayer) were selected (Figure 5.9(a)) and their averaged spectra and standard deviation from the denoised hyperspectral data set (Figure 5.8(c)) were shown in Figure 5.9(b). The spectra of A-B pixels with peak intensity around 0.3 have smaller differences with the monolayer fingerprint, while the spectra of C-E pixels with peak intensity around 0.4 are classified as bilayer. Figure 5.9(c) illustrates a single-channel image at 543 nm from the hyperspectral data set. The mean value and standard deviation of the reflection intensity distribution along the L2 direction (Figure 5.9(c)) was shown in Figure 5.9(d) based on the data at wavelengths of 543 nm, 558 nm, 572 nm, 587 nm, and 601 nm for demonstration. The grey curve in Figure 5.9(d) shows the predicted layer number distribution along the L1 direction in Figure 5.9(a) for comparison. According to the averaged spectra of mono- and bi-layer (Figure 5.9(b)), pixels in Figure 5.9(d) with intensity values smaller than 0.3 can be classified as monolayer, while pixels with intensity values between 0.3 and 0.4 can be classified as bilayer, which is consistent with the spectra features and the classification results.

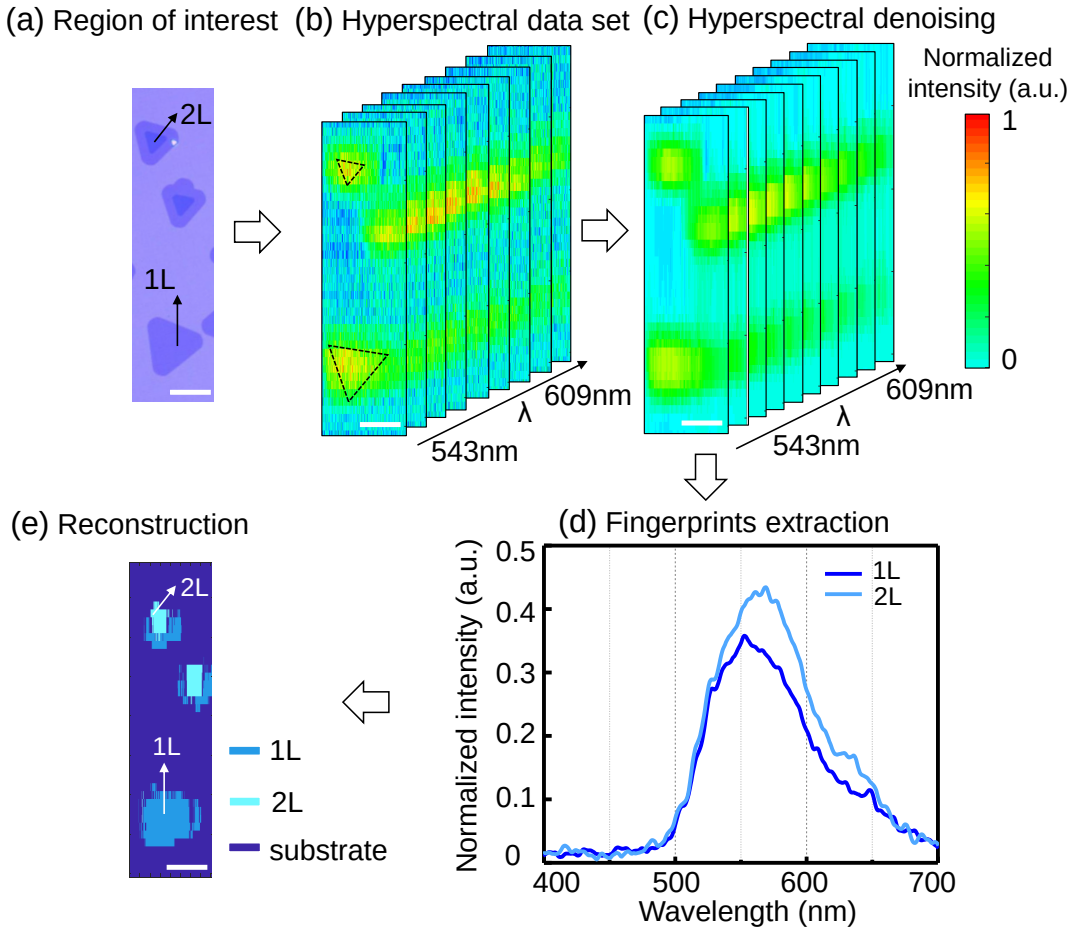

Figure 5.8: Process of hyperspectral fingerprints extraction and distribution maps reconstruction of CVD-grown MoS_2. (a) The optical microscopy image of the reference region with the distribution of mono- and bi-layer MoS_2 flakes. Single-channel images from the acquired hyperspectral data set at the spectral range of 543-609 nm (b) after the background subtraction and (c) denoising for demonstration. (d) The extracted hyperspectral fingerprints of mono- and bi-layer categories by averaging the spectra of neighboring pixels within the same category region. (e) The reconstructed abundance map of MoS_2 flakes after spectral unmixing. Scale bars = 20 µm.

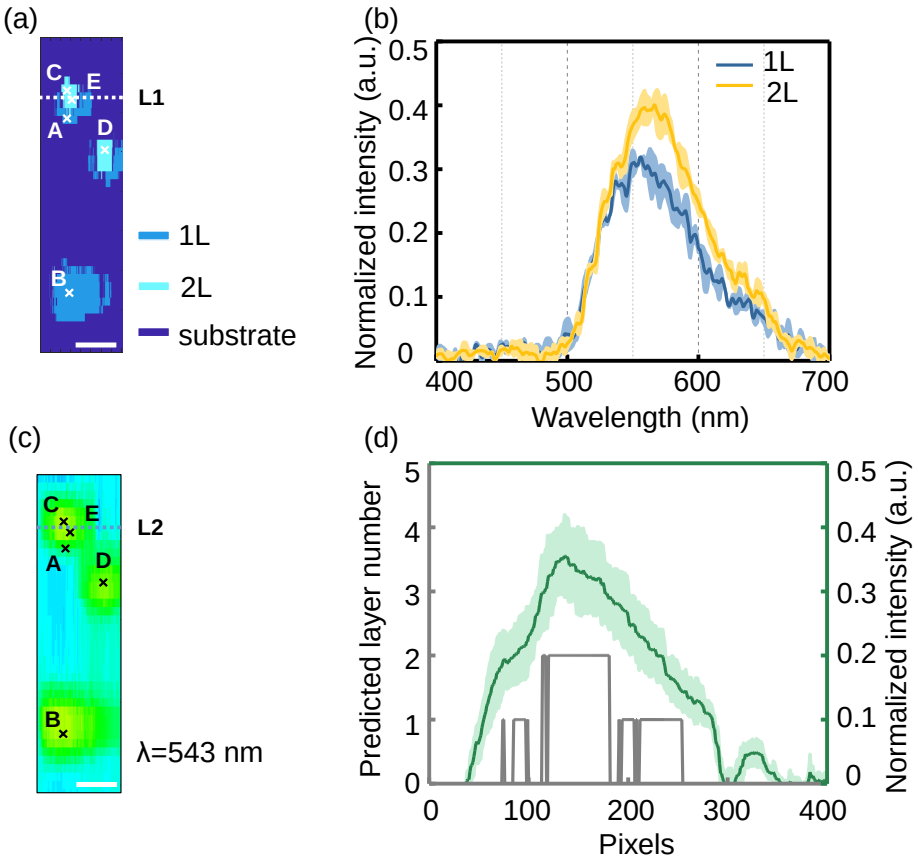

Figure 5.9: Pixel-wise spectral analysis using the denoised hyperspectral data sets. (a) Selected pixels from mono- and bi-layer regions in the reconstructed distribution map. (b) Averaged spectra with standard deviation of selected mono- and bi-layer pixels from the denoised hyperspectral data set. (c) Single-channel image from the denoised hyperspectral data set at the wavelength of 543 nm. (d) The spatial distribution of averaged reflection intensity and standard deviation along the L2 direction in (c). The averaged value and standard deviation were calculated based on the data at five representative wavelengths of 543 nm, 558 nm, 572 nm, 587 nm, and 601 nm. The grey curve shows the predicted layer number distribution along the L1 direction in (a). Scale bars = 20 µm.

5.3.2 Cross-validation and Generalizability Analysis

To validate the practicality of the previously extracted hyperspectral fingerprints in newly-measured samples, cross-validation was conducted using new MoS_2 samples where mono- and bi-layer flake categories existed. This study investigated if one pixel with monolayer thickness could be incorrectly classified into the bilayer subclass due to high spectral similarity. No further data processing was conducted on the new hyperspectral data set after background subtraction and denoising. Figure 5.10 illustrates the cross-validation results when applying previously extracted hyperspectral fingerprints to the data set of MoS_2 flakes in a new region. According to the optical microscope image and labels identified by optical contrast in Figure 5.10(a), mono- and bi-layer flakes appeared in this region. After the background subtraction and denoising of the hyperspectral data set, the calculated abundance map showed that, pixels of this region could be correctly classified as mono- and bi-layer categories, despite of the high similarity between the hyperspectral fingerprints (Figure 5.10(b)-(d)). This cross-validation using the hyperspectral fingerprints extracted from a reference region demonstrated the versatility of hyperspectral features after a one-time effort.

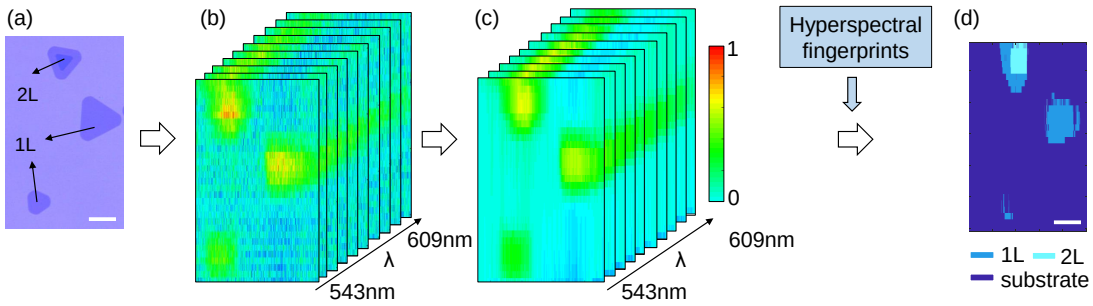

Figure 5.10: Cross-validation using the previously extracted hyperspectral fingerprints for layer number maps reconstruction of a new region. (a) The optical microscopy image of the new region with the distribution of mono- and bi-layer MoS_2 flakes. Single-channel images from the acquired hyperspectral data set at the spectral range of 543-609 nm after the background subtraction (b) and denoising (c) for demonstration. (d) The abundance map of MoS_2 flakes after spectral unmixing. Scale bars = 20 µm.

Further, generalizability of hyperspectral fingerprints and spectral unmixing method for layer number identification was analyzed using a second region with more flake categories (mono-, tri-, and few-layer). The whole process for the generalizability analysis included the selection of the region of interest, hyperspectral data set acquisition, and abundance map reconstruction of all the compositions using the extracted hyperspectral fingerprints (Figure 5.11(a)-(d)). The distribution maps of each composition were also obtained (Figure 5.11(e)-(g)), showing that pixels of this region could be correctly classified as mono-,

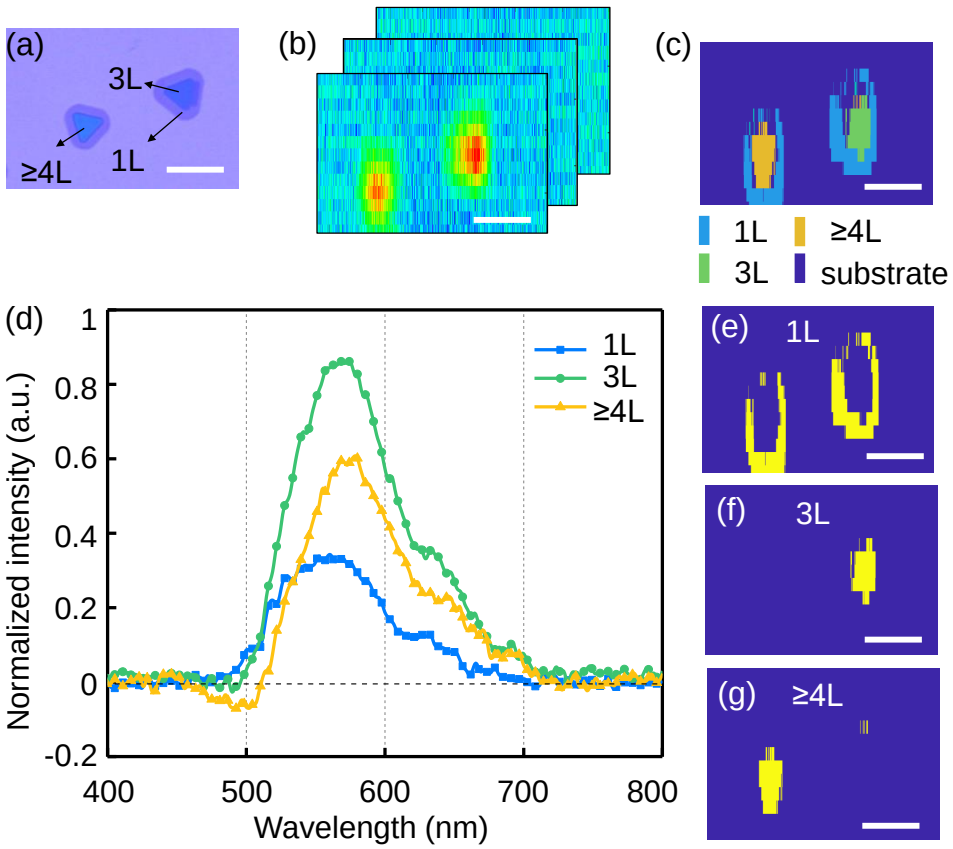

Figure 5.11: Generalizability analysis of hyperspectral fingerprints and the spectral unmixing method using a region with three MoS_2 flake categories. (a) The optical microscope image of the new region with the distribution of mono-, tri-, and few-layer MoS_2 flakes. (b) Single-channel images at the wavelengths of 572 nm, 594 nm, 616 nm. (b) Pixel-wise classification of mono-, tri-, and few-layer flake categories by one spectral unmixing calculation. (d) Extracted hyperspectral fingerprints of mono-, tri-, and few-layer flake categories. (e-g) Abundance maps of mono-, tri-, and few-layer flake categories, respectively. Scale bars = 20 µm.

tri-, and few-layer categories. The profile outputs were not as accurate as those from the microscopic image due to the spatial resolution loss of the hyperspectral microscope. However, most of the pixels from each category were correctly classified, which was sufficient to enable the search and localization of flakes with specific layer numbers.

5.3.3 Analysis of Hyperspectral Dimension Reduction

Although hyperspectral data sets provide abundant information for accurate pixel-wise classification in the scanned region, the high dimensional data set can be computationally expensive. To enable the application of the developed method, layer mapping performances were studied with the dimension reduction of the hyperspectral data set. Figure 5.12(a) illustrates the process of channel selection and dimension reduction of the original hyperspectral data set. First, the hyperspectral data set was extracted at the visible range of 400-700 nm from the original hyperspectral data set of 325-1056 nm. The extracted hyperspectral data had 400 channels. Second, the dimension of the 400-channel hyperspectral data set was downsampled to a 200-channel hyperspectral data set. The same process was repeated to obtain hyperspectral data sets with lower dimensions. The same hyperspectral data set used for cross-validation of hyperspectral fingerprints (Figure 5.10), was utilized. To quantify the distinction between two hyperspectral fingerprints, spectral similarity index (SI) was defined as

$$SI(\%) = \sqrt{\frac{\sum \left\{ \frac{i_1(\lambda) - i_0(\lambda)}{i_0(\lambda)} \times 100 \right\}^2}{N}} \tag{5.1}$$

where i_1 and i_0 are the normalized intensity at different spectral channels, and N (1, 2,. . . , λ) is the number of the spectral channels. SI is used to quantify the spectral differences between two distinct spectra. The more similar two spectra are, the smaller value the calculated SI is. The SI value of zero means the two spectra are the same ones.

Figure 5.12(b)-(m) shows the hyperspectral fingerprints and reconstructed abundance maps of mono- and bi-layer MoS_2 flakes at different dimensions (400, 200, 100, 50, 10, and 5 channels). The spectral similarity index of the hyperspectral fingerprints was calculated. Due to the denoising of the hyperspectral data sets, the extracted hyperspectral fingerprints had distinct features compared to the spectral noises. In the dimension reduction from 400 to 5 channels, the pixels were correctly classified into mono- and bi-layer categories. The spectral similarity index of the hyperspectral fingerprints maintained at a stable value, which provided distinct feature information and enabled the classification of pixels with different spectral information to the correct categories. The above results can

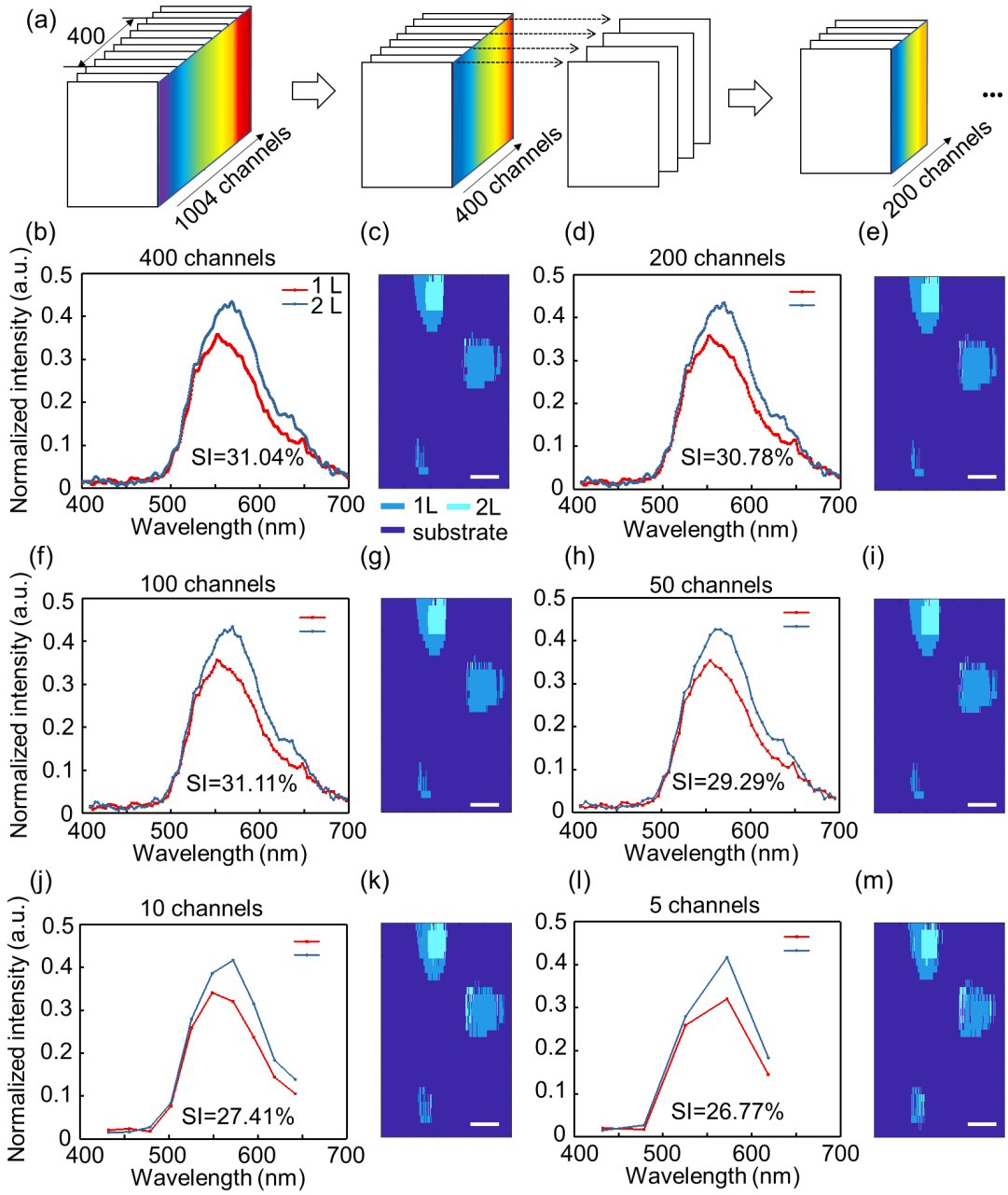

Figure 5.12: Process of building a hyperspectra library. (a) The optical microscope image of the region of interest with distribution of MoS_2 flakes from monolayer to bulk. (b)-(d) Single-channel images from the acquired hyperspectral data set. (e) The abundance map of MoS_2 flakes from monolayer, bilayer, trilayer, multi-layer, and bulk after the pixelwise classification. (f) The extracted characteristic spectra representing different flakes as part of the spectra library. Scale bar= 20 µm.

be resulted by two factors. The first one is the maintained values of spectral similarity index. The second factor is the number of categories. In this work, two categories were chosen for demonstration. When more categories were selected for identification, more channels need to be kept to ensure the correct estimated abundance maps.

5.4 Dual-illumination Hyperspectral Microscopy and Performance Evaluation

Figure 5.13 illustrates the schematic and photograph of the dual-illumination hyperspectral microscopy system, working at the epi-illumination mode. The dual-illumination includes a broadband LED (yellow beam path) and a multiline laser (blue beam path), working for specific cases of 2D materials measurements. Both illumination modes shared the same light path after the microscope objective (Leica, NA 0.85, N plan, EPI). The switch of the illumination modes was achieved by using a rotatable beam splitter (BS1) for precise rotation angle control. Broadband light (470-850 nm) from the LED was propagated to illuminate 2D samples on SiO_2/Si substrates through the objective. The reflected light from the sample was collected by the objective, split for observation (BS2), and focused by a cylindrical lens (L) onto the slit of a hyperspectral imager. The hyperspectral imager, which consisted of a Czerny-Turner spectrograph (the combination of M3, M4, M5, and RG) and a CCD camera, dispersed the incident light and recorded the pixel-wise spectra of the line-shaped area. The illumination mode using a multiline laser (peak wavelengths at 457.9 nm, 476 nm, 488 nm, 496.5 nm, and 514 nm) was implemented to measure small flakes (size dimension of 1-3 µm) fabricated by mechanical exfoliation (blue light path in Figure 5.13(a)). Due to the enhanced focusing property of a laser light source, sharper spatial profiles of samples can be acquired. The light emitted from the laser was reflected (M1/2), expanded (BE), and collimated (CL2). An adjustable slit (AS) functioned as an aperture to obtain a line-shaped beam by spatial filtering. The laser beam was directed to illuminate the sample by rotating the beam splitter (BS1) to a previously calibrated angle, and the reflected light from the sample propagated along the same light path as the broadband illumination. The slit of the hyperspectral imager was fixed with a width of 16 µm for both illumination modes.

Mechanically exfoliated WSe_2 flakes on a SiO_2/Si substrate with an oxidation thickness of 70 nm were used for demonstration. Figure 5.14(a) illustrates a sample-free capture of the camera with one spatial and one spectral coordinates. Figure 5.14(b) shows the spectra of the multiline laser extracted along the A-direction in Figure 5.14(a). Figure 5.14(c) shows the spatial distribution of the multiline laser extracted along the B-direction in Figure 5.14(a). A region of interest with WSe_2 flakes of bilayer (2L) and few-layer (3-5L)

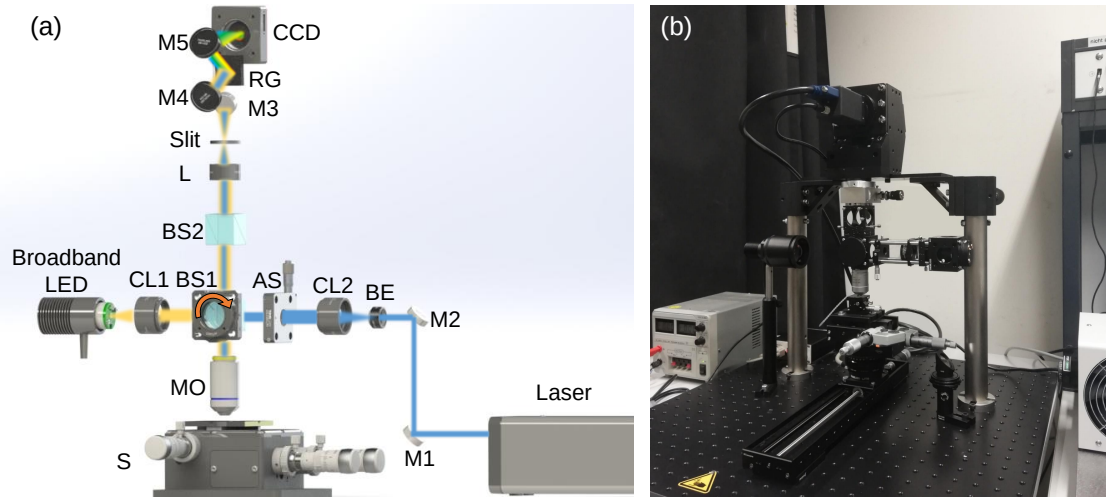

Figure 5.13: Schematic and photograph of the dual-illumination hyperspectral imaging microscope. (a) Schematic of the hyperspectral imaging microscope system. CL1-2, collimating lens; BS1-2, beam splitter; MO, microscope objective; AS, adjustable slit; M1-5, mirrors; BE, beam expander; L, cylindrical lens; RG, reflection grating; and S, stage. (b) Photograph of the dual-illumination hyperspectral imaging microscope.

was selected (Figure 5.14(d)) and scanned by the hyperspectral microscope (hyperspectral data set in Figure 5.14(e)). According to previous reports, the spectral difference of flakes with varying layer numbers can be observed in the whole visible range. The intensity variation at the multiline laser peaks were caused by the absorption of flakes at specific wavelengths. This could be considered as hyperspectral channel reduction (from supercontinuum illumination to multiline illumination). Therefore, the spectra change of the multiline laser source could be used for distinguishing flakes with varying layer numbers (Figure 5.14(f)). The distribution of two compositions (bilayer and few-layer flakes) was reconstructed using the same hyperspectral denoising and spectral unmixing method (Figure 5.14(g)). The spatial resolution using the multiline laser illumination mode is higher than that of broadband illumination mode, and the 2D flakes with sizes of a few microns can be detected.

The cross-validation and generalizability analysis of the hyperspectral fingerprints using the reference sample and the newly-measured samples showed that, the subtle spectra differences between different layer categories could be identified, and each type of flake could be searched and localized after spectral unmixing. Additionally, due to the spectral imaging nature (lower spatial resolution compared to that of RGB microscopes), the flake shapes in the reconstructed images were not as accurate as those in bright-field microscope images. The reconstructed layer maps based on the wideband illumination mode are more suitable for initial screening where accurate deformation information cannot be provided

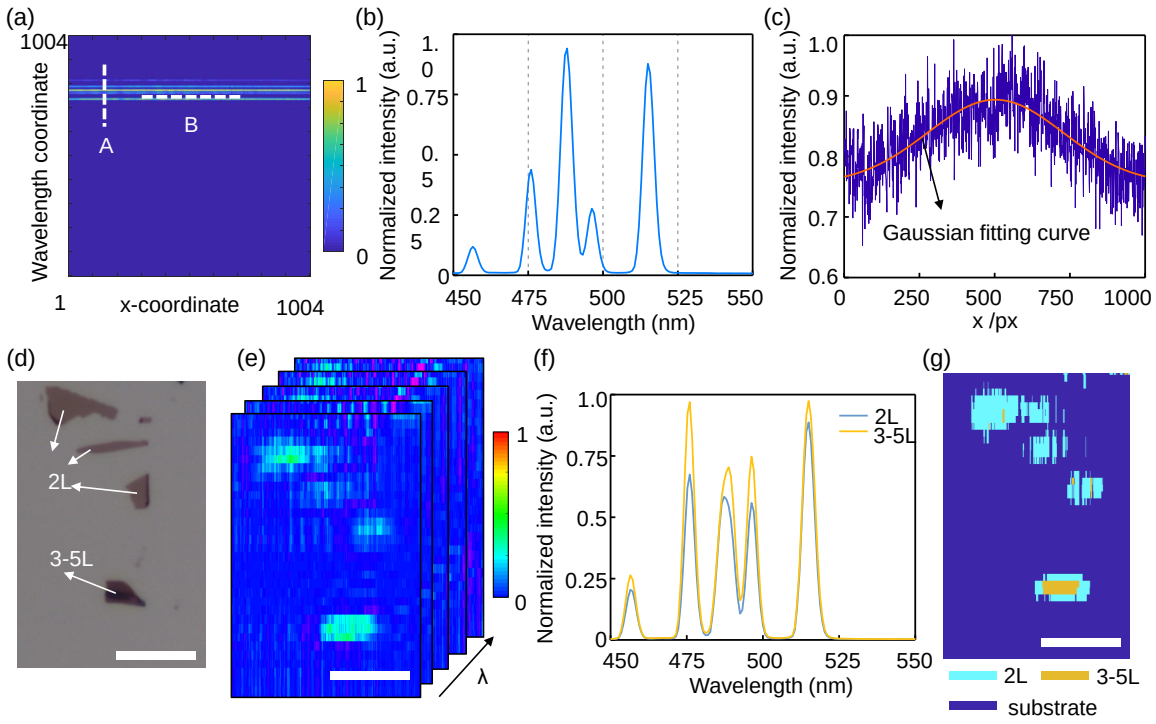

Figure 5.14: Data acquisition and pixel-wise layer map reconstruction using the multiline laser illumination. (a) Single sample-free capture of the camera during measurement showing the spectral distribution along the imaged line area. (b) The multiline laser spectrum with peak wavelengths at 457.9 nm, 476 nm, 488 nm, 496.5 nm, and 514 nm, respectively. (c) The spatial distribution of the laser illumination along the imaged line direction. The filtered curve shows the Gaussian distribution of the illumination beam. (d) The microscopic image of WSe_2 flakes on the SiO_2/Si substrate. (e) The hyperspectral data set of the same region is shown in (d). (f) The extracted hyperspectral fingerprints of bi- and few-layer flakes. (g) The reconstructed distribution map of two types of flakes. Scale bars= 20 µm.

(horizontal resolution is diffraction limited while the vertical scanning step size is 5 µm). The second mode of multiline laser illumination provides more accurate deformation information of CVD fabricated 2D materials. The horizontal resolution is diffraction limited while the vertical scanning step size is 1 µm. Further, this pixel-wise classification method was based on the intensity distribution of the whole spectra range; and therefore, slight intensity change might misclassify pixels to a wrong sub-class. Therefore, it is important to keep a fixed illumination condition by controlling an accurate stage position because slight stage position change can lead to variations of spectral intensity. Secondly, large flakes should be chosen for hyperspectral fingerprints extraction because this may render the spectra more representative. Thirdly, machine learning techniques such as generative adversarial network provides a way to compensate for the spectral variations of slight changes of illumination conditions and realize autofocusing of hyperspectral microscopy images. The spectral range of 400-700 nm was used for fingerprints extraction and calculation in this work. It is also possible to choose another spectral range where there is stronger absorption of 2D materials and the accuracy may be improved.

The hyperspectral-fingerprints-based mapping method can be utilized for studying heterogeneous properties of 2D materials. Theoretically, when the properties of 2D materials and their heterostructures correspond to their spectral behaviors, the heterogeneous variations in the spatial domain can be resolved using hyperspectral fingerprint extraction and distribution map reconstruction. For example, in the strain engineering of 2D materials, the strain-tuned heterogeneous optical properties of 2D materials can be spatially determined. Spectral fingerprints extraction and specific component mapping can also be utilized in Raman and photoluminescence spectroscopy for measurement and property investigation of 2D materials.

5.5 Summary

Line-scan hyperspectral imaging microscopy with linear unmixing was developed to characterize MoS_2, hBN, and WSe_2 samples fabricated by both the mechanical exfoliation and CVD methods by processing the multidimensional data sets. Pixelwise spectral analysis was used to extract the pure spectra of the monolayer and few-layer flakes. These pure spectra were employed as end members to reconstruct abundance maps which showed the distribution and accurate positions of different flakes. Furthermore, to test the identification accuracy of the system, a practical method achieved single-atomic-layer accuracy for layer number mapping of CVD-grown MoS_2 flakes, followed by cross-validation and generalizability analysis using new samples. The multiline laser illumination was implemented to enable the detection of small-scale flakes, realizing successful identification of mechani-

cally exfoliated WSe_2 flakes following the hyperspectral data set processing method. The investigation of hyperspectral dimension reduction and the abundance map reconstruction showed that when the spectral similarity index was maintained, the reduction of hyperspectral dimension did not significantly influence the identification performances.

Chapter 6

Deep-learning-enabled Images Fusion for Atomic Layer Mapping

In the developed manual interpretation method, the hyperspectral resolution and microscale spatial resolution have promoted an accurate layer number identification and flake position, which meets the requirement of researchers to search and locate the 2D flakes with specific layer numbers. However, in practice, the spatial resolution of hyperspectral imaging microscopy is lower than that of conventional optical microscopy, thus resulting in less accurate profile outputs. To this end, the fusion of both RGB images which provides accurate profile information, and hyperspectral images that provide abundant spectral information for layer number identification was conducted. In this Chapter, a dual-stream U-Net neural network is proposed to fuse RGB images (high spatial resolution) and hyperspectral images (high spectral resolution) for identification and segmentation of atomic layer flakes with monolayer, bilayer, trilayer, and multilayer thickness grown by CVD.

6.1 Principle of the Deep Fusion Method

A machine-learning-based image fusion technique, which integrates the complementary information from different optical modalities and generates a single prediction [253, 254], has been proposed for various applications such as remote sensing and medical imaging [255–258]. Figure 6.1 illustrates the process of atomic layer mapping of 2D flakes using the dual-stream deep fusion method. In the sample fabrication process, the MoS_2 flakes were fabricated on 270 nm SiO_2/Si substrate by CVD, with the flakes of varying atomic thickness distributed over the substrate. A commercial Leica microscope (20× objective) and the line-scan hyperspectral imaging system (100× Leica objective) were used to ac-

quire the RGB and hyperspectral images. The measurement parameters were controlled as follows, scanning speed as 100 µm/s, step size of 5 µm, the waiting time of 0.1 s for camera capture. The scanning time for a region of 200 × 80 µm^2 was 30 seconds, with a high spectral resolution of 0.728 nm/px. To reduce the dimensions of the data set and extract the important spectral information, 251 channels (507-689 nm) were selected from the original 1004 channels (325-1056 nm). The dimension reduction of the original hyperspectral data set required fewer computation resources. Considering that the characteristic spectra of MoS_2 flakes were dependent on the atomic layer number, oxidation thickness of the SiO_2/Si substrate, illumination conditions, and the numerical aperture of microscope objectives, the microscope objective and the illumination conditions were kept unchanged during the measurement.

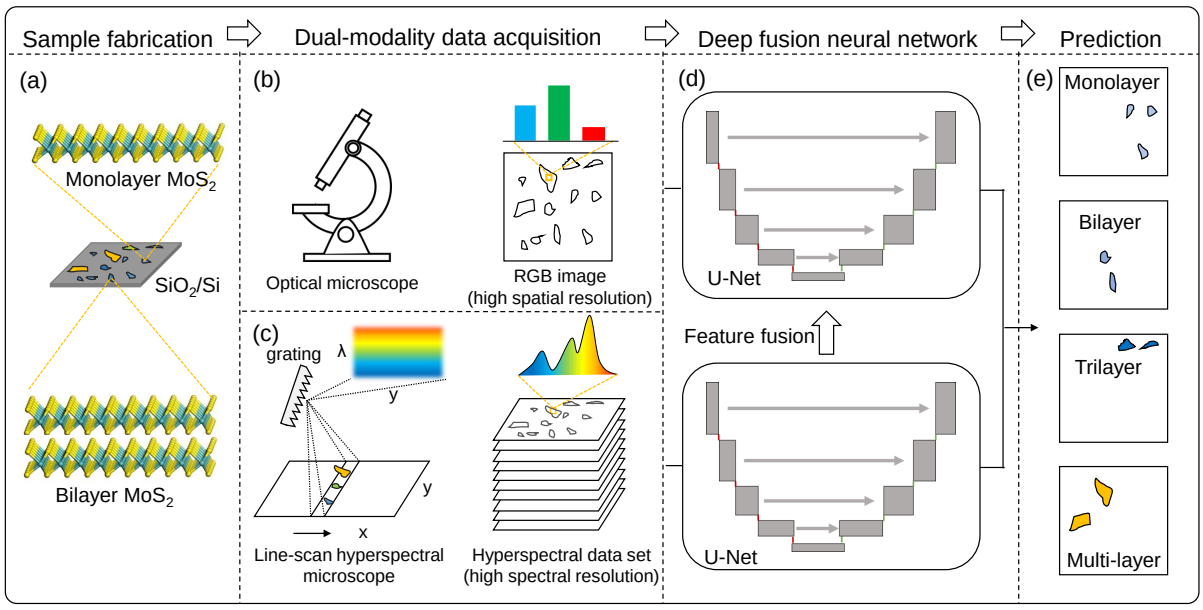

Figure 6.1: The work flow from 2D materials fabrication, RGB and hyperspectral data acquisition using optical microscopy and line-scan hyperspectral microscopy, deep fusion neural network processing, and the prediction of layer number maps.

Before the acquired data were fed into the deep fusion network, data pre-processing (data smoothing, background subtraction, and channel selection) was conducted to the hyperspectral data set to lower the noise, correct the inhomogeneity of the illumination, and extract the useful information from the redundant hyperspectral raw data. To transforming the RGB images (3 channels) and the hyperspectral images (251 channels after dimension reduction) into one coordinate system, the dual-modality data of the same region were co-registered using a feature-based method in the MATLAB environment. Due to different camera sources, the two types of images had different scales and coordinates. Data normalization was used to change the different scales of data sets into the same

value range, without distorting variations in this value range. Data augmentation was adopted to recreate the new data based on the original data set and enlarge the training data.

The registered RGB images with high spatial resolution and hyperspectral images with high spectral resolution were paired and employed as two inputs of the deep fusion neural network. The single-stream U-Net (the "U"-shape architecture) was first designed for medical image segmentation with a small number of training sets [259]. In this work, both hyperspectral images and RGB images were employed as network inputs, and therefore, a dual-stream U-Net was modified from the single-stream U-Net to extract high-spatial-resolution information from RGB images and high-spectral-resolution information from hyperspectral images, separately. In the training process, the labeled masks (target outputs) which contained the correct layer maps were fed jointly with the RGB images and hyperspectral images of 8 regions which contained more than 40 flakes with varying layer numbers into the network. After data augmentation, the training data sets included 48 image pairs, each pair containing 3-channel RGB images and 251-channel hyperspectral images. The network parameters were optimized by the iterative gradient descent to minimize the differences between the true outputs and the expected outputs. In the testing process, 5 new pairs of co-registered hyperspectral data sets and RGB images of 5 regions containing more than 20 MoS_2 flakes were put into the network, and the network estimated atomic layer maps. Through this deep fusion network, every pixel of the imaged area was classified into a sub-class (monolayer, bilayer, trilayer, multi-layer, or background/substrate), and thus the pixel-level image fusion was achieved. For comparison, a single-stream U-Net architecture was built, trained, and tested using only the RGB images from the paired data for layer number mapping. The performances of the deep fusion neural network and the single U-Net were compared.

6.2 Data Pre-processing and Post-processing

6.2.1 Registration of RGB and Hyperspectral Images

Feature-based algorithms were used for dual-modality image registration based on the correspondence between image features such as points, lines, and contours. Due to the high spatial resolution of the optical microscope, the RGB image was referred to as the fixed image (reference image) while the hyperspectral image was referred to as the moving image. The geometric transformation was applied to moving images so that the hyperspectral image could be aligned with the reference. The whole image registration could be divided into three steps. First, corresponding points between moving and fixed images were selected. Second, the transformation relation according to the corresponding

points was determined. Third, the geometrical transformation was applied to the moving image. By Image Processing Toolbox from MATLAB, the corresponding points between two images could be selected through the "Control Point Selection Tool".

Figure 6.2 shows the interface of the "Control Point Selection Tool". The left side is the hyperspectral image and the right side is the optical RGB image. The geometric transformation was defined by a rule where the point with Cartesian coordinates (x, y) was mapped to another point with Cartesian coordinates (u, v). The affine transformation was used and the equation can be described as:

$$[u \quad v] = [x \quad y \quad 1]\,T \tag{6.1}$$

T was a 3-by-3 transformation matrix, where all six elements of the first and second columns could be different. The third column was $[0, 0, 1]$. The transformation matrix T could be determined through the corresponding points.

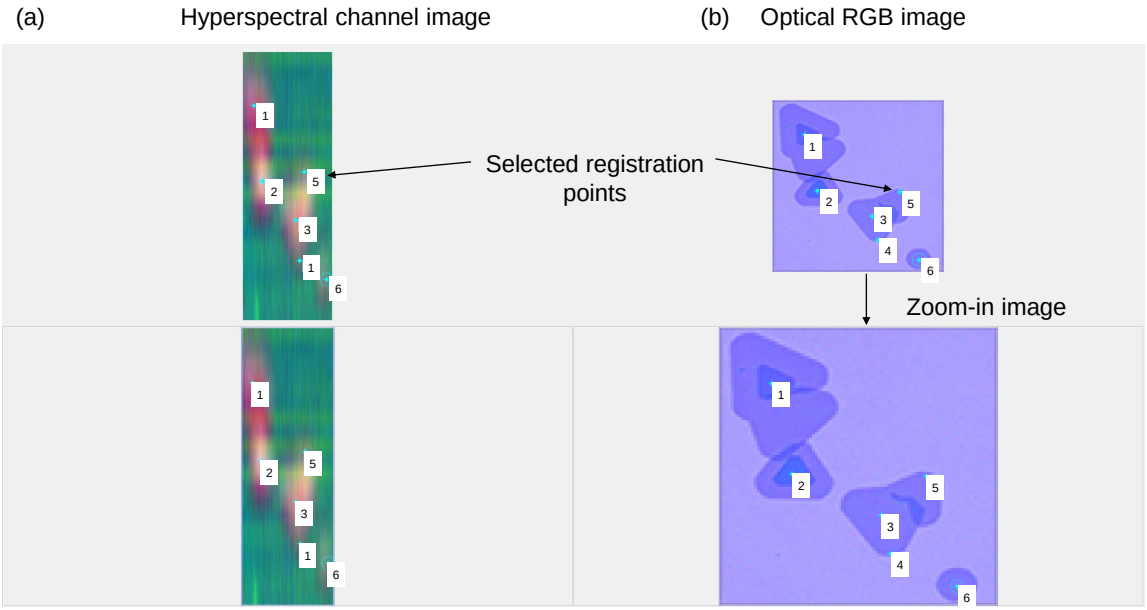

Figure 6.2: GUI for images registration in the MATLAB environment.

6.2.2 Data Normalization

There were two input variables including RGB images and hyperspectral images acquired from different optical modalities. The value of 8-bit RGB images ranged $[0, 255]$, while the intensity of hyperspectral data ranged $[0, 20]$. To fuse the features from both inputs and balance the attributions from both small and large values, min-max normalization

was introduced to rescale the range of RGB and hyperspectral images to $[0, 1]$. By this data normalization, the training speed of the network could be improved and the contrast of the images could be enhanced. Min-max normalization was employed to rescale the range of RGB and hyperspectral images to $[0, 1]$, and the equation is described as below.

$$X = \frac{x_i - x_{min}}{x_{max} - x_{min}} \tag{6.2}$$

where x_{max} and x_{min} are the maximum and minimum values of the matrix.

6.2.3 Data Labeling

The training of the network required not only the registered data pairs, but also the target data (manual annotations). The parameters of the network would be optimized to predict outputs that were as much as similar to the labeled target data. The data labeling was conducted manually in the MATLAB environment. Figure 6.3 shows the GUI for data labeling, where four sub-classes (monolayer, bilayer, trilayer, and multi-layer) were set and the corresponding regions in the optical images were circled with different colors. After the flakes were labeled, the regions without labeling were set as the fifth sub-class of background. The pixels of the regions were labeled with different values. For example, the background pixels were labeled with value zero, the monolayer pixels were labeled with value one, the bilayer pixels are labeled with value two, and so forth. Figure 6.4 illustrates optical RGB images and the pixel values after labeling. After this process, the labeled data had different pixel values as a classification to sub-classes. In the training process of the network, one-hot images for each sub-class were required. Therefore, the labeled data with different pixel values should be converted to one-hot images, where only 0 and 1 could be used to label pixel values. Pixel value 0 means the pixels were not classified as this sub-class while pixel value 1 meant the pixels were classified as this sub-class (Figure 6.5). Five one-hot images corresponding to the five sub-classes were obtained after the conversion. The one-hot images would be used as annotated data for training the network.

Due to the pre-processing operations onto the hyperspectral data and RGB data, the dimension changes of the raw data to the data pairs suitable for network training was summarized (Figure 6.6). The acquired hyperspectral data set contained 1004 spectral channels and the dimension was reduced to 251 channels after the redundant channels were removed. The hyperspectral data set and the corresponding RGB images captured from the same region were registered with 254 channels. The annotated one-hot images were used as masks. The hyperspectral data set, RGB images, and the masks were combined as one pair for network training.

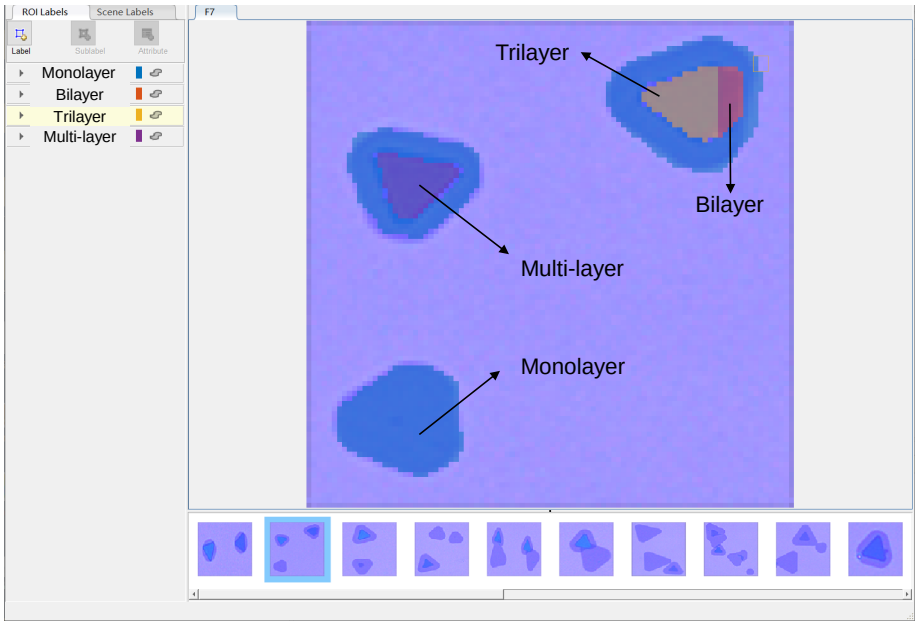

Figure 6.3: Graphic user interface (GUI) for images labeling.

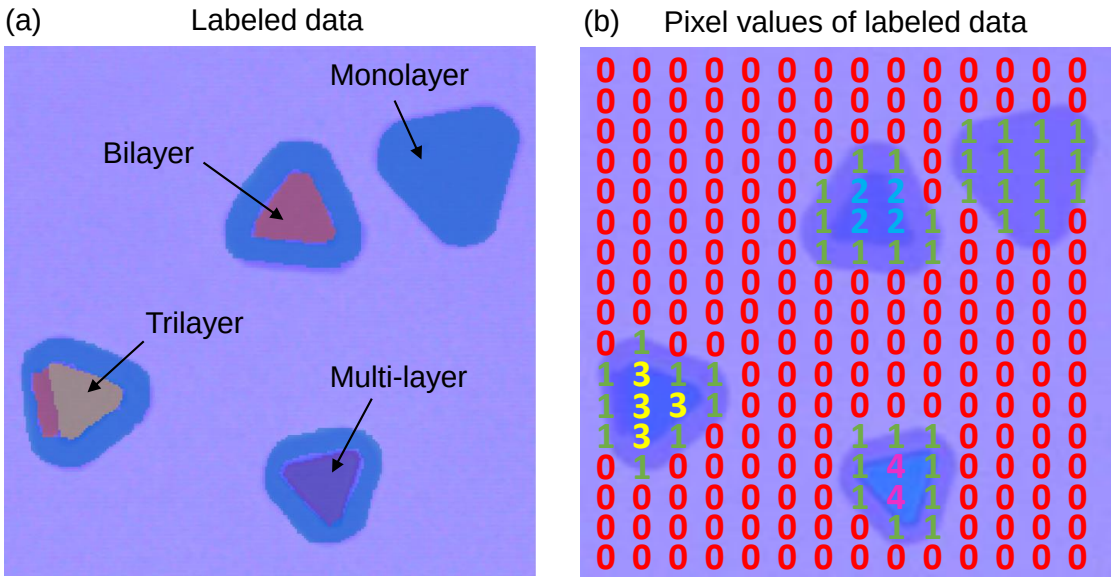

Figure 6.4: Labeled data and pixels with different values showing different layer numbers.

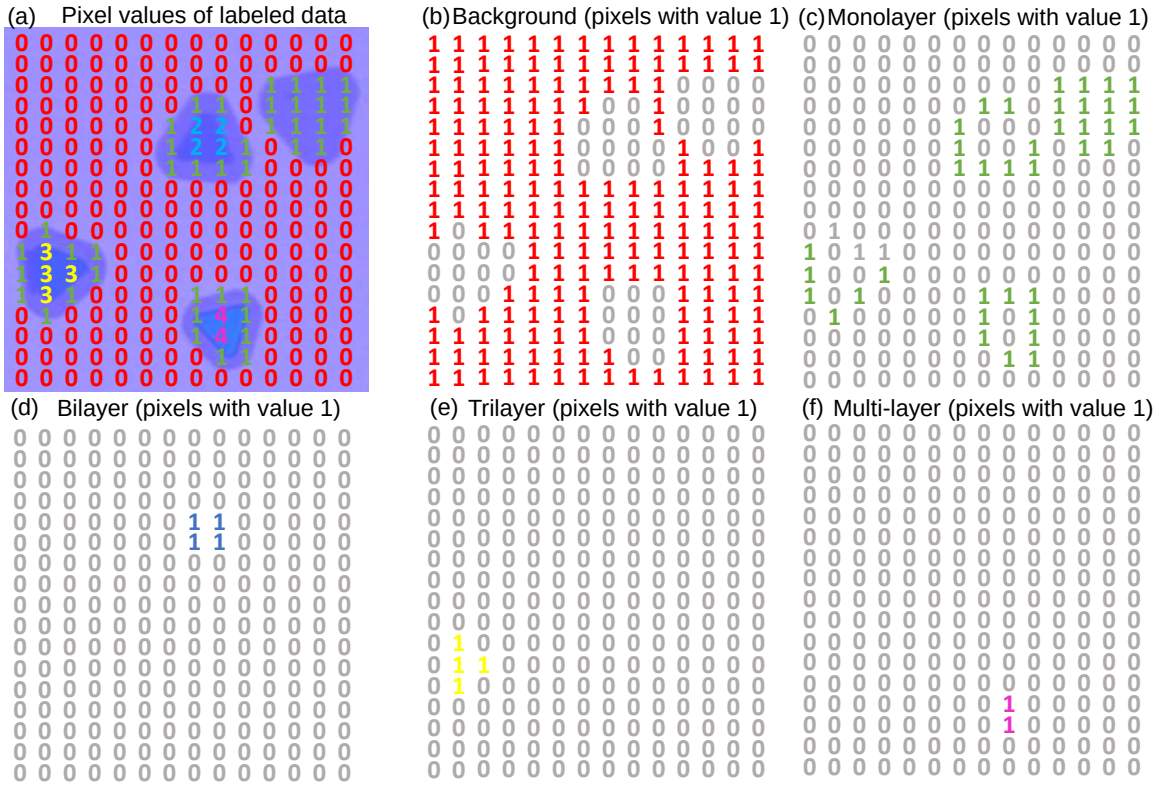

Figure 6.5: Labeled data and the converted one-hot images of different layer numbers.

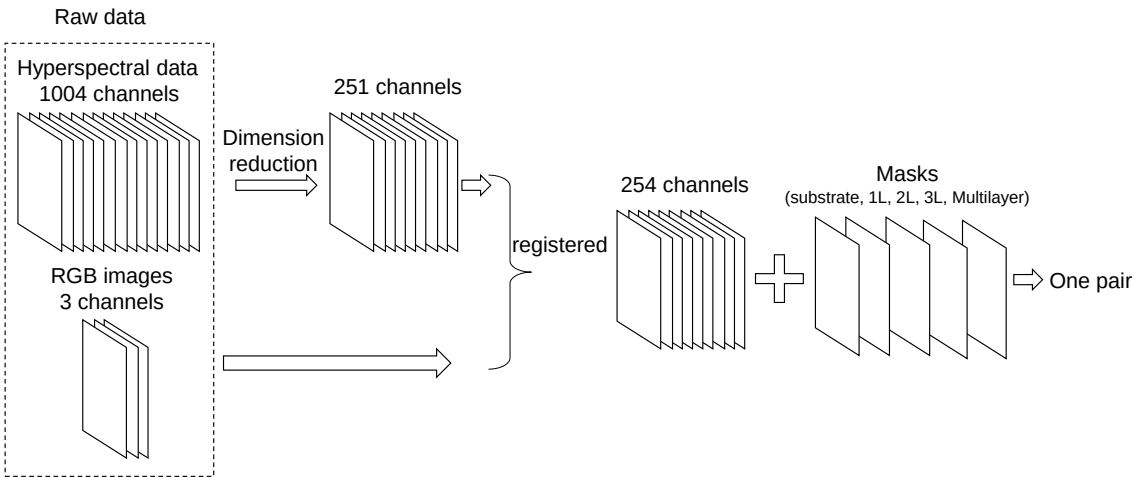

Figure 6.6: Data dimension changes from raw data to paired data for training.

6.2.4 Data Augmentation

Basic operations of data augmentation include flip, rotation, scale, crop, translation, and brightness changes of the original data sets. At the beginning of the training, the augmented data were considered as different and unique images. Data augmentation strategy was used to improve the robustness of the network and prevent over-fitting during the training process. The whole sample sets involved 8 pairs of registered hyperspectral and optical images acquired from 13 different regions containing more than 40 MoS_2 flakes with varying layer numbers. After data augmentation, the total number of registered pairs for training was 48, containing more than 240 flakes with different layer numbers. The same data augmentation operations were conducted on the hyperspectral data set, RGB images, and the masks of the same data pair (Figure 6.7).

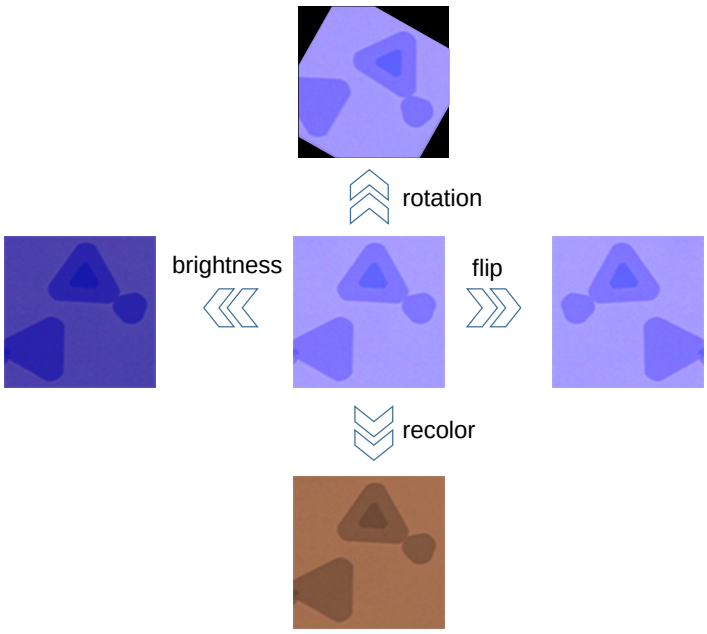

Figure 6.7: Data augmentation operations.

6.2.5 Data Post-processing

False predictions contained noisy points, which could influence the network performances such as dice score, Hausdorff distance, and confusion matrix. To eliminate the noise points, post-processing was carried out for improving the overall performance of the network. Connected Component Analysis (CCA), which is usually used in computer vision to detect and count the number of connected regions, was employed to eliminate the noise points of prediction results. First, eight-neighbor representation (all eight pixels around one pixel is considered connected components) was used to detect the connected pix-

els. Second, a threshold for the minimum size of a blob was set. If a connected blob was smaller than the threshold, this blob was defined as noise points and would be eliminated.

6.3 Network Architecture, Training, and Testing

6.3.1 Network Architecture

The deep fusion network was based on the FCN which extracted the hierarchical image features of data sets and achieved pixelwise semantic segmentation. Figure 6.8 illustrates the structure of the deep fusion network, which consisted of 6 different blocks, namely "conv3d" block, "maxpooling3d" block, "up-sampling2d" block, "conv2d" block, "max-pooling2d" block, and "features fusion" block. The network included a contraction part (left) and an expansion part (right). The contraction part had a two-stream structure where RGB images (2D) and hyperspectral images (3D) were fed jointly into the network. As the dimensions of network inputs were different, 2D convolutions and 3D convolutions were operated separately in the two network streams. In 2D convolutions, convolutional filters (3×3) moved in both directions (x, y) to calculate low dimensional features from the image data, with a 2D matrix as output, while in 3D convolutions, 3D filters ($3 \times 3 \times 1$) were applied to the data set and the filter moved in all direction (x, y, z) to calculate the low-level feature representations, with a 3D cube as the output. Both the 2D and 3D convolution block performed the downsampling operation and extracted 2D and 3D feature maps from RGB and hyperspectral images, separately.

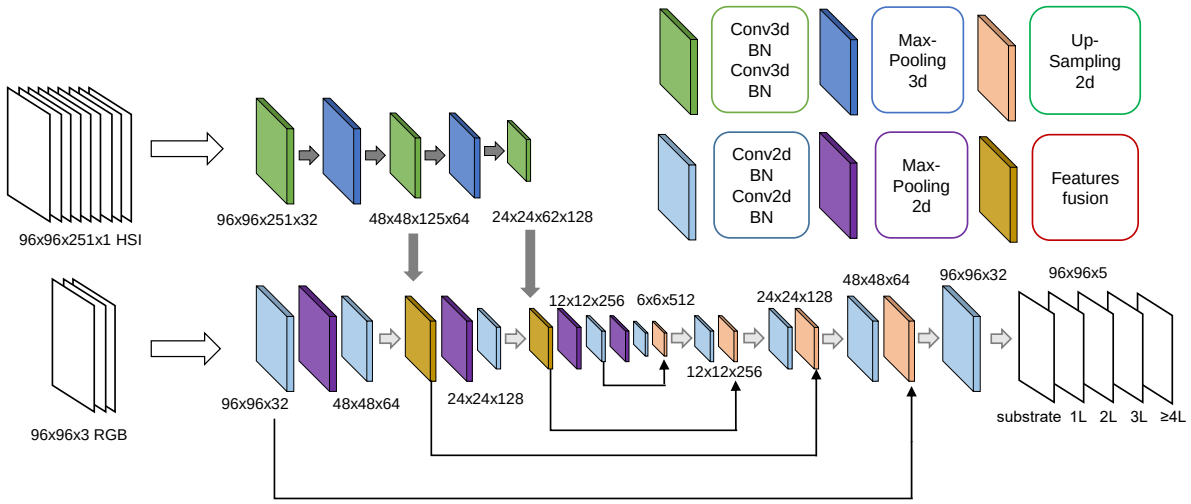

Figure 6.8: Deep fusion neural network architecture.

The 2D and 3D features were combined through the feature fusion, which integrated the hyperspectral information from 3D data set into the spatial information from 2D images

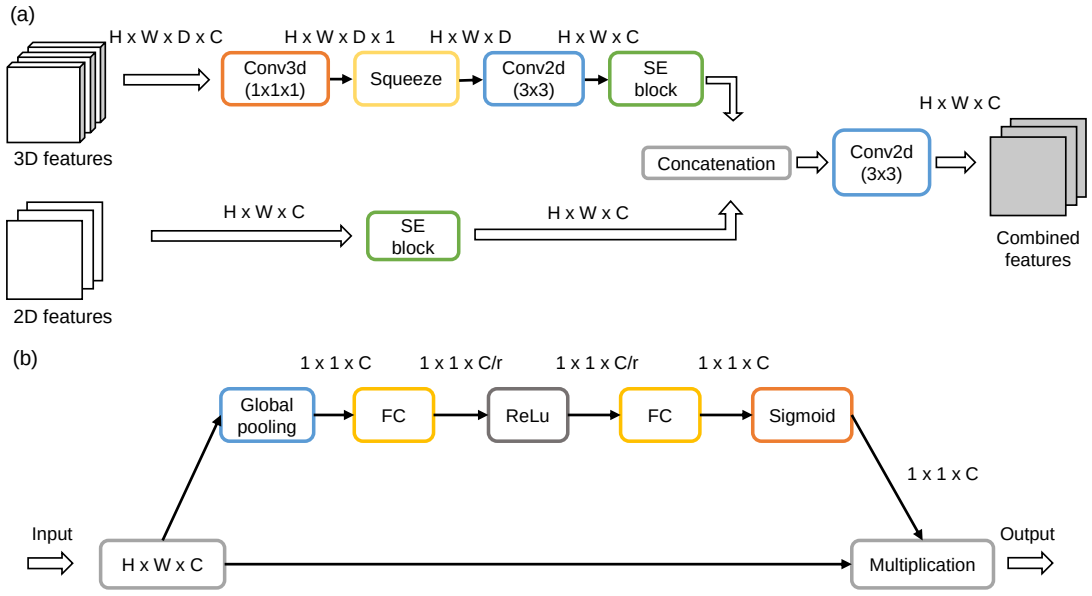

Figure 6.9: Fusion blocks (a) Three main parts including dimension reduction of 3D features, channel excitation (SE block) and features concatenation. (b) Structure of the SE block of weighing the feature map channels based on their importance.

in an optimal fusion strategy. At the same time, the 2D spatial information from hyperspectral images was also extracted through this process. The expansion section remained the same structure as the original S-U-Net. The D-U-Net output a 2D predicted image, of which the number of channels corresponded to the number of segmented classes (substrate, monolayer, bilayer, trilayer, and multi-layer). The convolution layers (contraction part) were repeated, with a ReLu activation function and a max-pooling for each layer.

Due to dimension differences between 3D and 2D features, features fusion block was employed to combine them optimally. The core of the features fusion block was to reduce the dimension of 3D features into 2D. The dimensions of 3D and 2D features could be expressed as $H \times W \times D \times C$ and $H \times W \times C$, where $H \times W$ represented the feature dimensions of height and width, D represented the depth of 3D feature, and C represented the feature channel. To transform the dimension of 3D features into 2D, channel C of 3D features was compressed into 1 using the $(1 \times 1 \times 1)$ 3D convolution. The dimension of channel-compressed 3D features was further processed through squeeze and (3×3) 2D convolution operations to become $H \times W \times C$, which is consistent with 2D feature (Figure 6.9(a)).

To optimize the effect of fused features, squeeze-and-excitation (SE) block was applied before concatenation. By automatic learning, the block could acquire the importance of each feature channel, enhance the useful features, and supress the less important ones (Figure 6.9(b)). Global average pooling layer was used as squeeze operation. Features

were compressed along the spatial dimension into $1 \times 1 \times C$. That means, each 2D feature channel was turned into a real number, which to some extent had a global receptive field. To reduce parameters and computational complexity, the feature channel was reduced from C to C/r, where r denoted the reduction ratio. After ReLu activation layer and fully connected layer, the feature channel could be ascended to C again. Sigmoid layer was used for the excitation operation.The weight could be generated for each feature channel through parameter w, which was learned to described the correlation between feature channels. Through sigmoid, the normalized weights between 0 and 1 could be obtained. Finally, through a scale operation, the normalized weights could be weighted to the features of each channel.

Loss functions were used to determine the error between the output of the network and the given target value. In deep learning, there are different types of loss functions for selection according to neural networks tasks. Cross-entropy as one of the most common loss functions in classification models, and mean squared error (MSE) is usually used as loss function for regression tasks. In our image segmentation task, dice loss was employed as the loss function to measure the overlap of two images. Compared to cross-entropy, dice loss performed better in class unbalanced situations where background occupied much more pixels than flake areas.

In data label process of data pre-processing, the segmentation labels were converted into one-hot label to obtain the binary target masks. Since the number of mask channels corresponded the number of prediction classes, dice loss could be calculated for each class. In this case, predicted probabilistic maps and manual annotation target masks had 5 channels and each channel represented a prediction class. Therefore, dice loss could be calculated class by class. Assume y_{true} was the manual annotation target mask, while y_{pred} was the predicted probabilistic maps. Then dice loss function could be expressed by the following equation:

$$DiceLoss = 1 - \frac{2\sum_{pixels} |y_{true} \circ y_{pred}| + s}{\sum_{pixels} (|y_{true}| + |y_{pred}|) + s} \tag{6.3}$$

where $\circ$ represents the entrywise product of two matrices. The s term is set to 1 in order to avoid the division by 0. For example, without s term, if both y_{true} and y_{pred} are zero, the fraction part will be invalid.

6.3.2 Batch Normalization

In the data pre-processing, RGB and hyperspectral inputs with different range scales were normalized to share the same value scale. Normalization could be conducted in the

hidden layers of the network because the values changed with convolution and pooling operations. In this deep fusion network, the batch normalization was added behind the convolution operation to speed up training and improve the performance of the neural network. The whole batch normalization operation could be divided into 4 steps. Assume that the input of a batch in a layer of the neural network was $X = [x_1, x_2, \ldots, x_n]$, where x_i represented one sample and n was batch size. First, the mean value of the elements in mini-batch can be found by:

$$\mu_B = \frac{1}{n} \sum_{i=1}^{n} x_i \tag{6.4}$$

Next, the variance of mini-batch was calculated as:

$$\sigma_B^2 = \frac{1}{n} \sum_{i=1}^{n} (x_i - \mu_B)^2 \tag{6.5}$$

Each element could be normalized as:

$$x_i' = \frac{x_i - \mu_B}{\sqrt{\sigma_B^2 + \epsilon}} \tag{6.6}$$

where ϵ was added in the denominator for numerical stability and was an arbitrarily small constant.

Finally, the data was re-scaled and shifted to recover the original distribution. The transformation step of batch normalization follows as:

$$y_i = \gamma_i \cdot x_i' + \beta_i \tag{6.7}$$

where γ and β are two trainable parameters to each layer, so the normalized output x_i' is multiplied by a standard deviation (γ) and added by a mean (β) .

6.3.3 Training and Testing

After the augmentation, RGB images with different orientation, 8 pairs ($96 \times 96 \times 251$ hyperspectral images and $96 \times 96 \times 3$ RGB images for each pair) were used for training the neural network (training set) and 5 pairs with the same dimensions were used for testing and evaluating the performance of the network (testing set). Each pair covered a sample region (50×50 µm^2 to 80×80 µm^2) which contained at least two types of MoS_2 flakes. The framework for training stages of both models are shown in Figure 6.10. The models

were trained in the environment based on i9 9900K CPU, 64GB RAM, Nvidia RTX2080 Super (8GB), CUDA 10.2+cudnn 7.6. The training optimizer was "Adam", the learning rate was set $2e^{-4}$, and the batch size was set as 1, with 250 epochs.

Figure 6.11 shows the learning curves of both neural networks. The x-axis represents the number of epochs for training and the y-axis represented the dice loss during the training process. Both the training and validation loss continued to decrease with the training epochs and both of them tended to convergence in the end. The training and validation loss decreased fast in the first 20 epochs. Specifically, it can be observed that there was a little gap between the train and validation loss learning curves and this gap was referred to as the generalization gap (Figure 6.11(b)). This plot shows the good fit learning curves which means the models were well trained during the process.

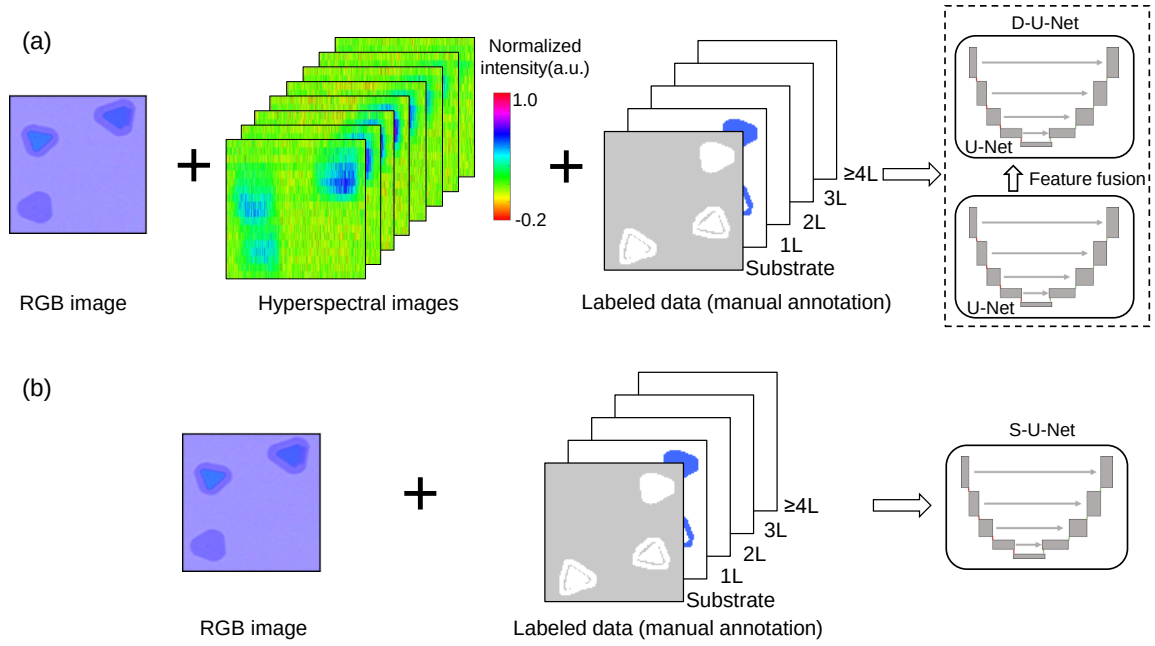

Figure 6.10: The framework of training stages of D-U-Net and S-U-Net models.

6.4 Prediction Performances and Quantitative Evaluation

6.4.1 Prediction Results

To evaluate the prediction performance of the D-U-Net, 5 new pairs of hyperspectral and RGB images captured at 5 regions containing more than 20 MoS_2 flakes were used for demonstration. The prediction results of S-U-Net which was trained and tested using only

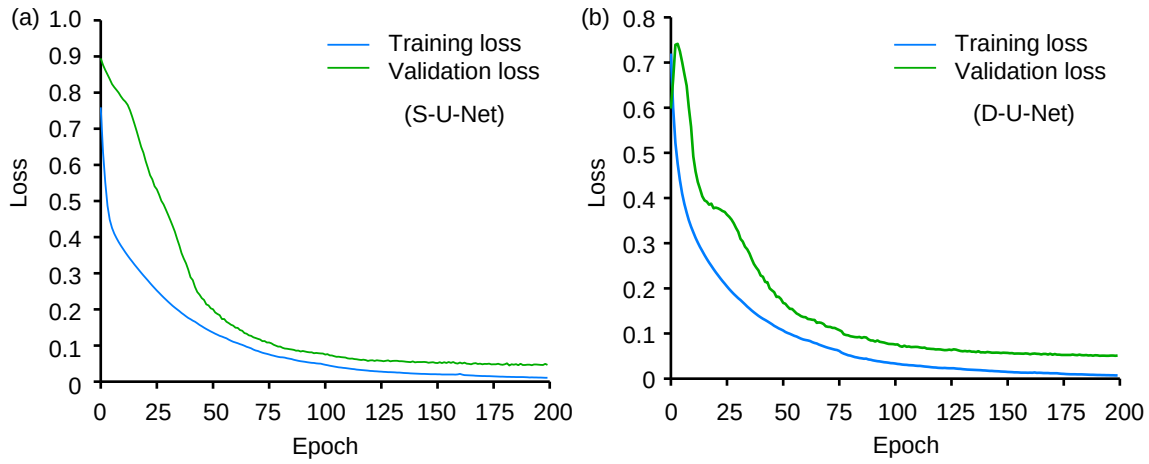

Figure 6.11: Learning curves of (a) S-U-Net and (b) D-U-Net.

RGB images are shown for comparison. The test was designed as a cross test using regions containing MoS_2 flakes with different layer number combinations. Each test pair contains at least three from the five sub-classes (background, monolayer, bilayer, trilayer, and multi-layer). Figure 6.12 shows the optical images of five test regions with the sub-classes of each flake as a reference. (a)-(e) are the optical image of these regions, respectively. Figures 6.12-6.16 illustrate the segmentation results of the test data using D-U-Net and S-U-Net, where the labeled manual annotations, the D-U-Net prediction results, and the S-U-Net prediction results for each sub-class are shown together.

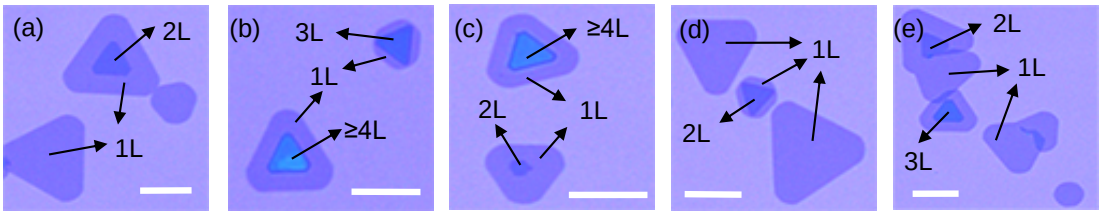

Figure 6.12: The optical images of five test samples. (a)-(e) are the optical image of these regions, respectively. Scale bar= 20 µm.

In Figure 6.13, the test sample contains monolayer and bilayer flakes. The background and monolayer regions were correctly identified by both D-U-Net and S-U-Net, and the profiles of different flakes are consistent with those of the reference. However, the bilayer region which can be distinguished by the D-U-Net was misidentified as trilayer by the S-U-Net. S-U-Net is kind of confusing to classify bilayer and trilayer pixels.

In Figure 6.14, the test sample contains monolayer, trilayer, and multi-layer regions. The background and the monolayer flakes can be correctly identified by both D-U-Net and S-

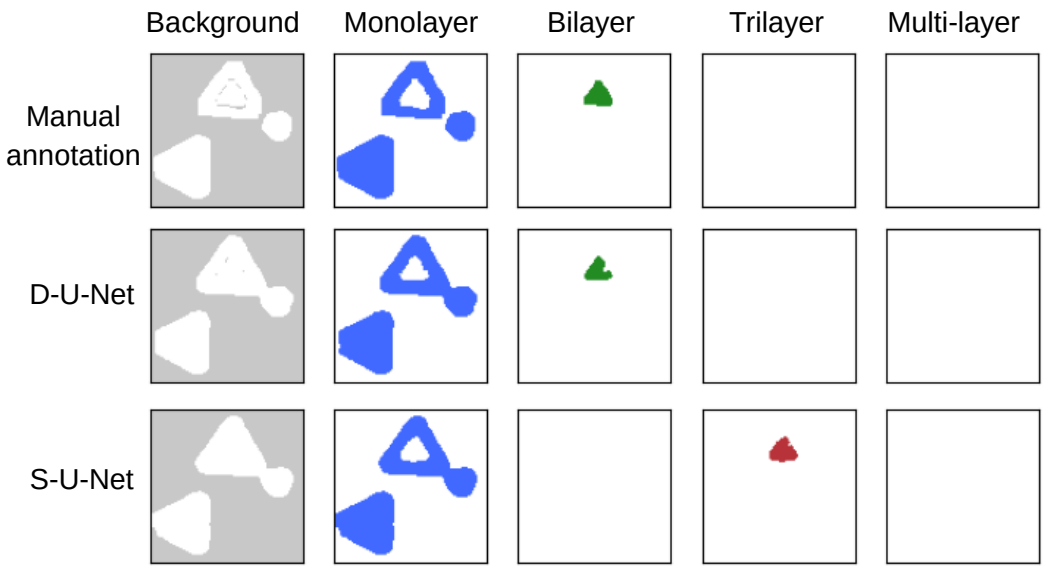

Figure 6.13: Prediction results of the distribution maps of substrate, monolayer, bilayer, trilayer, and multi-layer flakes by the deep fusion network and the single-stream U-Net (Figure 6.12 (a)).

U-Net. The different performance is that trilayer and multi-layer flakes can be successfully identified by the D-U-Net, while S-U-Net takes trilayer and multi-layer as one sub-class. S-U-Net is also confusing about the features of trilayer and multi-layer pixels.

In Figure 6.15, the test sample contains monolayer, bilayer, and multi-layer regions. The background and the monolayer flakes can be correctly identified by both D-U-Net and S-U-Net. D-U-Net can output correct layer number identification and accurate flake profiles of bilayer and multi-layer regions. S-U-Net misclassifies the bilayer and multi-layer pixels as trilayer sub-classes, and some multi-layer pixels are misclassified as the bilayer sub-class. S-U-Net is confusing about the bilayer, trilayer, and multi-layer features.

In Figure 6.16, the test sample contains monolayer and bilayer regions. Both D-U-Net and S-U-Net networks can identify background and monolayer regions with high prediction accuracy. For bilayer region identification, D-U-Net and S-U-Net can identify and predict the bilayer pixels. The difference lies in the profile output accuracy, which will be quantitatively analyzed in the following section. Compared to Figure 6.13, the S-U-Net shows randomness to correctly identify bilayer regions, which is unreliable for application.

In Figure 6.17, the test sample contains monolayer, bilayer, and trilayer regions, and looks more complicated than the former four samples. Both D-U-Net and S-U-Net networks can identify background and monolayer regions with high prediction accuracy. D-U-Net can output correct layer number identification and accurate flake profiles of bilayer and

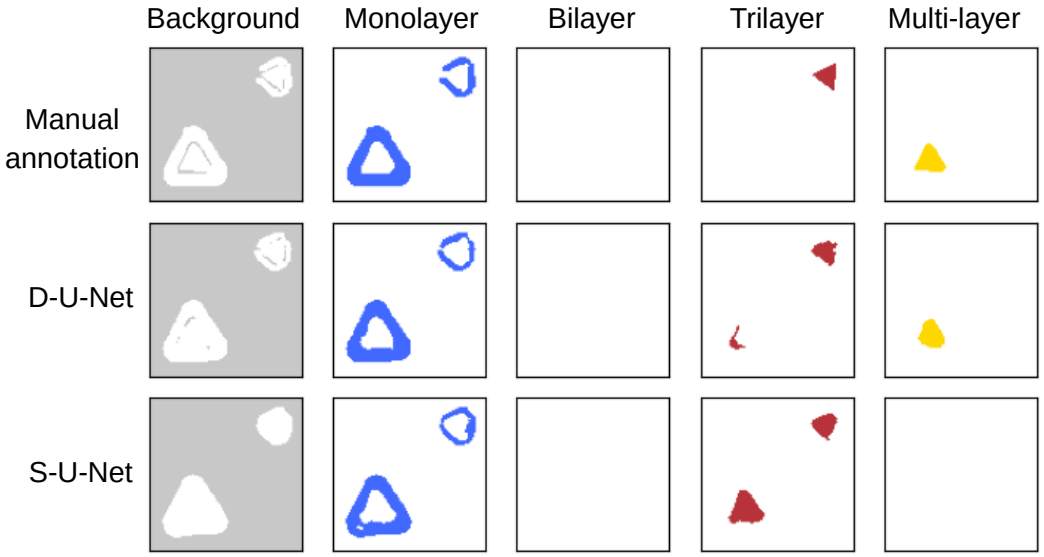

Figure 6.14: Prediction results of the distribution maps of substrate, monolayer, bilayer, trilayer, and multi-layer flakes by the deep fusion network and the single-stream U-Net (Figure 6.12 (b)).

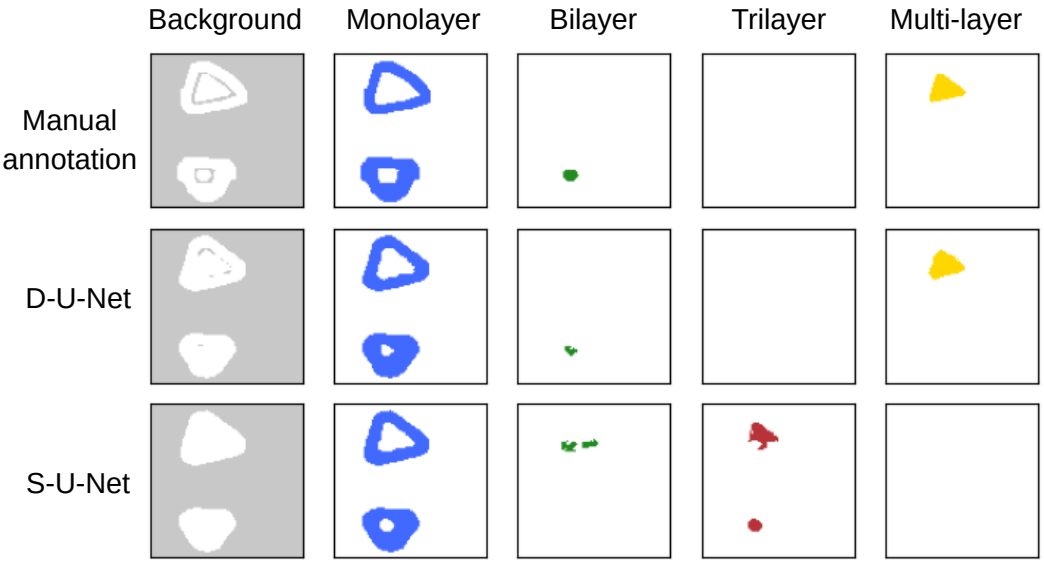

Figure 6.15: Prediction results of the distribution maps of substrate, monolayer, bilayer, trilayer, and multi-layer flakes by the deep fusion network and the single-stream U-Net (Figure 6.12 (c))

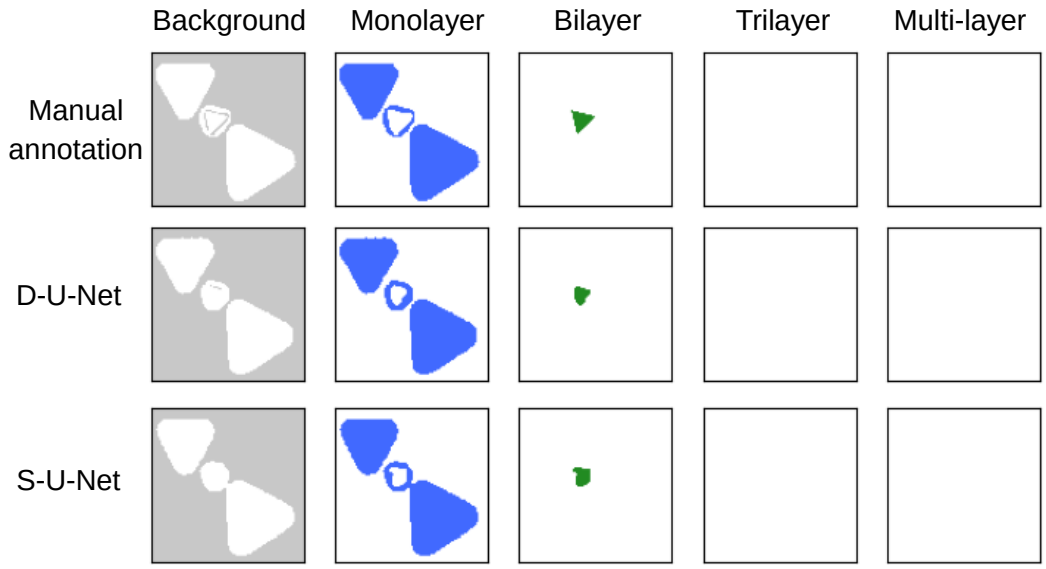

Figure 6.16: Prediction results of the distribution maps of substrate, monolayer, bilayer, trilayer, and multi-layer flakes by the deep fusion network and the single-stream U-Net (Figure 6.12 (d)).

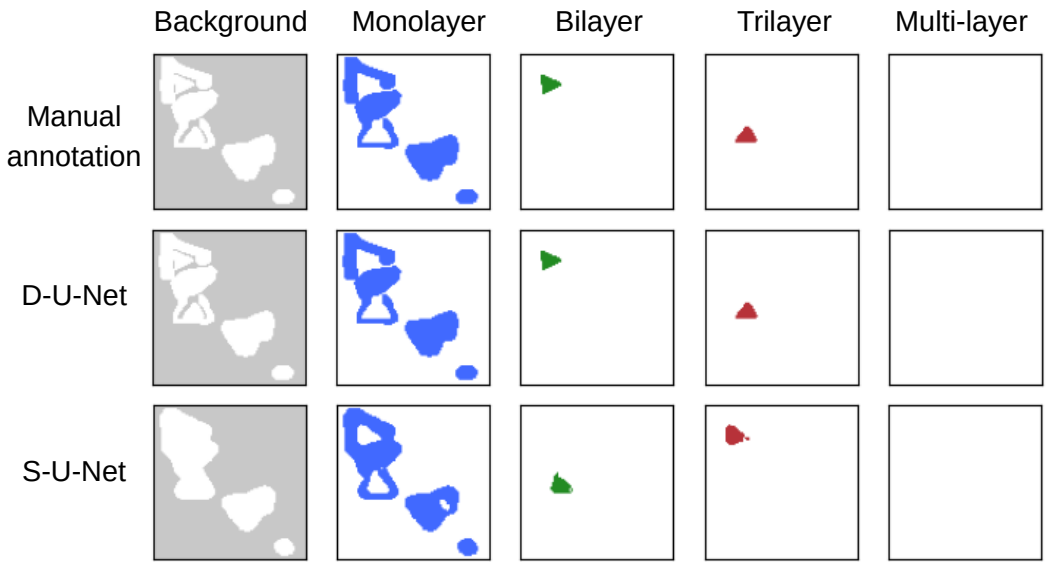

Figure 6.17: Prediction results of the distribution maps of substrate, monolayer, bilayer, trilayer, and multi-layer flakes by the deep fusion network and the single-stream U-Net (Figure 6.12 (e)).

trilayer regions, while S-U-Net misclassifies bilayer pixels to the trilayer sub-class and the trilayer pixels to the bilayer sub-class. According to the direct observation of the network prediction performances, it can be concluded that, both D-U-Net and S-U-Net can identify background and monolayer regions with high accuracy. D-U-Net achieves better prediction success rate when identifying bilayer, trilayer, and multi-layer regions while S-U-Net is confusing about bilayer, trilayer, and multi-layer sub-classes.

6.4.2 Quantitative Evaluation

To quantitatively analyze the prediction performances of both networks, dice similarity coefficient (DSC), Hausdorff distance (95^{th} percentile), and confusion matric were employed to evaluate the layer number identification and flake region segmentation results.

First, DSC was calculated to assess the overlapping accuracy of network predictions. The DSC could be defined as two times the correct prediction, divided by the sum of the areas of manual annotations and prediction results using the following equation.

$$DSC = \frac{2\,(G \cap P)}{|G| + |P|} \tag{6.8}$$

Where G is the labeled pixel set of each sub-class (manual annotations), and P is the predicted pixel set of each sub-class (prediction). The closer is the score to 1, the better the performance of successful prediction (Figure 6.18(a)). Figure 6.18(b) shows the calculated DSC values of D-U-Net and S-U-Net. Both models had a high DSC value (above 90%) in the segmentation of background and monolayer sub-classes. However, S-U-Net achieved 21.8%, 20.1%, and 3.3% in segmentation of bilayer, trilayer, multi-layer sub-classes, separately. The predicted distribution maps of each sub-classes (bilayer, trilayer, and multi-layer) had a very limited overlapping region with the labeled annotation, which was mainly due to the similar color contrast among these layers. D-U-Net achieved 77.5%, 70.3%, and 91.9% accuracy when classifying pixels into the correct sub-classes. With the introduction of hyperspectral images that provided abundant spectral information, D-U-Net could better distinguish different layers, and the RGB images ensured the accurate localization of each sub-class. The mean DSC values of D-U-Net and S-U-Net were 88.3% and 60.5%, separately, which meant that the overall performance was improved by 28% by imagery fusion.

Second, Hausdorff distance was calculated to assess the localization accuracy of the network prediction. Hausdorff distance is defined by the following equation, which calculates the longest distance between one point of a set to all the points of the other set.

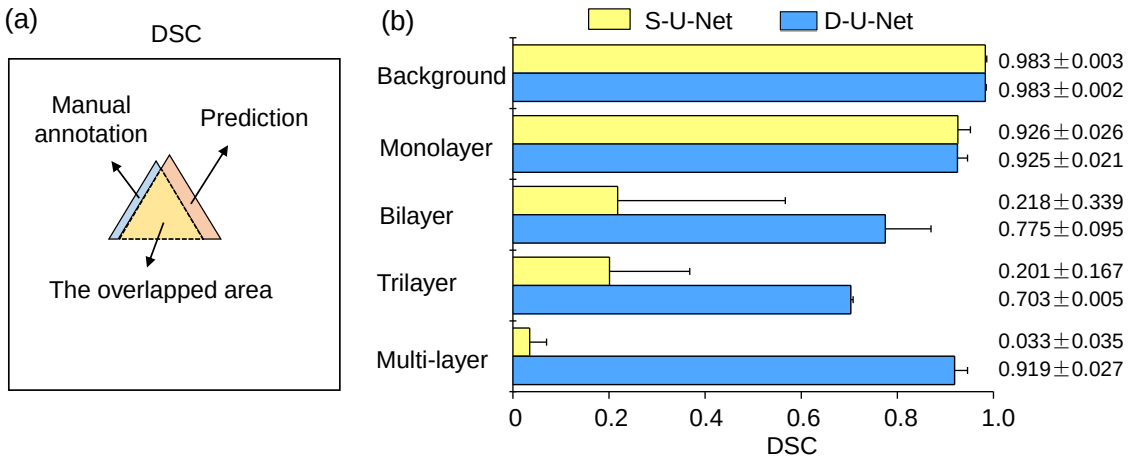

Figure 6.18: Evaluation of the dice similarity coefficient. (a) Diagram. (b) The calculated values of S-U-Net and D-U-Net models.

$$H(G,P) = max\left\{ \sup_{x\in G} \inf_{y\in P} d(x,y), \sup_{y\in P} \inf_{x\in G} d(x,y) \right\} \tag{6.9}$$

where G is the manual annotation set, and P is the prediction set, while x and y are the points from both sets, respectively.

In practice, to eliminate the influence from random noise points, 95^{th} percentile Hausdorff distance (HD95) was employed instead of the maximum (100^{th} percentile). As the HD95 represented the absolute distance between two point sets, the large value meant the predicted flake area was far from the labeled area. Figure 6.19(a) shows the diagram of Hausdorff distance calculation and Figure 6.19(b) illustrates the calculated values of both models. For S-U-Net, the values of background and monolayer classes were not large, which meant a good prediction compared with the target data. However, the distances for bilayer, trilayer, and multi-layer predictions had large values of 32.411 px, 58.776 px, and 14.488 px, separately. For D-U-Net, the distance values for background, monolayer, bilayer, and multi-layer sub-classes were 4.353 px, 2.051 px, 2.562 px, and 1.751 px, separately. Only the trilayer sub-class had a large value of 40.708 px, which was mainly due to one wrongly predicted area in Figure 6.14.

Third, to understand how the pixels of one sub-class were misclassified to another sub-class, the confusion matrix of both models were calculated to visualize the performance of classification. Each row of the matrix represented the instances in a predicted class, while each column represented the instances in an actual class. Different from the dice score, the confusion matrix made it easy to see if the system was confusing of two or more classes. Since both models performed well in background and monolayer segmentation, we mainly

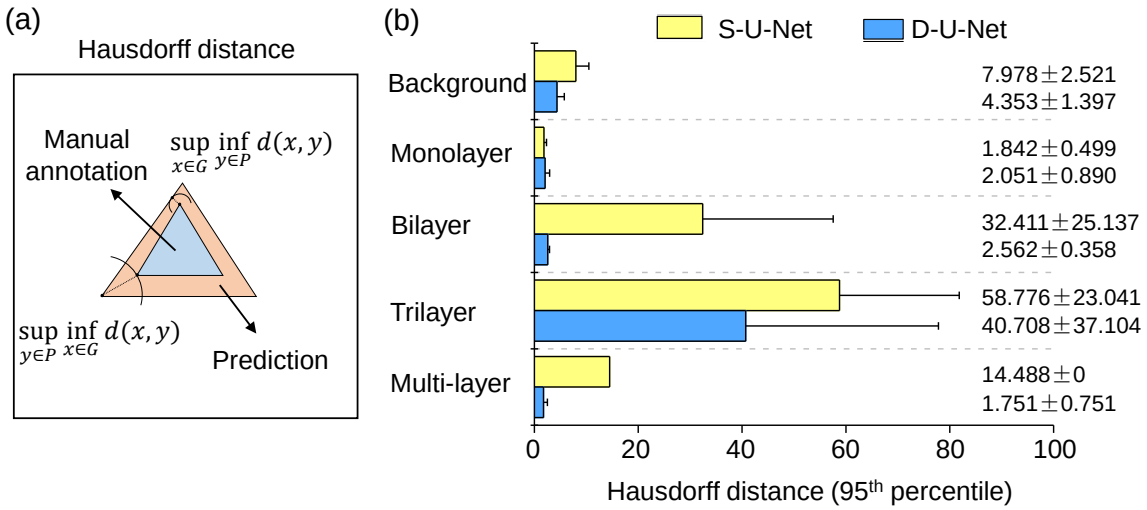

Figure 6.19: Evaluation of the Hausdorff distance. (a) The diagram of Hausdorff distance. (b) Evaluation results of Hausdorff distance (95^{th} percentile).

focused on bilayer, trilayer, and multi-layer sub-classes. From the confusion matrix of S-U-Net (Figure 6.20(a)), only 20% bilayer pixels were classified correctly, and 69% bilayer pixels were misclassified as trilayer. 43% trilayer pixels were misclassified as bilayer sub-class. 80% multi-layer pixels were classified as trilayer sub-class incorrectly. From the confusion matrix of D-U-Net (Figure 6.20(b)), the misclassified pixels only accounted for a small proportion (around 5%), except one case that around 20% bilayer pixels were misclassified as the monolayer sub-class. The S-U-Net model was confusing with bilayer, trilayer, and multi-layer sub-classes while D-U-Net was more intelligent with these sub-classes. The confusion matrix of S-U-Net was compared with the previous reports (the confusion matric of D-U-Net was not compared because no reports have been published so far). In a recent report where flakes with 2-6 layers as one sub-class, the VGG16 network could reach 99% and 74% accuracy in segmenting background and monolayer sub-classes, and 61% in segmenting the few-layer (2-6 layers) sub-class [61]. In our case, if 2-6 layers were combined as one sub-class, a higher accuracy could be reached (90%).

The deep fusion neural network with RGB microscope images and hyperspectral microscope images as two inputs could distinguish and segment MoS_2 flakes with monolayer to multi-layer thickness with high accuracy, which cannot be achieved by the single-input network using only RGB microscope images. The deep fusion neural network possessed both advantages of two inputs with high spatial and spectral resolution. Although the single U-Net neural network which used only RGB images acquired by optical microscopes had bad performances for bilayer, trilayer, and multi-layer identification, this model could be useful for some specific circumstances. For example, this network can be used for a

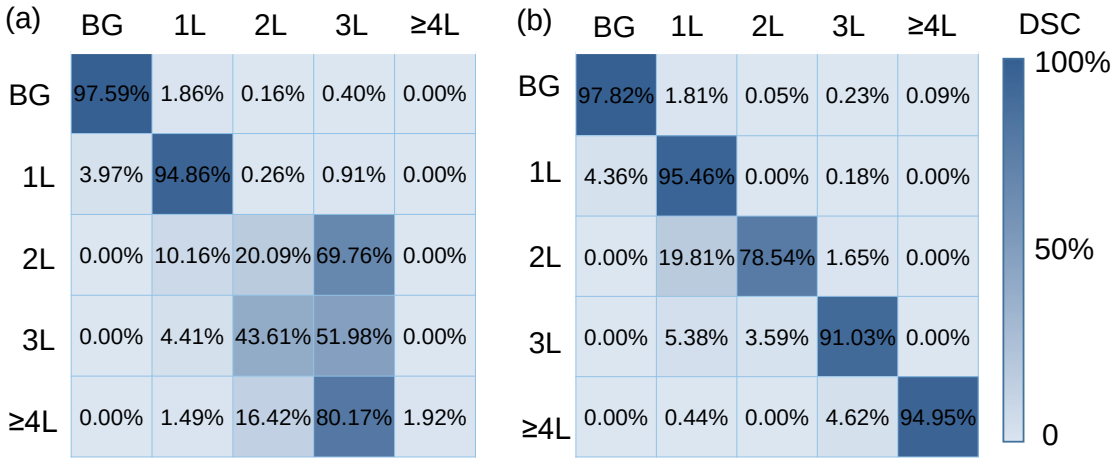

Figure 6.20: Confusion matrix of S-U-Net (a) and D-U-Net (b) for segmenting monolayer, bilayer, trilayer, multi-layer, and background sub-classes.

rough classification of flakes with three categories including monolayer, few-layer (2-10 layers), and bulk flakes. The acquisition of training data sets, network training and testing, real working speed, can be advantageous than the deep fusion neural network which demands more work. For circumstances where accurate atomic layer numbers of flakes are desired, deep fusion neural network shows much better performances than single U-Net architecture, and thus is more practical for real applications. MoS_2 flakes on 270 nm SiO_2/Si substrates are used for proof-of-concept demonstration. The deep fusion network can also be further implemented to other 2D materials with different oxidation thickness of SiO_2/Si substrates, which requires measurements of more samples for network training. The current work can be further adapted by research groups for their own specific applications. This dual-stream U-Net network can also be used to a hybrid microscope with two cameras which can obtain the high-spatial-resolution color images and high-spectral-resolution hyperspectral images at the same time.

6.4.3 Model Generalizability Analysis

To evaluate the predictive performance of D-U-Net to generalize to illumination and contrast variation, which is essential for practical applications, we perform leave-one-sample-out for cross validation. Specifically, we used the sample IDs to split the data set into training, validation and test sets. There were 13 different samples available. In each split, we used data from 10 samples for training, 2 samples for validation and the data from the remaining sample for testing. This procedure was repeated until all of the samples were used as testing. We did leave-one-sample-out in two scenarios: a) 20% hyperspectral illumination variation, constant RGB illumination; b) 20% hyperspectral

illumination, and 10% contrast variation in RGB images.

For comparison, only the five regions which were previously employed as testing pairs (Figure 6.12) are shown in Figure 6.21. The image segmentation results of monolayer were mostly consistent with the manual annotations, while mistaken predictions happened for bi-, tri-, and multi-layer in both leave-one-sample-out predictions. For example, the bilayer region (green) in Figure 6.21(a) was mis-identified as trilayer in the first leave-one-sample-out operation (20% hyperspectral illumination variation, constant RGB illumination), and was correctly identified in the second leave-one-sample-out operation (20% hyperspectral illumination variation, 10% RGB contrast variation).

The shown five images were chosen as comparison and could not represent all the other samples. Therefore, the statistical results based on all the samples are illustrated in Figure 6.22. In the constant RGB illumination case, the median DSC was 98.1% (substrate), 93.7% (monolayer), 81.7% (bilayer), 79.6% (trilayer), and 92.6% (multi-layer) (Figure 6.22(a)), showing the predictive stability compared to the previous values (blue in Fig. 6.18(b)). At the same time, in the 10% RGB contrast variation case, the DSC values for substrate (98.1%) and monolayer (93.9%) were close to those of the constant illumination case, and a decrease in bilayer (69.7%), trilayer(64.5%), and multi-layer (89.4%) occurred (Figure 6.22(a)). HD95 (blue in Figure 6.19(b)) was more stable in the leave-one-sample-out evaluation, while contrast variation (10%) increased the deviation when classifying bilayer pixels (Figure 6.22(b)).

The confusion matrices of both leave-one-sample-out calculations were acquired using the median values. The predictions of the constant illumination case (Figure 6.23(a)) was highly consistent with the previous results (Figure 6.20(b)), while for 10% contrast variation case, the uncertainty increased when identifying bilayer and trilayer (Figure 6.23(b)), indicating the bilayer and trilayer was the most confusing sub-classes. Through this analysis, cross-validation showed that D-U-Net had a stable statistical performance; a constant illumination condition when capturing RGB microscope images was important to ensure a higher rate of accurate identification, especially for bilayer and trilayer flakes.

6.5 Summary

A dual-stream U-Net neural network was proposed to fuse RGB images (high spatial resolution) and hyperspectral images (high spectral resolution) for identification and segmentation of atomic layer flakes with monolayer, bilayer, trilayer, and multi-layer thickness grown by the CVD method. The deep fusion network could be trained using a small number of samples, reaching high accuracy (>80%) and one-layer precision for atomic layer identification. A quantitative comparison showed advantageous performances of the deep

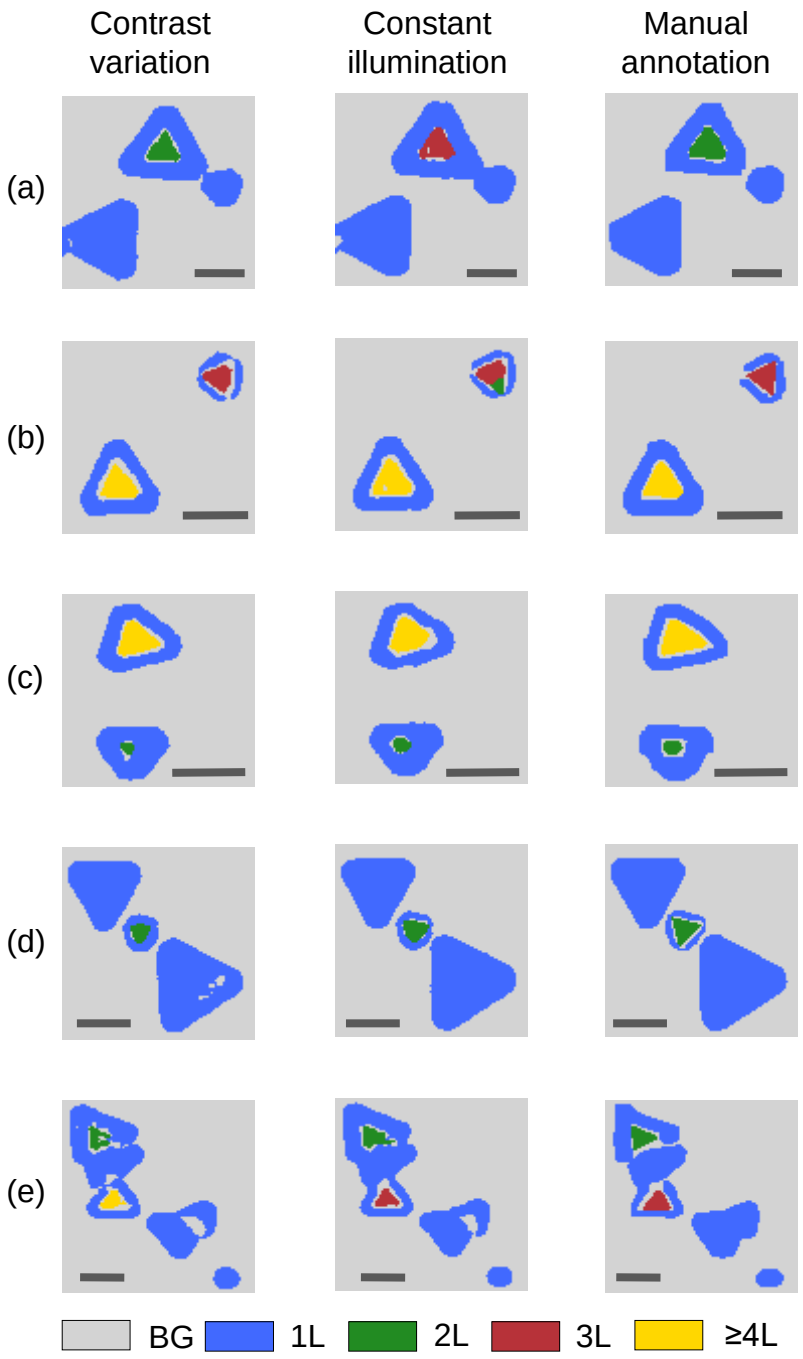

Figure 6.21: Segmentation results of leave-one-sample-out evaluation using the same five regions in Figure 6.12 for comparison, under conditions of contrast variation (10%) and constant illumination. Scale bar=20 µm.

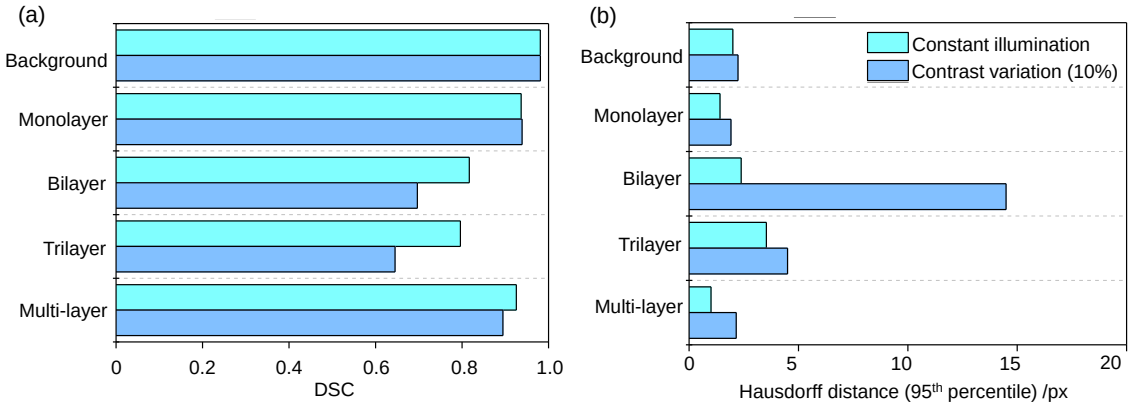

Figure 6.22: DSC values and HD95, under both constant illumination and 10% contrast variation conditions.

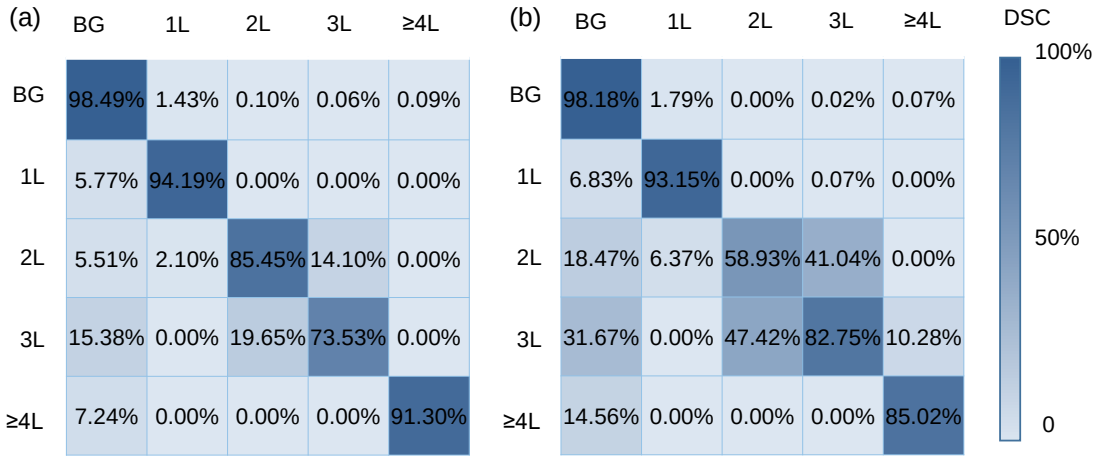

Figure 6.23: Confusion matrices of constant illumination (a) and 10% contrast variation (b).

fusion network over the single-stream U-Net which used only RGB microscope images. This AI-supported technique with high speed, high spatial resolution, and high accuracy has the potential to replace repeated manual work of 2D materials characterization.

Chapter 7

Conclusion and Outlook

7.1 Conclusion

In this thesis, a line-scan hyperspectral imaging microscope system including a line-scan hyperspectral imaging microscope, system control, data acquisition graphic user interface, and data processing algorithms, was custom built for 2D layer number identification. The control and image acquisition of the system worked in the MATLAB environment. The microscale spatial resolution of the line-scan hyperspectral imaging microscope (horizontal resolution better than 228 lp/mm and vertical resolution of 5 µm/pixel) was sufficient for the characterization of distinct micron-sized 2D flake areas, considering that the sizes of few-layer and monolayer crystals are several to tens of microns in the lateral dimension [260]. The line-scan hyperspectral imaging microscopy is advantageous for rapid 2D materials measurements.

To process and understand the multidimensional data sets of semiconducting MoS_2 flakes acquired by the custom-built hyperspectral imaging microscope, image processing algorithms for reconstructing the layer maps were developed from manual interpretation (MATLAB environment) to machine-learning-based methods (Python environment).

To develop the manual interpretation method, two classification strategies including linear unmixing analysis and differential reflectance analysis, were used to determine the spatial distribution of different areas with varying thicknesses. The comparative study proved the linear unmixing an effective tool for accurate thickness mapping. Line-scan hyperspectral imaging microscopy with linear unmixing was employed to characterize MoS_2 and hBN flakes fabricated by the mechanical exfoliation by processing the multidimensional data sets. Pixel-level spectral analysis was used to extract the pure spectra of the monolayer and few-layer flakes. These pure spectra were employed as end members to conduct

the linear unmixing of the hyperspectral data sets. The reconstructed abundance maps showed the distribution and accurate positions of different flakes, realizing automated search and identification within a large area in several minutes. To test the identification limit of the proposed spectral unmixing method, a practical hyperspectral-library-assisted method was further investigated for rapid layer number mapping of CVD-grown MoS_2 samples, reaching the one-atomic-layer resolution. The hand-crafted library, which used extracted characteristic spectra of different flakes as components, was utilized to quantitatively identify and map the distribution of distinct flakes from a newly-measured sample with unknown thickness distribution. This method has applications in 2D materials investigations using this pixelwise-classification-based mapping method.

To further develop an intelligent system for fully automated large-area layer number mapping of 2D materials, a dual-stream U-Net neural network was proposed to fuse RGB images (high spatial resolution) and hyperspectral images (high spectral resolution) for identification and segmentation of atomic layer MoS_2 flakes with monolayer, bilayer, trilayer, and multi-layer thickness grown by the CVD method. The deep fusion network was trained using a small number of samples, reaching high accuracy (>80%) and one-layer precision for atomic layer identification. A quantitative comparison showed advantageous performances of the deep fusion network over the single-stream U-Net which used only RGB microscope images. This AI-supported technique with high speed, high spatial resolution, and high accuracy has the potential to replace repeated manual work of 2D materials characterization.

A summary of the time consumption using the hyperspectral imaging microscopy to reconstruct the layer number maps of different flakes was discussed. For a region of 200×80 μm^2, the measurement and data acquisition required 30 seconds, the data pre-processing including background subtraction and denoising required 3 mins, and the spectral unmixing and spatial distribution reconstruction of each type of flake took 2-3 mins, given that the library has been already built in advance. The time for building such a library was obviously longer since the operator also needed time to search for different types of flakes using an optical microscope and the test of such a library also required time. For the deep-learning-based method, the network took several seconds to predict the layer distribution after being well trained and was suitable for real-time measurement and data processing.

7.2 Outlook

The improvement of the current system includes a higher resolution, higher speed, better robustness, and wider applications. The spectral resolution of the line-scan hyperspectral

system allows for one-layer identification of 2D materials. The spatial resolution for imaging exfoliation 2D flakes (3-5 microns) is not enough to output accurate profiles, which has been resolved by fusing the hyperspectral data sets and the RGB images. The method to improve the spatial resolution is one of the possible ways, where the system can also be designed as a point-scan mode. Then, the main focus is to overcome the time-consuming drawback of the point-scan mode. Usually, when one performance of the system is improved, another performance will be lowered. The improvement of spatial resolution by using point-scan mode brings lower scanning speed. The trade-off depends on the application circumstances. The current system could be designed as Raman hyperspectral microscopy and hyperspectral photoluminescence microscopy as the point-scan mode [261, 262]. The idea of characteristic spectra extraction and specific component mapping can work as well, and fusion is not necessary if the resolution of the hyperspectral images is improved.

The current system can be further developed based on the deep fusion network. The hyperspectral data sets and RGB images are acquired from different modalities. It takes time in the dual-modality data acquisition step, although the network can predict layer maps in a few seconds after being well trained. Therefore, dual modalities can be combined as a hybrid system. A camera can be implemented at the position of observation, where the hyperspectral imager records the hyperspectral data set and the camera captures the RGB images. In this case, the deep fusion neural network works as well, and the time for data acquisition can be reduced.

Another aspect is to improve the robustness of the neural network. The performances of the network are based on the hyperspectral imaging system developed in our lab. If the network is employed to a point-scan hyperspectral imaging system, its parameters need to be re-trained with the new data acquired by the new system. As our hyperspectral imaging microscopy system was built as a demo, the robustness of the neural network can be further investigated when other similar systems are available. The speed can also be improved when the neural network can be well trained using fewer samples. To develop our system in this way, a self-learning network will be investigated.

Not limited to layer number mapping of 2D materials, the hyperspectral imaging method can be utilized for studying heterogeneous properties of 2D materials. Theoretically, when the properties of 2D materials and their heterostructures correspond to their spectral behaviors, the heterogeneous variations in the spatial domain can be resolved and performed using this method which mainly includes featured spectra extraction and abundance map calculation. For example, in the strain engineering of 2D materials, the strain-tuned heterogeneous optical properties of 2D materials can be spatially determined [263, 264].

Appendix A

A.1 List of Symbols

The symbols listed below are applied throughout the entire thesis. The locally used symbols are explained and defined in respective content where they first appear.

$A_{i,j}$	Values of the abundance map matrix
$B_{i,j}$	Values of the abundance map matrix
b_1	Bias of one neuron of the network
DSC	Dice similarity coefficient
EM_i	End members
G	Labelled pixel set by manual annotation
I_i	Pure spectra of flakes
I_k	Reflection intensity of each pixel
P	Predicted pixel set
$P_{i,j}$	Measured spectra of the hyperspectral data set
p	A hyperspectral data set
$R_{intensity}(i, j, \lambda)$	Calculated intensity distribution of point (i, j) at wavelength λ
$R(i, j, \lambda)$	Measured reflection spectra of pixel (i, j)
$R_0(i, j, \lambda)$	Averaged spectra from the bare substrate
T	3-by-3 transformation matrix
$[u \quad v]$	Cartesian coordinates
(w_1, w_2)	Neuron weights of the network
X	Normalized matrix
x_i	Value of the matrix
x_i'	Normalized value of the matrix
(x_1, x_2)	Neuron inputs of the network
$[x \quad y]$	Cartesian coordinates
x_{max}	Maximum value of the normalized matrix

x_{min}	Minium value of the normalized matrix
(y_1, y_2)	Neuron outputs of the network
y_{pred}	Predicted pixel set
y_{true}	Labelled pixel set
z_1	Value before activation function of the neuron
λ	Wavelength
μ_B	Mean value
σ_B^2	Varience
ϵ_B^2	An arbitrarily small constant
γ	Standard deviation (trainable parameters of network layers)
β	Mean value (trainable parameters of network layers)

A.2 List of Abbreviations

1L monolayer

2D two-dimensional

2L bilayer

3L trilayer

AFM atomic force microscopy

AI artificial intelligence

BP black phosphorus

BS beam splitter

BTF Bragg tunable filter

CCD charge-coupled device

CMOS complementary metal oxide semiconductor

CNN convolutional neural network

CVD chemical vapor deposition

CW continuous-wave

DFG difference frequency generator

DFIR discrete frequency infrared

DL deep learning

DSC dice similarity coefficient

D-U-Net dual-stream U-Net network

ECM ellipsometric contrast micrography

FCN fully convolutional network

FETs field-effect transistors

FTCs flexible transparent conductors

FTIR Fourier-transform infrared spectroscopy

GUI graphical user interface

hBN hexagonal boron nitride

ICA independent component analysis

IR infrared

LEDs light-emitting diodes

LSPR localized surface plasmon resonance

MCR-ALS multivariate curve resolution-alternating least squares

ML machine learning

MoS_2 molybdenum disulphide

MSE mean squared error

OAP off-axis parabolic

OR optical rectification

PCA principal component analysis

PL photoluminescence

PTIR photothermal-induced resonance

QCL quantum cascade laser

RM reference mirror

SEM scanning electron microscopy

SERS surface enhanced Raman spectroscopy

SIE spectroscopic imaging ellipsometry

SINS synchrotron infrared nanospectroscopy

SNR signal-to-noise ratio

SWNTs single-walled carbon nanotubes

s-SNOM scattering-type scanning nearfield optical microscopy

S-U-Net single-stream U-Net network

TEM transmission electron microscopy

TERS tip-enhanced Raman spectroscopy

THz terahertz

THz-TDS terahertz time-domain spectroscopy

TMDs transition metal dichalcogenides

tBLG twisted bilayer graphene

VCA vertex components analysis

VNIR visible and the near-infrared

XRD x-ray diffraction

A.3 List of Figures

A.4 List of Tables

Acknowledgment

This dissertation summarizes my Ph.D work since October 2017 at the Institute for Measurement Systems and Sensor Technology (MST) of the Technical University of Munich (TUM). In the last several years, I have received much support to conduct my Ph.D work. Here I would like to express my sincere thanks to you.

I am really grateful to my supervisor Prof. Dr.-Ing. habil. Dr. h.c. Alexander W. Koch for providing such a collaborative and interdisciplinary environment, where colleagues and students at different groups work together and discuss about very interesting topics. I thank Prof. Koch much for the scientific freedom at our institute to do such work which are interesting to me. His support and trust encourage me to go deeper into hyperspectral imaging field. His comments and suggestions also helped me to improve the quality of publications.

I would like to thank our institute manager Dr. Martin Jakobi for his careful help in daily work at MST. His patience and detailed suggestions are beneficial to me in laboratory work, thesis supervision, scientific collaboration, and international mobility. I also thank Ms. Rita von Grafenstein for her detailed work in organizing thesis presentation of my students' and my dissertations.

I want to express my many thanks to Dr. Ali Yetisen at Imperial College London for his guidance in research and publishing work. His trust motivates me to pursue a higher standard of my research work. Many thanks to Dr. Andreas Stier, İnci Güler, and Prof. Jonathan Finley at Walter Schottky Institut and Physik Department at TUM for their support in sample preparation and valuable comments of research work.

I would like to say thank you to my colleagues at MST. Michael Köhler, Dr. Shengjia Wang, Jie Dong, Kun Wang, and Patrick Kienle supported me in both scientific work and daily life. I thank Xinxu Zhao and Xiao Bi at our neighboring Institute of Environmental Sensing and Modeling (ESM) for their help and daily funny stuff. I also thank my supervised students, Zhutong Jiang, Heng Tian, and Zhendong Li for their fantastic thesis work.

I thank my financial support from China Scholarship Council (CSC) during my Ph.D at TUM. Without this support, I couldn't concentrate so much on the research work.

I cannot be more grateful to my family. My parents always support me and care about me. Even you don't quite understand my research work, your careful words about my daily life, about my health, and my moods are definitely best supports to me. I would like to express my deepest appreciation to my wife, Ling Cheng, for your care and patience full of love.

Bibliography

[1] Curtiss O Davis, Jeffrey Bowles, Robert A Leathers, Dan Korwan, T Valerie Downes, William A Snyder, W Joe Rhea, Wei Chen, John Fisher, W Paul Bissett, and Robert Alan Reisse. Ocean PHILLS hyperspectral imager: design, characterization, and calibration. *Optics Express*, 10(4):210–221, 2002.

[2] Junshi Xia, Peijun Du, Xiyan He, and Jocelyn Chanussot. Hyperspectral remote sensing image classification based on rotation forest. *IEEE Geoscience and Remote Sensing Letters*, 11(1):239–243, 2013.

[3] Ramón Moreno, Francesco Corona, Amaury Lendasse, Manuel Graña, and Lênio S Galvão. Extreme learning machines for soybean classification in remote sensing hyperspectral images. *Neurocomputing*, 128:207–216, 2014.

[4] Dimitris Manolakis, Steven Golowich, and Robert S DiPietro. Long-wave infrared hyperspectral remote sensing of chemical clouds: a focus on signal processing approaches. *IEEE Signal Processing Magazine*, 31(4):120–141, 2014.

[5] Lefei Zhang, Liangpei Zhang, Dacheng Tao, Xin Huang, and Bo Du. Hyperspectral remote sensing image subpixel target detection based on supervised metric learning. *IEEE Transactions on Geoscience and Remote Sensing*, 52(8):4955–4965, 2013.

[6] Guangyu Zhao, Mikael Ljungholm, Elin Malmqvist, Giuseppe Bianco, Lars-Anders Hansson, Sune Svanberg, and Mikkel Brydegaard. Inelastic hyperspectral lidar for profiling aquatic ecosystems. *Laser & Photonics Reviews*, 10(5):807–813, 2016.

[7] MA Rodríguez-Conejo and Juan Meléndez. Hyperspectral quantitative imaging of gas sources in the mid-infrared. *Applied Optics*, 54(2):141–149, 2015.

[8] MS Kim, AM Lefcourt, K Chao, YR Chen, Intaek Kim, and DE Chan. Multispectral detection of fecal contamination on apples based on hyperspectral imagery:

Part I. Application of visible and near–infrared reflectance imaging. *Transactions of the ASAE*, 45(6):2027, 2002.

[9] Oliver Wurl. *Practical guidelines for the analysis of seawater*. CRC press, 2009.

[10] Aurélie Jullien, Umberto Bortolozzo, Stefania Residori, Stéphanie Grabielle, Nicolas Forget, and Jean-Pierre Huignard. Phase and group delay control of femtosecond pulses with liquid crystal cells and application to hyperspectral imaging. In *Slow Light, Fast Light, and Opto-Atomic Precision Metrology X*, volume 10119, page 101191B. International Society for Optics and Photonics, 2017.

[11] Martin Halicek, Guolan Lu, James V Little, Xu Wang, Mihir Patel, Christopher C Griffith, Mark W El-Deiry, Amy Y Chen, and Baowei Fei. Deep convolutional neural networks for classifying head and neck cancer using hyperspectral imaging. *Journal of Biomedical Optics*, 22(6):060503, 2017.

[12] Dimitris Manolakis, Eric Truslow, Michael Pieper, Thomas Cooley, and Michael Brueggeman. Detection algorithms in hyperspectral imaging systems: an overview of practical algorithms. *IEEE Signal Processing Magazine*, 31(1):24–33, 2013.

[13] Kin Fai Mak, Changgu Lee, James Hone, Jie Shan, and Tony F Heinz. Atomically thin MoS_2: a new direct-gap semiconductor. *Physical Review Letters*, 105(13):136805, 2010.

[14] Andrea Splendiani, Liang Sun, Yuanbo Zhang, Tianshu Li, Jonghwan Kim, Chi-Yung Chim, Giulia Galli, and Feng Wang. Emerging photoluminescence in monolayer MoS_2. *Nano Letters*, 10(4):1271–1275, 2010.

[15] Andre K Geim and Irina V Grigorieva. Van der waals heterostructures. *Nature*, 499(7459):419–425, 2013.

[16] Kin Fai Mak and Jie Shan. Photonics and optoelectronics of 2D semiconductor transition metal dichalcogenides. *Nature Photonics*, 10(4):216–226, 2016.

[17] Qing Hua Wang, Kourosh Kalantar-Zadeh, Andras Kis, Jonathan N Coleman, and Michael S Strano. Electronics and optoelectronics of two-dimensional transition metal dichalcogenides. *Nature Nanotechnology*, 7(11):699–712, 2012.

[18] Yuan Liu, Nathan O Weiss, Xidong Duan, Hung-Chieh Cheng, Yu Huang, and Xiangfeng Duan. Van der waals heterostructures and devices. *Nature Reviews Materials*, 1(9):1–17, 2016.

[19] KS Novoselov, O A Mishchenko, O A Carvalho, and AH Castro Neto. 2D materials and van der waals heterostructures. *Science*, 353(6298), 2016.

[20] Jie Wang, Minghui Liang, Yan Fang, Tengfei Qiu, Jin Zhang, and Linjie Zhi. Rod-coating: towards large-area fabrication of uniform reduced graphene oxide films for flexible touch screens. *Advanced Materials*, 24(21):2874–2878, 2012.

[21] Nazmul Karim, Shaila Afroj, Sirui Tan, Pei He, Anura Fernando, Chris Carr, and Kostya S Novoselov. Scalable production of graphene-based wearable e-textiles. *ACS Nano*, 11(12):12266–12275, 2017.

[22] Minpyo Kang, Jejung Kim, Bongkyun Jang, Youngcheol Chae, Jae-Hyun Kim, and Jong-Hyun Ahn. Graphene-based three-dimensional capacitive touch sensor for wearable electronics. *ACS Nano*, 11(8):7950–7957, 2017.

[23] Dmitriy Khatayevich, Tamon Page, Carolyn Gresswell, Yuhei Hayamizu, William Grady, and Mehmet Sarikaya. Selective detection of target proteins by peptide-enabled graphene biosensor. *Small*, 10(8):1505–1513, 2014.

[24] Meng-Lin Tsai, Sheng-Han Su, Jan-Kai Chang, Dung-Sheng Tsai, Chang-Hsiao Chen, Chih-I Wu, Lain-Jong Li, Lih-Juann Chen, and Jr-Hau He. Monolayer MoS_2 heterojunction solar cells. *ACS Nano*, 8(8):8317–8322, 2014.

[25] Dattatray J Late, Yi-Kai Huang, Bin Liu, Jagaran Acharya, Sharmila N Shirodkar, Jiajun Luo, Aiming Yan, Daniel Charles, Umesh V Waghmare, Vinayak P Dravid, and C.N.R. Rao. Sensing behavior of atomically thin-layered MoS_2 transistors. *ACS Nano*, 7(6):4879–4891, 2013.

[26] Oriol Lopez-Sanchez, Dominik Lembke, Metin Kayci, Aleksandra Radenovic, and Andras Kis. Ultrasensitive photodetectors based on monolayer MoS_2. *Nature Nanotechnology*, 8(7):497–501, 2013.

[27] Byungjin Cho, Jongwon Yoon, Sung Kwan Lim, Ah Ra Kim, Dong-Ho Kim, Sung-Gyu Park, Jung-Dae Kwon, Young-Joo Lee, Kyu-Hwan Lee, Byoung Hun Lee, Heung Cho Ko, and Myung Gwan Hahm. Chemical sensing of 2D graphene/MoS_2 heterostructure device. *ACS Applied Materials & Interfaces*, 7(30):16775–16780, 2015.

[28] Zongyou Yin, Xiao Zhang, Yongqing Cai, Junze Chen, Jen It Wong, Yee-Yan Tay, Jianwei Chai, Jumiati Wu, Zhiyuan Zeng, Bing Zheng, Hui Ying Yang, and Hua Zhang. Preparation of MoS_2-MoO_3 hybrid nanomaterials for light-emitting diodes. *Angewandte Chemie International Edition*, 53(46):12560–12565, 2014.

[29] Woo Jong Yu, Zheng Li, Hailong Zhou, Yu Chen, Yang Wang, Yu Huang, and Xiangfeng Duan. Vertically stacked multi-heterostructures of layered materials for logic transistors and complementary inverters. *Nature Materials*, 12(3):246–252, 2013.

[30] Fengnian Xia, Han Wang, Di Xiao, Madan Dubey, and Ashwin Ramasubramaniam. Two-dimensional material nanophotonics. *Nature Photonics*, 8(12):899–907, 2014.

[31] P Blake, EW Hill, AH Castro Neto, KS Novoselov, D Jiang, R Yang, TJ Booth, and AK Geim. Making graphene visible. *Applied Physics Letters*, 91(6):063124, 2007.

[32] Zhengyang Cai, Bilu Liu, Xiaolong Zou, and Hui-Ming Cheng. Chemical vapor deposition growth and applications of two-dimensional materials and their heterostructures. *Chemical Reviews*, 118(13):6091–6133, 2018.

[33] Bing Deng, Zhongfan Liu, and Hailin Peng. Toward mass production of CVD graphene films. *Advanced Materials*, 31(9):1800996, 2019.

[34] Yi-Hsien Lee, Xin-Quan Zhang, Wenjing Zhang, Mu-Tung Chang, Cheng-Te Lin, Kai-Di Chang, Ya-Chu Yu, Jacob Tse-Wei Wang, Chia-Seng Chang, Lain-Jong Li, and Tsung-Wu Lin. Synthesis of large-area MoS_2 atomic layers with chemical vapor deposition. *Advanced Materials*, 24(17):2320–2325, 2012.

[35] Ivan V Vlassiouk, Yijing Stehle, Pushpa Raj Pudasaini, Raymond R Unocic, Philip D Rack, Arthur P Baddorf, Ilia N Ivanov, Nickolay V Lavrik, Frederick List, Nitant Gupta, Ksenia V. Bets, Boris I. Yakobson, and Sergei N. Smirnov. Evolutionary selection growth of two-dimensional materials on polycrystalline substrates. *Nature Materials*, 17(4):318–322, 2018.

[36] Hai Li, Jumiati Wu, Xiao Huang, Gang Lu, Jian Yang, Xin Lu, Qihua Xiong, and Hua Zhang. Rapid and reliable thickness identification of two-dimensional nanosheets using optical microscopy. *ACS Nano*, 7(11):10344–10353, 2013.

[37] Wengen Ouyang, Xin-Z Liu, Qunyang Li, Yingying Zhang, Jiarui Yang, and Quanshui Zheng. Optical methods for determining thicknesses of few-layer graphene flakes. *Nanotechnology*, 24(50):505701, 2013.

[38] Dheeraj Golla, Kanokporn Chattrakun, Kenji Watanabe, Takashi Taniguchi, Brian J LeRoy, and Arvinder Sandhu. Optical thickness determination of hexagonal boron nitride flakes. *Applied Physics Letters*, 102(16):161906, 2013.

[39] ZH Ni, HM Wang, Johnson Kasim, HM Fan, Tongxi Yu, Yong Hua Wu, YP Feng, and ZX Shen. Graphene thickness determination using reflection and contrast spectroscopy. *Nano Letters*, 7(9):2758–2763, 2007.

[40] Krishna P Dhakal, Dinh Loc Duong, Jubok Lee, Honggi Nam, Minsu Kim, Min Kan, Young Hee Lee, and Jeongyong Kim. Confocal absorption spectral imaging of MoS_2: optical transitions depending on the atomic thickness of intrinsic and chemically doped MoS_2. *Nanoscale*, 6(21):13028–13035, 2014.

[41] Hong Li, Qing Zhang, Chin Chong Ray Yap, Beng Kang Tay, Teo Hang Tong Edwin, Aurelien Olivier, and Dominique Baillargeat. From bulk to monolayer MoS_2: evolution of Raman scattering. *Advanced Functional Materials*, 22(7):1385–1390, 2012.

[42] Etienne Gaufrès, Stéphane Marcet, Vincent Aymong, Nathalie Y-Wa Tang, Alexandre Favron, Felix Thouin, Charlotte Allard, David Rioux, Nicolas Cottenye, Marc Verhaegen, and Richard Martel. Hyperspectral Raman imaging using bragg tunable filters of graphene and other low-dimensional materials. *Journal of Raman Spectroscopy*, 49(1):174–182, 2018.

[43] Craig M Nolen, Giovanni Denina, Desalegne Teweldebrhan, Bir Bhanu, and Alexander A Balandin. High-throughput large-area automated identification and quality control of graphene and few-layer graphene films. *ACS Nano*, 5(2):914–922, 2011.

[44] Andrea C Ferrari, JC Meyer, Vittorio Scardaci, Cinzia Casiraghi, Michele Lazzeri, Francesco Mauri, Stefano Piscanec, Da Jiang, KS Novoselov, S Roth, and AK Geim. Raman spectrum of graphene and graphene layers. *Physical Review Letters*, 97(18):187401, 2006.

[45] Ayse Berkdemir, Humberto R Gutiérrez, Andrés R Botello-Méndez, Néstor Perea-López, Ana Laura Elías, Chen-Ing Chia, Bei Wang, Vincent H Crespi, Florentino López-Urías, Jean-Christophe Charlier, Humberto Terrones, and Mauricio Terrones. Identification of individual and few layers of WS_2 using Raman spectroscopy. *Scientific Reports*, 3(1):1–8, 2013.

[46] Xin Zhang, Xiao-Fen Qiao, Wei Shi, Jiang-Bin Wu, De-Sheng Jiang, and Ping-Heng Tan. Phonon and Raman scattering of two-dimensional transition metal dichalcogenides from monolayer, multilayer to bulk material. *Chemical Society Reviews*, 44(9):2757–2785, 2015.

[47] Philipp Braeuninger-Weimer, Sebastian Funke, Ruizhi Wang, Peter Thiesen, Daniel Tasche, Wolfgang Viöl, and Stephan Hofmann. Fast, noncontact, wafer-scale, atomic layer resolved imaging of two-dimensional materials by ellipsometric contrast micrography. *ACS Nano*, 12(8):8555–8563, 2018.

[48] S Funke, U Wurstbauer, B Miller, A Matković, A Green, A Diebold, C Röling, and PH Thiesen. Spectroscopic imaging ellipsometry for automated search of flakes of mono-and N-layers of 2D-materials. *Applied Surface Science*, 421:435–439, 2017.

[49] Chanyoung Yim, Maria O'Brien, Niall McEvoy, Sinéad Winters, Inam Mirza, James G Lunney, and Georg S Duesberg. Investigation of the optical properties of MoS_2 thin films using spectroscopic ellipsometry. *Applied Physics Letters*, 104(10):103114, 2014.

[50] Andreas Hutzler, Christian D Matthus, Christian Dolle, Mathias Rommel, Michael PM Jank, Erdmann Spiecker, and Lothar Frey. Large-area layer counting of two-dimensional materials evaluating the wavelength shift in visible-reflectance spectroscopy. *The Journal of Physical Chemistry C*, 123(14):9192–9201, 2019.

[51] Samuel M Hornett, Rayko I Stantchev, Martha Z Vardaki, Chris Beckerleg, and Euan Hendry. Subwavelength terahertz imaging of graphene photoconductivity. *Nano Letters*, 16(11):7019–7024, 2016.

[52] Peter Bøggild, David MA Mackenzie, Patrick R Whelan, Dirch H Petersen, Jonas Due Buron, Amaia Zurutuza, John Gallop, Ling Hao, and Peter U Jepsen. Mapping the electrical properties of large-area graphene. *2D Materials*, 4(4):042003, 2017.

[53] Jonathan Long, Evan Shelhamer, and Trevor Darrell. Fully convolutional networks for semantic segmentation. In *Proceedings of the IEEE Conference on Computer Vision and Pattern Recognition*, pages 3431–3440, 2015.

[54] Erick Moen, Dylan Bannon, Takamasa Kudo, William Graf, Markus Covert, and David Van Valen. Deep learning for cellular image analysis. *Nature Methods*, pages 1–14, 2019.

[55] Ross Girshick, Jeff Donahue, Trevor Darrell, and Jitendra Malik. Rich feature hierarchies for accurate object detection and semantic segmentation. In *Proceedings of the IEEE Conference on Computer Vision and Pattern Recognition*, pages 580–587, 2014.

[56] Alberto Garcia-Garcia, Sergio Orts-Escolano, Sergiu Oprea, Victor Villena-Martinez, Pablo Martinez-Gonzalez, and Jose Garcia-Rodriguez. A survey on deep learning techniques for image and video semantic segmentation. *Applied Soft Computing*, 70:41–65, 2018.

[57] Satoru Masubuchi and Tomoki Machida. Classifying optical microscope images of exfoliated graphene flakes by data-driven machine learning. *npj 2D Materials and Applications*, 3(1):1–7, 2019.

[58] Eliska Greplova, Carolin Gold, Benedikt Kratochwil, Tim Davatz, Riccardo Pisoni, Annika Kurzmann, Peter Rickhaus, Mark H Fischer, Thomas Ihn, and Sebastian D Huber. Fully automated identification of two-dimensional material samples. *Physical Review Applied*, 13(6):064017, 2020.

[59] Yu Saito, Kento Shin, Kei Terayama, Shaan Desai, Masaru Onga, Yuji Nakagawa, Yuki M Itahashi, Yoshihiro Iwasa, Makoto Yamada, and Koji Tsuda. Deep-learning-based quality filtering of mechanically exfoliated 2D crystals. *npj Computational Materials*, 5(1):1–6, 2019.

[60] Satoru Masubuchi, Eisuke Watanabe, Yuta Seo, Shota Okazaki, Takao Sasagawa, Kenji Watanabe, Takashi Taniguchi, and Tomoki Machida. Deep-learning-based image segmentation integrated with optical microscopy for automatically searching for two-dimensional materials. *npj 2D Materials and Applications*, 4(1):1–9, 2020.

[61] Bingnan Han, Yuxuan Lin, Yafang Yang, Nannan Mao, Wenyue Li, Haozhe Wang, Kenji Yasuda, Xirui Wang, Valla Fatemi, Lin Zhou, et al. Deep-learning-enabled fast optical identification and characterization of 2D materials. *Advanced Materials*, page 2000953, 2020.

[62] Gary A Roth, Sahil Tahiliani, Nicole M Neu-Baker, and Sara A Brenner. Hyperspectral microscopy as an analytical tool for nanomaterials. *Wiley Interdisciplinary Reviews: Nanomedicine and Nanobiotechnology*, 7(4):565–579, 2015.

[63] T Taubner, F Keilmann, and R Hillenbrand. Nanoscale-resolved subsurface imaging by scattering-type near-field optical microscopy. *Optics Express*, 13(22):8893–8899, 2005.

[64] Markus Brehm, Thomas Taubner, Rainer Hillenbrand, and Fritz Keilmann. Infrared spectroscopic mapping of single nanoparticles and viruses at nanoscale resolution. *Nano Letters*, 6(7):1307–1310, 2006.

[65] Rachel E O'Brien, Bingbing Wang, Stephen T Kelly, Nils Lundt, Yuan You, Allan K Bertram, Stephen R Leone, Alexander Laskin, and Mary K Gilles. Liquid–liquid phase separation in aerosol particles: Imaging at the nanometer scale. *Environmental Science & Technology*, 49(8):4995–5002, 2015.

[66] Luca Costa, Giovanni Li-Destri, Neil H Thomson, Oleg Konovalov, and Diego Pontoni. Real space imaging of nanoparticle assembly at liquid–liquid interfaces with nanoscale resolution. *Nano Letters*, 16(9):5463–5468, 2016.

[67] Takeshi Fukuma, Bernhard Reischl, Naritaka Kobayashi, Peter Spijker, Filippo Federici Canova, Keisuke Miyazawa, and Adam S Foster. Mechanism of atomic force microscopy imaging of three-dimensional hydration structures at a solid-liquid interface. *Physical Review B*, 92(15):155412, 2015.

[68] Benjamin Pollard, Eric A Muller, Karsten Hinrichs, and Markus B Raschke. Vibrational nano-spectroscopic imaging correlating structure with intermolecular coupling and dynamics. *Nature Communications*, 5(1):1–7, 2014.

[69] Takashi Kimura, Yasumasa Joti, Akemi Shibuya, Changyong Song, Sangsoo Kim, Kensuke Tono, Makina Yabashi, Masatada Tamakoshi, Toshiyuki Moriya, Tairo Oshima, Tetsuya Ishikawa, Yoshitaka Bessho, and Yoshinori Nishino. Imaging live cell in micro-liquid enclosure by x-ray laser diffraction. *Nature Communications*, 5(1):1–7, 2014.

[70] Appala Raju Badireddy, Mark R Wiesner, and Jie Liu. Detection, characterization, and abundance of engineered nanoparticles in complex waters by hyperspectral imagery with enhanced darkfield microscopy. *Environmental Science & Technology*, 46(18):10081–10088, 2012.

[71] Moon S Kim, YR Chen, and PM Mehl. Hyperspectral reflectance and fluorescence imaging system for food quality and safety. *Transactions of the ASAE*, 44(3):721, 2001.

[72] Ana Perez Grassi, Anton J Tremmel, Alexander W Koch, and Hala J El-Khozondar. On-line thickness measurement for two-layer systems on polymer electronic devices. *Sensors*, 13(11):15747–15757, 2013.

[73] Alexander Weber-Bargioni, Adam Schwartzberg, Matteo Cornaglia, Ariel Ismach, Jeffrey J Urban, YuanJie Pang, Reuven Gordon, Jeffrey Bokor, Miquel B Salmeron, D Frank Ogletree, Paul Ahiby, Stefano Cabrini, and P James Schuck. Hyperspectral nanoscale imaging on dielectric substrates with coaxial optical antenna scan probes. *Nano Letters*, 11(3):1201–1207, 2011.

[74] Dan Fu, Gary Holtom, Christian Freudiger, Xu Zhang, and Xiaoliang Sunney Xie. Hyperspectral imaging with stimulated Raman scattering by chirped femtosecond lasers. *The Journal of Physical Chemistry B*, 117(16):4634–4640, 2013.

[75] S Piqueras, L Duponchel, R Tauler, and A De Juan. Monitoring polymorphic transformations by using in situ Raman hyperspectral imaging and image multiset analysis. *Analytica Chimica Acta*, 819:15–25, 2014.

[76] Marena Manley. Near-infrared spectroscopy and hyperspectral imaging: non-destructive analysis of biological materials. *Chemical Society Reviews*, 43(24):8200–8214, 2014.

[77] Yu John Hsu, Chih-Chiang Chen, Chien-Hsiang Huang, Chia-Hua Yeh, Li-Ying Liu, and Szu-Yu Chen. Line-scanning hyperspectral imaging based on structured illumination optical sectioning. *Biomedical Optics Express*, 8(6):3005–3016, 2017.

[78] Aoife A Gowen, Yaoze Feng, Edurne Gaston, and Vasilis Valdramidis. Recent applications of hyperspectral imaging in microbiology. *Talanta*, 137:43–54, 2015.

[79] Qi Pian, Ruoyang Yao, Nattawut Sinsuebphon, and Xavier Intes. Compressive hyperspectral time-resolved wide-field fluorescence lifetime imaging. *Nature Photonics*, 11(7):411, 2017.

[80] Hui Huang, Li Liu, and Michael O Ngadi. Recent developments in hyperspectral imaging for assessment of food quality and safety. *Sensors*, 14(4):7248–7276, 2014.

[81] Jacques Lefebvre. Real time hyperspectroscopy for dynamical study of carbon nanotubes. *ACS Nano*, 10(10):9602–9607, 2016.

[82] Liang Gao, Robert T Kester, Nathan Hagen, and Tomasz S Tkaczyk. Snapshot image mapping spectrometer (IMS) with high sampling density for hyperspectral microscopy. *Optics Express*, 18(14):14330–14344, 2010.

[83] Ludovic Duponchel, Waiss Elmi-Rayaleh, Cyril Ruckebusch, and Jean-Pierre Huvenne. Multivariate curve resolution methods in imaging spectroscopy: influence of extraction methods and instrumental perturbations. *Journal of Chemical Information and Computer Sciences*, 43(6):2057–2067, 2003.

[84] Massoud Ghasemzadeh-Barvarz, Adel Ramezani-Kakroodi, Denis Rodrigue, and Carl Duchesne. Multivariate image regression for quality control of natural fiber composites. *Industrial & Engineering Chemistry Research*, 52(35):12426–12436, 2013.

[85] Da-Wen Sun. *Hyperspectral imaging for food quality analysis and control*. Elsevier, 2010.

[86] Alexander FH Goetz, Gregg Vane, Jerry E Solomon, and Barrett N Rock. Imaging spectrometry for earth remote sensing. *Science*, 228(4704):1147–1153, 1985.

[87] Costanza Cucci, John K Delaney, and Marcello Picollo. Reflectance hyperspectral imaging for investigation of works of art: old master paintings and illuminated manuscripts. *Accounts of Chemical Research*, 49(10):2070–2079, 2016.

[88] Min Huang, Xiangmei Wan, Min Zhang, and Qibing Zhu. Detection of insect-damaged vegetable soybeans using hyperspectral transmittance image. *Journal of Food Engineering*, 116(1):45–49, 2013.

[89] Gabriel A Leiva-Valenzuela, Renfu Lu, and José Miguel Aguilera. Assessment of internal quality of blueberries using hyperspectral transmittance and reflectance images with whole spectra or selected wavelengths. *Innovative Food Science & Emerging Technologies*, 24:2–13, 2014.

[90] Jacques Lefebvre and Paul Finnie. Photoluminescence and forster resonance energy transfer in elemental bundles of single-walled carbon nanotubes. *The Journal of Physical Chemistry C*, 113(18):7536–7540, 2009.

[91] Jack A Alexander-Webber, Clement Faugeras, Piotr Kossacki, Marek Potemski, Xu Wang, Hee Dae Kim, Samuel D Stranks, Robert A Taylor, and Robin J Nicholas. Hyperspectral imaging of exciton photoluminescence in individual carbon nanotubes controlled by high magnetic fields. *Nano Letters*, 14(9):5194–5200, 2014.

[92] Steve Bégin, Bryan Burgoyne, Vincent Mercier, Alain Villeneuve, Réal Vallée, and Daniel Côté. Coherent anti-Stokes Raman scattering hyperspectral tissue imaging with a wavelength-swept system. *Biomedical Optics Express*, 2(5):1296–1306, 2011.

[93] Sebastian Karpf, Matthias Eibl, Wolfgang Wieser, Thomas Klein, and Robert Huber. A time-encoded technique for fibre-based hyperspectral broadband stimulated Raman microscopy. *Nature Communications*, 6(1):1–6, 2015.

[94] Brandon M Davis, Amanda J Hemphill, Derya Cebeci Maltaş, Michael A Zipper, Ping Wang, and Dor Ben-Amotz. Multivariate hyperspectral Raman imaging using compressive detection. *Analytical Chemistry*, 83(13):5086–5092, 2011.

[95] Eduardo M Perassi, Calin Hrelescu, Andreas Wisnet, Markus Döblinger, Christina Scheu, Frank Jäckel, Eduardo A Coronado, and Jochen Feldmann. Quantitative understanding of the optical properties of a single, complex-shaped gold nanoparticle from experiment and theory. *ACS Nano*, 8(5):4395–4402, 2014.

[96] Emilie Ringe, Bhavya Sharma, Anne-Isabelle Henry, Laurence D Marks, and Richard P Van Duyne. Single nanoparticle plasmonics. *Physical Chemistry Chemical Physics*, 15(12):4110–4129, 2013.

[97] Adam B Taylor and Peter Zijlstra. Single-molecule plasmon sensing: current status and future prospects. *ACS Sensors*, 2(8):1103–1122, 2017.

[98] Wei Wang and Nongjian Tao. Detection, counting, and imaging of single nanoparticles. *Analytical Chemistry*, 86(1):2–14, 2014.

[99] J-S Bouillard, S Vilain, W Dickson, and AV Zayats. Hyperspectral imaging with scanning near-field optical microscopy: applications in plasmonics. *Optics Express*, 18(16):16513–16519, 2010.

[100] Dominic Lepage, Alvaro Jiménez, Jacques Beauvais, and Jan J Dubowski. Conic hyperspectral dispersion mapping applied to semiconductor plasmonics. *Light: Science & Applications*, 1(9):e28–e28, 2012.

[101] Mónica B Mamián-López and Ronei J Poppi. SERS hyperspectral imaging assisted by MCR-ALS for studying polymeric microfilms loaded with paracetamol. *Microchemical Journal*, 123:243–251, 2015.

[102] Frank Neubrech, Christian Huck, Ksenia Weber, Annemarie Pucci, and Harald Giessen. Surface-enhanced infrared spectroscopy using resonant nanoantennas. *Chemical Reviews*, 117(7):5110–5145, 2017.

[103] Mohammad Rahman, Kenneth Davey, and Shi-Zhang Qiao. Advent of 2D rhenium disulfide (ReS_2): fundamentals to applications. *Advanced Functional Materials*, 27(10):1606129, 2017.

[104] Andres Castellanos-Gomez, Leonardo Vicarelli, Elsa Prada, Joshua O Island, KL Narasimha-Acharya, Sofya I Blanter, Dirk J Groenendijk, Michele Buscema, Gary A Steele, JV Alvarez, Herry W Zandbergen, JJ Palacios, and van der Zant Herre SJ. Isolation and characterization of few-layer black phosphorus. *2D Materials*, 1(2):025001, 2014.

[105] Jincan Zhang, Yucheng Huang, Zhenjun Tan, Tianran Li, Yichi Zhang, Kaicheng Jia, Li Lin, Luzhao Sun, Xiwen Chen, Zhenzhu Li, et al. Low-temperature heteroepitaxy of 2D PbI_2/graphene for large-area flexible photodetectors. *Advanced Materials*, 30(36):1803194, 2018.

[106] Kai Zhang, Lei Zhang, Fung Ling Yap, Peng Song, Cheng-Wei Qiu, and Kian Ping Loh. Large-area graphene nanodot array for plasmon-enhanced infrared spectroscopy. *Small*, 12(10):1302–1308, 2016.

[107] Luca La Notte, Giuseppe Valerio Bianco, Alessandro Lorenzo Palma, Aldo Di Carlo, Giovanni Bruno, and Andrea Reale. Sprayed organic photovoltaic cells and mini-modules based on chemical vapor deposited graphene as transparent conductive electrode. *Carbon*, 129:878–883, 2018.

[108] Hongtao Lin, Yi Song, Yizhong Huang, Derek Kita, Skylar Deckoff-Jones, Kaiqi Wang, Lan Li, Junying Li, Hanyu Zheng, Zhengqian Luo, et al. Chalcogenide glass-on-graphene photonics. *Nature Photonics*, 11(12):798–805, 2017.

[109] Yantao Chen, Ren Ren, Haihui Pu, Jingbo Chang, Shun Mao, and Junhong Chen. Field-effect transistor biosensors with two-dimensional black phosphorus nanosheets. *Biosensors and Bioelectronics*, 89:505–510, 2017.

[110] Xiaolong Chen, Xiaobo Lu, Bingchen Deng, Ofer Sinai, Yuchuan Shao, Cheng Li, Shaofan Yuan, Vy Tran, Kenji Watanabe, Takashi Taniguchi, et al. Widely tunable black phosphorus mid-infrared photodetector. *Nature Communications*, 8(1):1–7, 2017.

[111] Munkhbayar Batmunkh, Munkhjargal Bat-Erdene, and Joseph G Shapter. Black phosphorus: synthesis and application for solar cells. *Advanced Energy Materials*, 8(5):1701832, 2018.

[112] Huda S AlSalem, Chloe Holroyd, Melissa Danial Iswan, Andrew B Horn, Melissa A Denecke, and Sven PK Koehler. Characterisation, coverage, and orientation of functionalised graphene using sum-frequency generation spectroscopy. *Physical Chemistry Chemical Physics*, 20(13):8962–8967, 2018.

[113] Zhe Luo, Jesse Maassen, Yexin Deng, Yuchen Du, Richard P Garrelts, Mark S Lundstrom, D Ye Peide, and Xianfan Xu. Anisotropic in-plane thermal conductivity observed in few-layer black phosphorus. *Nature Communications*, 6(1):1–8, 2015.

[114] Juanxia Wu, Nannan Mao, Liming Xie, Hua Xu, and Jin Zhang. Identifying the crystalline orientation of black phosphorus using angle-resolved polarized Raman spectroscopy. *Angewandte Chemie International Edition*, 54(8):2366–2369, 2015.

[115] Charles Lin, Roberto Grassi, Tony Low, and Amr S Helmy. Multilayer black phosphorus as a versatile mid-infrared electro-optic material. *Nano Letters*, 16(3):1683–1689, 2016.

[116] Michele Buscema, Dirk J Groenendijk, Sofya I Blanter, Gary A Steele, Herre SJ Van Der Zant, and Andres Castellanos-Gomez. Fast and broadband photoresponse of few-layer black phosphorus field-effect transistors. *Nano Letters*, 14(6):3347–3352, 2014.

[117] Gongxun Bai, Shuoguo Yuan, Yuda Zhao, Zhibin Yang, Sin Yuk Choi, Yang Chai, Siu Fung Yu, Shu Ping Lau, and Jianhua Hao. 2D layered materials of rare-earth Er-doped MoS_2 with NIR-to-NIR down-and up-conversion photoluminescence. *Advanced Materials*, 28(34):7472–7477, 2016.

[118] Kehao Zhang, Simin Feng, Junjie Wang, Angelica Azcatl, Ning Lu, Rafik Addou, Nan Wang, Chanjing Zhou, Jordan Lerach, Vincent Bojan, et al. Manganese doping of monolayer MoS_2: the substrate is critical. *Nano Letters*, 15(10):6586–6591, 2015.

[119] Aleksander A Tedstone, David J Lewis, and Paul OBrien. Synthesis, properties, and applications of transition metal-doped layered transition metal dichalcogenides. *Chemistry of Materials*, 28(7):1965–1974, 2016.

[120] Antonio Di Bartolomeo, Filippo Giubileo, Giuseppe Luongo, Laura Iemmo, Nadia Martucciello, Gang Niu, Mirko Fraschke, Oliver Skibitzki, Thomas Schroeder, and Grzegorz Lupina. Tunable schottky barrier and high responsivity in graphene/Si-nanotip optoelectronic device. *2D Materials*, 4(1):015024, 2016.

[121] Jungwook Choi, Hanyu Zhang, and Jong Hyun Choi. Modulating optoelectronic properties of two-dimensional transition metal dichalcogenide semiconductors by photoinduced charge transfer. *ACS Nano*, 10(1):1671–1680, 2016.

[122] Jaekwang Lee, Jingsong Huang, Bobby G Sumpter, and Mina Yoon. Strain-engineered optoelectronic properties of 2D transition metal dichalcogenide lateral heterostructures. *2D Materials*, 4(2):021016, 2017.

[123] Feng Wang, Zhenxing Wang, Chao Jiang, Lei Yin, Ruiqing Cheng, Xueying Zhan, Kai Xu, Fengmei Wang, Yu Zhang, and Jun He. Progress on electronic and opto-

electronic devices of 2D layered semiconducting materials. *Small*, 13(35):1604298, 2017.

[124] Qiaoliang Bao and Kian Ping Loh. Graphene photonics, plasmonics, and broadband optoelectronic devices. *ACS Nano*, 6(5):3677–3694, 2012.

[125] Xia Congxin and Li Jingbo. Recent advances in optoelectronic properties and applications of two-dimensional metal chalcogenides. *Journal of Semiconductors*, 37(5):051001, 2016.

[126] Daria A Smirnova, Andrey E Miroshnichenko, Yuri S Kivshar, and Alexander B Khanikaev. Tunable nonlinear graphene metasurfaces. *Physical Review B*, 92(16):161406, 2015.

[127] Houlong L Zhuang and Richard G Hennig. Theoretical perspective of photocatalytic properties of single-layer SnS_2. *Physical Review B*, 88(11):115314, 2013.

[128] Yung-Chang Lin, Dumitru O Dumcenco, Hannu-Pekka Komsa, Yoshiko Niimi, Arkady V Krasheninnikov, Ying-Sheng Huang, and Kazu Suenaga. Properties of individual dopant atoms in single-layer MoS_2: atomic structure, migration, and enhanced reactivity. *Advanced Materials*, 26(18):2857–2861, 2014.

[129] Jingying Liu, Yunzhou Xue, Ziyu Wang, Zai-Quan Xu, Changxi Zheng, Bent Weber, Jingchao Song, Yusheng Wang, Yuerui Lu, Yupeng Zhang, et al. Two-dimensional $CH_3NH_3PbI_3$ perovskite: synthesis and optoelectronic application. *ACS Nano*, 10(3):3536–3542, 2016.

[130] Riccardo Frisenda, Yue Niu, Patricia Gant, Aday J Molina-Mendoza, Robert Schmidt, Rudolf Bratschitsch, Jinxin Liu, Lei Fu, Dumitru Dumcenco, Andras Kis, et al. Micro-reflectance and transmittance spectroscopy: a versatile and powerful tool to characterize 2D materials. *Journal of Physics D: Applied Physics*, 50(7):074002, 2017.

[131] Woong Choi, Mi Yeon Cho, Aniruddha Konar, Jong Hak Lee, Gi-Beom Cha, Soon Cheol Hong, Sangsig Kim, Jeongyong Kim, Debdeep Jena, Jinsoo Joo, et al. High-detectivity multilayer MoS_2 phototransistors with spectral response from ultraviolet to infrared. *Advanced Materials*, 24(43):5832–5836, 2012.

[132] MM Benameur, B Radisavljevic, JS Héron, S Sahoo, H Berger, and A Kis. Visibility of dichalcogenide nanolayers. *Nanotechnology*, 22(12):125706, 2011.

[133] Cory R Dean, Andrea F Young, Inanc Meric, Chris Lee, Lei Wang, Sebastian Sorgenfrei, Kenji Watanabe, Takashi Taniguchi, Phillip Kim, Kenneth L Shepard, et al. Boron nitride substrates for high-quality graphene electronics. *Nature Nanotechnology*, 5(10):722–726, 2010.

[134] Wei Yang, Guorui Chen, Zhiwen Shi, Cheng-Cheng Liu, Lianchang Zhang, Guibai Xie, Meng Cheng, Duoming Wang, Rong Yang, Dongxia Shi, et al. Epitaxial growth of single-domain graphene on hexagonal boron nitride. *Nature Materials*, 12(9):792–797, 2013.

[135] Behnood G Ghamsari, Jacob Tosado, Mahito Yamamoto, Michael S Fuhrer, and Steven M Anlage. Measuring the complex optical conductivity of graphene by Fabry-Pérot reflectance spectroscopy. *Scientific Reports*, 6:34166, 2016.

[136] F Borondics, Mathieu Jossent, C Sandt, Laure Lavoute, Dmitry Gaponov, Ammar Hideur, Paul Dumas, and Sébastien Février. Supercontinuum-based Fourier transform infrared spectromicroscopy. *Optica*, 5(4):378–381, 2018.

[137] Md Arafat Hossain, John Canning, Zhikang Yu, Sandra Ast, Peter J Rutledge, Joseph K-H Wong, Abbas Jamalipour, and Maxwell J Crossley. Time-resolved and temperature tuneable measurements of fluorescent intensity using a smartphone fluorimeter. *Analyst*, 142(11):1953–1961, 2017.

[138] Silas J Leavesley, Naga Annamdevula, John Boni, Samantha Stocker, Kristin Grant, Boris Troyanovsky, Thomas C Rich, and Diego F Alvarez. Hyperspectral imaging microscopy for identification and quantitative analysis of fluorescently-labeled cells in highly autofluorescent tissue. *Journal of Biophotonics*, 5(1):67–84, 2012.

[139] Lutz Langguth, Agata Szuba, Sander A Mann, Erik C Garnett, Gijsje H Koenderink, and A Femius Koenderink. Nano-antenna enhanced two-focus fluorescence correlation spectroscopy. *Scientific Reports*, 7(1):1–9, 2017.

[140] Patrik J Murr, Markus S Rauscher, Anton Tremmel, Michael Schardt, and Alexander W Koch. Fluorescence imaging of viscous materials in the ultraviolet-visible wavelength range. *Review of Scientific Instruments*, 85(8):085111, 2014.

[141] S Papernov, MD Brunsman, JB Oliver, BN Hoffman, AA Kozlov, SG Demos, A Shvydky, FHM Cavalcante, L Yang, CS Menoni, et al. Optical properties of oxygen vacancies in HfO_2 thin films studied by absorption and luminescence spectroscopy. *Optics Express*, 26(13):17608–17623, 2018.

[142] Matthias Eibl, Sebastian Karpf, Wolfgang Wieser, Thomas Klein, and Robert Huber. Hyperspectral stimulated Raman microscopy with two fiber laser sources. In *European Conference on Biomedical Optics*, page 953604. Optical Society of America, 2015.

[143] Andrea C Ferrari and Denis M Basko. Raman spectroscopy as a versatile tool for studying the properties of graphene. *Nature Nanotechnology*, 8(4):235–246, 2013.

[144] Thomas Hümmer, Jonathan Noe, Matthias S Hofmann, Theodor W Hänsch, Alexander Högele, and David Hunger. Cavity-enhanced Raman microscopy of individual carbon nanotubes. *Nature Communications*, 7(1):1–7, 2016.

[145] Ji-Xin Cheng and X Sunney Xie. Vibrational spectroscopic imaging of living systems: An emerging platform for biology and medicine. *Science*, 350(6264), 2015.

[146] Shihao Ran, Sebastian Berisha, Rupali Mankar, Wei-Chuan Shih, and David Mayerich. Mitigating fringing in discrete frequency infrared imaging using time-delayed integration. *Biomedical Optics Express*, 9(2):832–843, 2018.

[147] Shachi Mittal, Kevin Yeh, L Suzanne Leslie, Seth Kenkel, Andre Kajdacsy-Balla, and Rohit Bhargava. Simultaneous cancer and tumor microenvironment subtyping using confocal infrared microscopy for all-digital molecular histopathology. *Proceedings of the National Academy of Sciences*, 115(25):E5651–E5660, 2018.

[148] Kristen E Watts, Thomas J Blackburn, and Jeanne E Pemberton. Optical spectroscopy of surfaces, interfaces, and thin films: A status report. *Analytical Chemistry*, 91(7):4235–4265, 2019.

[149] Rohit Bhargava. Infrared spectroscopic imaging: the next generation. *Applied Spectroscopy*, 66(10):1091–1120, 2012.

[150] Andrea Centrone. Infrared imaging and spectroscopy beyond the diffraction limit. 2015.

[151] Florian Huth, Alexander Govyadinov, Sergiu Amarie, Wiwat Nuansing, Fritz Keilmann, and Rainer Hillenbrand. Nano-FTIR absorption spectroscopy of molecular fingerprints at 20 nm spatial resolution. *Nano letters*, 12(8):3973–3978, 2012.

[152] Kevin Yeh, Dongkwan Lee, and Rohit Bhargava. Multicolor discrete frequency infrared spectroscopic imaging. *Analytical Chemistry*, 91(3):2177–2185, 2019.

[153] Christian Rosenberg Petersen, Nikola Prtljaga, Mark Farries, Jon Ward, Bruce Napier, Gavin Rhys Lloyd, Jayakrupakar Nallala, Nick Stone, and Ole Bang. Mid-infrared multispectral tissue imaging using a chalcogenide fiber supercontinuum source. *Optics Letters*, 43(5):999–1002, 2018.

[154] Xiaohang Pan, Hao Xu, Yanqing Gao, Yafeng Zhang, Liaoxin Sun, Dan Li, Zhengji Wen, Shimin Li, Weiwei Yu, Zhiming Huang, et al. Spatial and frequency selective plasmonic metasurface for long wavelength infrared spectral region. *Advanced Optical Materials*, 6(20):1800337, 2018.

[155] Panagis D Samolis and Michelle Y Sander. Phase-sensitive lock-in detection for high-contrast mid-infrared photothermal imaging with sub-diffraction limited resolution. *Optics Express*, 27(3):2643–2655, 2019.

[156] Weiliang Ma, Pablo Alonso-González, Shaojuan Li, Alexey Y Nikitin, Jian Yuan, Javier Martín-Sánchez, Javier Taboada-Gutiérrez, Iban Amenabar, Peining Li, Saül Vélez, et al. In-plane anisotropic and ultra-low-loss polaritons in a natural van der Waals crystal. *Nature*, 562(7728):557–562, 2018.

[157] Alexandre Dazzi and Craig B Prater. AFM-IR: Technology and applications in nanoscale infrared spectroscopy and chemical imaging. *Chemical Reviews*, 117(7):5146–5173, 2017.

[158] Zhiwen Shi, Hans A Bechtel, Samuel Berweger, Yinghui Sun, Bo Zeng, Chenhao Jin, Henry Chang, Michael C Martin, Markus B Raschke, and Feng Wang. Amplitude-and phase-resolved nanospectral imaging of phonon polaritons in hexagonal boron nitride. *ACS Photonics*, 2(7):790–796, 2015.

[159] FJ Alfaro-Mozaz, Pablo Alonso-González, Saul Vélez, I Dolado, M Autore, S Mastel, F Casanova, LE Hueso, P Li, A Yu Nikitin, et al. Nanoimaging of resonating hyperbolic polaritons in linear boron nitride antennas. *Nature Communications*, 8(1):1–8, 2017.

[160] Piotr Patoka, Georg Ulrich, Ariana E Nguyen, Ludwig Bartels, Peter A Dowben, Volodymyr Turkowski, Talat S Rahman, Peter Hermann, Bernd Kästner, Arne Hoehl, et al. Nanoscale plasmonic phenomena in CVD-grown MoS_2 monolayer revealed by ultra-broadband synchrotron radiation based nano-FTIR spectroscopy and near-field microscopy. *Optics Express*, 24(2):1154–1164, 2016.

[161] Eric A Muller, Benjamin Pollard, and Markus B Raschke. Infrared chemical nanoimaging: Accessing structure, coupling, and dynamics on molecular length scales. *The Journal of Physical Chemistry Letters*, 6(7):1275–1284, 2015.

[162] P Uhd Jepsen, David G Cooke, and Martin Koch. Terahertz spectroscopy and imaging-modern techniques and applications. *Laser & Photonics Reviews*, 5(1):124–166, 2011.

[163] Roger A Lewis. A review of terahertz sources. *Journal of Physics D: Applied Physics*, 47(37):374001, 2014.

[164] Hannah J Joyce, Jessica L Boland, Christopher L Davies, Sarwat A Baig, and Michael B Johnston. A review of the electrical properties of semiconductor nanowires: insights gained from terahertz conductivity spectroscopy. *Semiconductor Science and Technology*, 31(10):103003, 2016.

[165] Jannika Lauth, Sachin Kinge, and Laurens DA Siebbeles. Ultrafast transient absorption and terahertz spectroscopy as tools to probe photoexcited states and dynamics in colloidal 2D nanostructures. *Zeitschrift für Physikalische Chemie*, 231(1):107–119, 2017.

[166] Jannika Lauth, Aditya Kulkarni, Frank CM Spoor, Nicolas Renaud, Ferdinand C Grozema, Arjan J Houtepen, Juleon M Schins, Sachin Kinge, and Laurens DA Siebbeles. Photogeneration and mobility of charge carriers in atomically thin colloidal inse nanosheets probed by ultrafast terahertz spectroscopy. *The Journal of Physical Chemistry Letters*, 7(20):4191–4196, 2016.

[167] Rebecca L Milot, Rebecca J Sutton, Giles E Eperon, Amir Abbas Haghighirad, Josue Martinez Hardigree, Laura Miranda, Henry J Snaith, Michael B Johnston, and Laura M Herz. Charge-carrier dynamics in 2D hybrid metal-halide perovskites. *Nano Letters*, 16(11):7001–7007, 2016.

[168] Guangjiang Li, Kateryna Kushnir, Mengjing Wang, Yongchang Dong, Sergii Chertopalov, Apparao M Rao, Vadym N Mochalin, Ramakrishna Podila, Kristie Koski, and Lyubov V Titova. Terahertz spectroscopy of 2D materials. In *2018 43rd International Conference on Infrared, Millimeter, and Terahertz Waves (IRMMW-THz)*, pages 1–3. IEEE, 2018.

[169] Steven A Henck, Walter M Duncan, Lee M Lowenstein, and Stephanie Watts Butler. In situ spectral ellipsometry for real-time thickness measurement: Etching multilayer stacks. *Journal of Vacuum Science & Technology A: Vacuum, Surfaces, and Films*, 11(4):1179–1185, 1993.

[170] Peter Westphal and Antje Bornmann. Biomolecular detection by surface plasmon enhanced ellipsometry. *Sensors and Actuators B: Chemical*, 84(2-3):278–282, 2002.

[171] RA Synowicki, Craig M Herzinger, James T Hall, and Andrew Malingowski. Optical constants of electroplated gold from spectroscopic ellipsometry. *Applied Surface Science*, 421:824–830, 2017.

[172] Aleksandar Matković, Uroš Ralević, Manisha Chhikara, Milka M Jakovljević, Djordje Jovanović, Gvido Bratina, and Radoš Gajić. Influence of transfer residue on the optical properties of chemical vapor deposited graphene investigated through spectroscopic ellipsometry. *Journal of Applied Physics*, 114(9):093505, 2013.

[173] S Funke, B Miller, E Parzinger, P Thiesen, AW Holleitner, and U Wurstbauer. Imaging spectroscopic ellipsometry of MoS_2. *Journal of Physics: Condensed Matter*, 28(38):385301, 2016.

[174] You-Chia Chang, Chang-Hua Liu, Che-Hung Liu, Zhaohui Zhong, and Theodore B Norris. Extracting the complex optical conductivity of mono-and bilayer graphene by ellipsometry. *Applied Physics Letters*, 104(26):261909, 2014.

[175] R Secondo, D Fomra, N Izyumskaya, V Avrutin, JN Hilfiker, A Martin, Ü Özgür, and NJOME Kinsey. Reliable modeling of ultrathin alternative plasmonic materials using spectroscopic ellipsometry. *Optical Materials Express*, 9(2):760–770, 2019.

[176] Matteo Bruna and SJAPL Borini. Optical constants of graphene layers in the visible range. *Applied Physics Letters*, 94(3):031901, 2009.

[177] Jahan M Dawlaty, Shriram Shivaraman, Jared Strait, Paul George, Mvs Chandrashekhar, Farhan Rana, Michael G Spencer, Dmitry Veksler, and Yunqing Chen. Measurement of the optical absorption spectra of epitaxial graphene from terahertz to visible. *Applied Physics Letters*, 93(13):131905, 2008.

[178] Cristiane N Santos, Frédéric Joucken, Domingos De Sousa Meneses, Patrick Echegut, Jessica Campos-Delgado, Pierre Louette, Jean-Pierre Raskin, and Benoit Hackens. Terahertz and mid-infrared reflectance of epitaxial graphene. *Scientific Reports*, 6:24301, 2016.

[179] Takuya Iwasaki, Taharh Zelai, Sheng Ye, Yoshishige Tsuchiya, Harold MH Chong, and Hiroshi Mizuta. Local hole doping concentration modulation on graphene probed by tip-enhanced Raman spectroscopy. *Carbon*, 111:67–73, 2017.

[180] Robin W Havener, Houlong Zhuang, Lola Brown, Richard G Hennig, and Jiwoong Park. Angle-resolved Raman imaging of interlayer rotations and interactions in twisted bilayer graphene. *Nano Letters*, 12(6):3162–3167, 2012.

[181] Jianing Chen, Michela Badioli, Pablo Alonso-González, Sukosin Thongrattanasiri, Florian Huth, Johann Osmond, Marko Spasenović, Alba Centeno, Amaia Pesquera, Philippe Godignon, et al. Optical nano-imaging of gate-tunable graphene plasmons. *Nature*, 487(7405):77–81, 2012.

[182] S Dai, Q Ma, MK Liu, T Andersen, Z Fei, MD Goldflam, M Wagner, K Watanabe, T Taniguchi, M Thiemens, et al. Graphene on hexagonal boron nitride as a tunable hyperbolic metamaterial. *Nature Nanotechnology*, 10(8):682–686, 2015.

[183] Xiaoxia Yang, Feng Zhai, Hai Hu, Debo Hu, Ruina Liu, Shunping Zhang, Mengtao Sun, Zhipei Sun, Jianing Chen, and Qing Dai. Far-field spectroscopy and near-field optical imaging of coupled plasmon–phonon polaritons in 2D van der waals heterostructures. *Advanced Materials*, 28(15):2931–2938, 2016.

[184] Ji-Hun Kang, Sheng Wang, Zhiwen Shi, Wenyu Zhao, Eli Yablonovitch, and Feng Wang. Goos-hänchen shift and even–odd peak oscillations in edge-reflections of surface polaritons in atomically thin crystals. *Nano Letters*, 17(3):1768–1774, 2017.

[185] Ingrid D Barcelos, Alisson R Cadore, Leonardo C Campos, Angelo Malachias, K Watanabe, T Taniguchi, Francisco CB Maia, Raul Freitas, and Christoph Deneke. Graphene/H-BN plasmon-phonon coupling and plasmon delocalization observed by infrared nano-spectroscopy. *Nanoscale*, 7(27):11620–11625, 2015.

[186] Gregory Auton, Dmytro B But, Jiawei Zhang, Ernie Hill, Dominique Coquillat, Christophe Consejo, Philippe Nouvel, Wojciech Knap, Luca Varani, Frederic Teppe, et al. Terahertz detection and imaging using graphene ballistic rectifiers. *Nano Letters*, 17(11):7015–7020, 2017.

[187] JL Tomaino, AD Jameson, JW Kevek, MJ Paul, AM Van Der Zande, RA Barton, PL McEuen, ED Minot, and Yun-Shik Lee. Terahertz imaging and spectroscopy of large-area single-layer graphene. *Optics Express*, 19(1):141–146, 2011.

[188] Ivan Ivanov, Mischa Bonn, Zoltán Mics, and Dmitry Turchinovich. Perspective on terahertz spectroscopy of graphene. *EPL (Europhysics Letters)*, 111(6):67001, 2015.

[189] Lei Ren, Qi Zhang, Jun Yao, Zhengzong Sun, Ryosuke Kaneko, Zheng Yan, Sebastien Nanot, Zhong Jin, Iwao Kawayama, Masayoshi Tonouchi, et al. Terahertz and infrared spectroscopy of gated large-area graphene. *Nano Letters*, 12(7):3711–3715, 2012.

[190] Patrick R Whelan, Deping Huang, David Mackenzie, Sara A Messina, Zhancheng Li, Xin Li, Yunqing Li, Timothy J Booth, Peter U Jepsen, Haofei Shi, et al. Conductivity mapping of graphene on polymeric films by terahertz time-domain spectroscopy. *Optics Express*, 26(14):17748–17754, 2018.

[191] JW Weber, VE Calado, and MCM Van De Sanden. Optical constants of graphene measured by spectroscopic ellipsometry. *Applied Physics Letters*, 97(9):091904, 2010.

[192] FJ Nelson, VK Kamineni, T Zhang, ES Comfort, JU Lee, and AC Diebold. Optical properties of large-area polycrystalline chemical vapor deposited graphene by spectroscopic ellipsometry. *Applied Physics Letters*, 97(25):253110, 2010.

[193] Aleksandar Matković, Angela Beltaos, Marijana Milićević, Uroš Ralević, Borislav Vasić, Djordje Jovanović, and Radoš Gajić. Spectroscopic imaging ellipsometry and fano resonance modeling of graphene. *Journal of Applied Physics*, 112(12):123523, 2012.

[194] Wei Li, Guangjun Cheng, Yiran Liang, Boyuan Tian, Xuelei Liang, Lianmao Peng, AR Hight Walker, David J Gundlach, and Nhan V Nguyen. Broadband optical properties of graphene by spectroscopic ellipsometry. *Carbon*, 99:348–353, 2016.

[195] Andres Castellanos-Gomez, Jorge Quereda, Herko P van der Meulen, Nicolás Agraït, and Gabino Rubio-Bollinger. Spatially resolved optical absorption spectroscopy of single- and few-layer MoS_2 by hyperspectral imaging. *Nanotechnology*, 27(11):115705, 2016.

[196] G Plechinger, F Mooshammer, A Castellanos-Gomez, GA Steele, C Schüller, and T Korn. Optical spectroscopy of interlayer coupling in artificially stacked MoS_2 layers. *2D Materials*, 2(3):034016, 2015.

[197] Xiaoli Li, Yafang Shi, Shuai Li, Wei Shi, Wenpeng Han, Chuan Zhou, Xiaohui Zhao, and Baolai Liang. Layer-number dependent reflection spectra of MoS_2 flakes on SiO_2/Si substrate. *Optical Materials Express*, 8(10):3082–3091, 2018.

[198] Yue Niu, Sergio Gonzalez-Abad, Riccardo Frisenda, Philipp Marauhn, Matthias Drüppel, Patricia Gant, Robert Schmidt, Najme S Taghavi, David Barcons, Aday J Molina-Mendoza, et al. Thickness-dependent differential reflectance spectra of monolayer and few-layer MoS_2, $MoSe_2$, WS_2 and WSe_2. *Nanomaterials*, 8(9):725, 2018.

[199] Haiyan Nan, Zilu Wang, Wenhui Wang, Zheng Liang, Yan Lu, Qian Chen, Daowei He, Pingheng Tan, Feng Miao, Xinran Wang, et al. Strong photoluminescence enhancement of MoS_2 through defect engineering and oxygen bonding. *ACS Nano*, 8(6):5738–5745, 2014.

[200] Weitao Su, Naresh Kumar, Sandro Mignuzzi, Jason Crain, and Debdulal Roy. Nanoscale mapping of excitonic processes in single-layer MoS_2 using tip-enhanced photoluminescence microscopy. *Nanoscale*, 8(20):10564–10569, 2016.

[201] Kyoung-Duck Park, Omar Khatib, Vasily Kravtsov, Genevieve Clark, Xiaodong Xu, and Markus B Raschke. Hybrid tip-enhanced nanospectroscopy and nanoimaging of monolayer WSe_2 with local strain control. *Nano Letters*, 16(4):2621–2627, 2016.

[202] Benjamin J Robinson, Cristina E Giusca, Yurema Teijeiro Gonzalez, Nicholas D Kay, Olga Kazakova, and Oleg V Kolosov. Structural, optical and electrostatic properties of single and few-layers MoS_2: effect of substrate. *2D Materials*, 2(1):015005, 2015.

[203] Yingchao Zhang, Dmitri V Voronine, Shangran Qiu, Alexander M Sinyukov, Mary Hamilton, Zachary Liege, Alexei V Sokolov, Zhenrong Zhang, and Marlan O Scully. Improving resolution in quantum subnanometre-gap tip-enhanced Raman nanoimaging. *Scientific Reports*, 6(1):1–9, 2016.

[204] Guillaume Froehlicher, Etienne Lorchat, Olivia Zill, Michelangelo Romeo, and Stéphane Berciaud. Rigid-layer Raman-active modes in N-layer transition metal dichalcogenides: interlayer force constants and hyperspectral Raman imaging. *Journal of Raman Spectroscopy*, 49(1):91–99, 2018.

[205] Debo Hu, Xiaoxia Yang, Chi Li, Ruina Liu, Ziheng Yao, Hai Hu, Stephanie N Gilbert Corder, Jianing Chen, Zhipei Sun, Mengkun Liu, et al. Probing optical anisotropy of nanometer-thin Van der Waals microcrystals by near-field imaging. *Nature Communications*, 8(1):1–8, 2017.

[206] SB Lu, LL Miao, ZN Guo, X Qi, CJ Zhao, H Zhang, SC Wen, DY Tang, and DY Fan. Broadband nonlinear optical response in multi-layer black phosphorus: an emerging infrared and mid-infrared optical material. *Optics Express*, 23(9):11183–11194, 2015.

[207] Xi Ling, Shengxi Huang, Eddwi H Hasdeo, Liangbo Liang, William M Parkin, Yuki Tatsumi, Ahmad RT Nugraha, Alexander A Puretzky, Paul Masih Das, Bobby G

Sumpter, et al. Anisotropic electron-photon and electron-phonon interactions in black phosphorus. *Nano Letters*, 16(4):2260–2267, 2016.

[208] Arnob Islam, Wei Du, Vida Pashaei, Hao Jia, Zenghui Wang, Jaesung Lee, Guo Jun Ye, Xian Hui Chen, and Philip X-L Feng. Discerning black phosphorus crystal orientation and anisotropy by polarized reflectance measurement. *ACS Applied Materials & Interfaces*, 10(30):25629–25637, 2018.

[209] Xiaomu Wang, Aaron M Jones, Kyle L Seyler, Vy Tran, Yichen Jia, Huan Zhao, Han Wang, Li Yang, Xiaodong Xu, and Fengnian Xia. Highly anisotropic and robust excitons in monolayer black phosphorus. *Nature Nanotechnology*, 10(6):517–521, 2015.

[210] Chen Chen, Feng Chen, Xiaolong Chen, Bingchen Deng, Brendan Eng, Daehwan Jung, Qiushi Guo, Shaofan Yuan, Kenji Watanabe, Takashi Taniguchi, et al. Bright mid-infrared photoluminescence from thin-film black phosphorus. *Nano Letters*, 19(3):1488–1493, 2019.

[211] Fengnian Xia, Han Wang, and Yichen Jia. Rediscovering black phosphorus as an anisotropic layered material for optoelectronics and electronics. *Nature Communications*, 5(1):1–6, 2014.

[212] Sampath Gamage, Zhen Li, Vladislav S Yakovlev, Colin Lewis, Han Wang, Stephen B Cronin, and Yohannes Abate. Nanoscopy of black phosphorus degradation. *Advanced Materials Interfaces*, 3(12):1600121, 2016.

[213] D Grasseschi, DA Bahamon, FCB Maia, AH Castro Neto, RO Freitas, and CJS De Matos. Oxygen impact on the electronic and vibrational properties of black phosphorus probed by synchrotron infrared nanospectroscopy. *2D Materials*, 4(3):035028, 2017.

[214] Ye Ming Qing, Hui Feng Ma, and Tie Jun Cui. Tailoring anisotropic perfect absorption in monolayer black phosphorus by critical coupling at terahertz frequencies. *Optics Express*, 26(25):32442–32450, 2018.

[215] Xi Wang, Qian Ma, Leiming Wu, Jun Guo, Shunbin Lu, Xiaoyu Dai, and Yuanjiang Xiang. Tunable terahertz/infrared coherent perfect absorption in a monolayer black phosphorus. *Optics Express*, 26(5):5488–5496, 2018.

[216] HB Ribeiro, CEP Villegas, DA Bahamon, D Muraca, AH Castro Neto, EAT De Souza, AR Rocha, MA Pimenta, and CJS De Matos. Edge phonons in black phosphorus. *Nature Communications*, 7(1):1–7, 2016.

[217] Henrique B Ribeiro, Marcos A Pimenta, and Christiano JS de Matos. Raman spectroscopy in black phosphorus. *Journal of Raman Spectroscopy*, 49(1):76–90, 2018.

[218] Fadhel Alsaffar, Sarah Alodan, Abdul Alrasheed, Abdulrahman Alhussain, Noura Alrubaiq, Ahmad Abbas, and Moh R Amer. Raman sensitive degradation and etching dynamics of exfoliated black phosphorus. *Scientific Reports*, 7:44540, 2017.

[219] Sruthi Kuriakose, Taimur Ahmed, Patrick Taylor, Yi Zhu, Michelle JS Spencer, Sivacarendran Balendhran, Yuerui Lu, Vipul Bansal, Sharath Sriram, Madhu Bhaskaran, et al. Generating strong room-temperature photoluminescence in black phosphorus using organic molecules. *2D Materials*, 6(1):015009, 2018.

[220] Stefan Heist, Chen Zhang, Karl Reichwald, Peter Kühmstedt, Gunther Notni, and Andreas Tünnermann. 5D hyperspectral imaging: fast and accurate measurement of surface shape and spectral characteristics using structured light. *Optics Express*, 26(18):23366–23379, 2018.

[221] Claudia V Correa, Henry Arguello, and Gonzalo R Arce. Snapshot colored compressive spectral imager. *JOSA A*, 32(10):1754–1763, 2015.

[222] Anton Hasenkampf, Niels Kröger, Arthur Schönhals, Wolfgang Petrich, and Annemarie Pucci. Surface-enhanced mid-infrared spectroscopy using a quantum cascade laser. *Optics Express*, 23(5):5670–5680, 2015.

[223] Artem Yakovliev, Roman Ziniuk, Junle Qu, and Tymish Y Ohulchanskyy. Hyperspectral imaging of rare-earth doped nanoparticles emitting in near-and short-wave infrared regions. In *Tenth International Conference on Information Optics and Photonics*, volume 10964, page 109646J. International Society for Optics and Photonics, 2018.

[224] Nicolas Dobigeon and Nathalie Brun. Spectral mixture analysis of EELS spectrum-images. *Ultramicroscopy*, 120:25–34, 2012.

[225] Pavel Potapov and Axel Lubk. Optimal principal component analysis of STEM XEDS spectrum images. *Advanced Structural and Chemical Imaging*, 5(1):4, 2019.

[226] José MP Nascimento and José MB Dias. Vertex component analysis: A fast algorithm to unmix hyperspectral data. *IEEE transactions on Geoscience and Remote Sensing*, 43(4):898–910, 2005.

[227] Judith Felten, Hardy Hall, Joaquim Jaumot, Romà Tauler, Anna De Juan, and András Gorzsás. Vibrational spectroscopic image analysis of biological material using multivariate curve resolution–alternating least squares (MCR-ALS). *Nature Protocols*, 10(2):217–240, 2015.

[228] S Piqueras, L Duponchel, R Tauler, and A De Juan. Resolution and segmentation of hyperspectral biomedical images by multivariate curve resolution-alternating least squares. *Analytica Chimica Acta*, 705(1-2):182–192, 2011.

[229] Anna De Juan, Joaquim Jaumot, and Romà Tauler. Multivariate curve resolution (MCR). Solving the mixture analysis problem. *Analytical Methods*, 6(14):4964–4976, 2014.

[230] Clemence Fauteux-Lefebvre, Francis Lavoie, and Ryan Gosselin. A hierarchical multivariate curve resolution methodology to identify and map compounds in spectral images. *Analytical Chemistry*, 90(21):13118–13125, 2018.

[231] Yuval Garini, Ian T Young, and George McNamara. Spectral imaging: principles and applications. *Cytometry Part A: The Journal of the International Society for Analytical Cytology*, 69(8):735–747, 2006.

[232] Xiaoli Li, Ruiqing Zhou, Yifei Xu, Xuan Wei, and Yong He. Spectral unmixing combined with Raman imaging, a preferable analytic technique for molecule visualization. *Applied Spectroscopy Reviews*, 52(5):417–438, 2017.

[233] Emilie Chouzenoux, Maxime Legendre, Saïd Moussaoui, and Jérôme Idier. Fast constrained least squares spectral unmixing using primal-dual interior-point optimization. *IEEE Journal of Selected Topics in Applied Earth Observations and Remote Sensing*, 7(1):59–69, 2013.

[234] Xingchen Dong, Jie Dong, Ali K Yetisen, Michael H Köhler, Shengjia Wang, Martin Jakobi, and Alexander W Koch. Characterization and layer thickness mapping of two-dimensional MoS_2 flakes via hyperspectral line-scanning microscopy. *Applied Physics Express*, 12(10):102004, 2019.

[235] Ramakrishnan Kannan, AV Ievlev, Nouamane Laanait, Maxim A Ziatdinov, Rama K Vasudevan, Stephen Jesse, and Sergei V Kalinin. Deep data analysis via physically constrained linear unmixing: universal framework, domain examples, and a community-wide platform. *Advanced Structural and Chemical Imaging*, 4(1):6, 2018.

[236] Chien-Sheng Liao, Joon Hee Choi, Delong Zhang, Stanley H Chan, and Ji-Xin Cheng. Denoising stimulated Raman spectroscopic images by total variation minimization. *The Journal of Physical Chemistry C*, 119(33):19397–19403, 2015.

[237] A Hutzler, CD Matthus, M Rommel, and L Frey. Generalized approach to design multi-layer stacks for enhanced optical detectability of ultrathin layers. *Applied Physics Letters*, 110(2):021909, 2017.

[238] Chunwei Hsu, Riccardo Frisenda, Robert Schmidt, Ashish Arora, Steffen Michaelis De Vasconcellos, Rudolf Bratschitsch, Herre SJ van der Zant, and Andres Castellanos-Gomez. Thickness-dependent refractive index of 1L, 2L, and 3L MoS_2, MoS_2, WS_2, and WSe_2. *Advanced Optical Materials*, 7(13):1900239, 2019.

[239] CE Stevens, Tineke Stroucken, AV Stier, J Paul, H Zhang, P Dey, SA Crooker, Stephan W Koch, and Denis Karaiskaj. Superradiant coupling effects in transition-metal dichalcogenides. *Optica*, 5(6):749–755, 2018.

[240] Majharul Haque Khan, Hua Kun Liu, Xudong Sun, Yusuke Yamauchi, Yoshio Bando, Dmitri Golberg, and Zhenguo Huang. Few-atomic-layered hexagonal boron nitride: CVD growth, characterization, and applications. *Materials Today*, 20(10):611–628, 2017.

[241] Chu Liu, Yaoguang Ma, Weisen Li, and Lun Dai. The evolution of Raman spectrum of graphene with the thickness of SiO_2 capping layer on Si substrate. *Applied Physics Letters*, 103(21):213103, 2013.

[242] Hui Zhang, Yaoguang Ma, Yi Wan, Xin Rong, Ziang Xie, Wei Wang, and Lun Dai. Measuring the refractive index of highly crystalline monolayer MoS_2 with high confidence. *Scientific Reports*, 5:8440, 2015.

[243] Kei Kinoshita, Rai Moriya, Momoko Onodera, Yusai Wakafuji, Satoru Masubuchi, Kenji Watanabe, Takashi Taniguchi, and Tomoki Machida. Dry release transfer of graphene and few-layer h-BN by utilizing thermoplasticity of polypropylene carbonate. *npj 2D Materials and Applications*, 3(1):1–8, 2019.

[244] Yeonghoon Jin, Yoonhyuk Rah, Junghoon Park, Jaeho Shim, and Kyoungsik Yu. Rapid and broad-range thickness estimation method of hexagonal boron nitride using Raman spectroscopy and optical microscope. *Applied Physics Letters*, 116(8):081104, 2020.

[245] Nihit Saigal, Amlan Mukherjee, Vasam Sugunakar, and Sandip Ghosh. Angle of incidence averaging in reflectance measurements with optical microscopes for

studying layered two-dimensional materials. *Review of Scientific Instruments*, 85(7):073105, 2014.

[246] Joel M Katzen, Matej Velicky, Yuefeng Huang, Stacey Drakeley, William Hendren, Robert M Bowman, Qiran Cai, Ying Chen, Lu Hua Li, and Fumin Huang. Rigorous and accurate contrast spectroscopy for ultimate thickness determination of micrometer-sized graphene on gold and molecular sensing. *ACS Applied Materials & Interfaces*, 10(26):22520–22528, 2018.

[247] Yuanlong Zhang, Lingjie Kong, Hao Xie, Xiaofei Han, and Qionghai Dai. Enhancing axial resolution and background rejection in line-scanning temporal focusing microscopy by focal modulation. *Optics Express*, 26(17):21518–21526, 2018.

[248] Peter J Verveer, Jim Swoger, Francesco Pampaloni, Klaus Greger, Marco Marcello, and Ernst HK Stelzer. High-resolution three-dimensional imaging of large specimens with light sheet-based microscopy. *Nature Methods*, 4(4):311–313, 2007.

[249] Kevin M Dean, Philippe Roudot, Erik S Welf, Gaudenz Danuser, and Reto Fiolka. Deconvolution-free subcellular imaging with axially swept light sheet microscopy. *Biophysical Journal*, 108(12):2807–2815, 2015.

[250] Yilei Li, Alexey Chernikov, Xian Zhang, Albert Rigosi, Heather M Hill, Arend M Van Der Zande, Daniel A Chenet, En-Min Shih, James Hone, and Tony F Heinz. Measurement of the optical dielectric function of monolayer transition-metal dichalcogenides: MoS_2, $MoSe_2$, WS_2, and WSe_2. *Physical Review B*, 90(20):205422, 2014.

[251] Yilei Li and Tony F Heinz. Two-dimensional models for the optical response of thin films. *2D Materials*, 5(2):025021, 2018.

[252] Xiao-Li Li, Wen-Peng Han, Jiang-Bin Wu, Xiao-Fen Qiao, Jun Zhang, and Ping-Heng Tan. Layer-number dependent optical properties of 2D materials and their application for thickness determination. *Advanced Functional Materials*, 27(19):1604468, 2017.

[253] Yongjin Zhou, Weijian Huang, Pei Dong, Yong Xia, and Shanshan Wang. D-UNet: a dimension-fusion U shape network for chronic stroke lesion segmentation. *IEEE/ACM Transactions on Computational Biology and Bioinformatics*, 2019.

[254] Yu Liu, Xun Chen, Zengfu Wang, Z Jane Wang, Rabab K Ward, and Xuesong Wang. Deep learning for pixel-level image fusion: Recent advances and future prospects. *Information Fusion*, 42:158–173, 2018.

[255] Pedram Ghamisi, Bernhard Höfle, and Xiao Xiang Zhu. Hyperspectral and LiDAR data fusion using extinction profiles and deep convolutional neural network. *IEEE Journal of Selected Topics in Applied Earth Observations and Remote Sensing*, 10(6):3011–3024, 2016.

[256] Frosti Palsson, Johannes R Sveinsson, and Magnus O Ulfarsson. Multispectral and hyperspectral image fusion using a 3-D-convolutional neural network. *IEEE Geoscience and Remote Sensing Letters*, 14(5):639–643, 2017.

[257] Zhe Guo, Xiang Li, Heng Huang, Ning Guo, and Quanzheng Li. Deep learning-based image segmentation on multimodal medical imaging. *IEEE Transactions on Radiation and Plasma Medical Sciences*, 3(2):162–169, 2019.

[258] Xiaomeng Li, Hao Chen, Xiaojuan Qi, Qi Dou, Chi-Wing Fu, and Pheng-Ann Heng. H-DenseUNet: hybrid densely connected UNet for liver and tumor segmentation from CT volumes. *IEEE Transactions on Medical Imaging*, 37(12):2663–2674, 2018.

[259] Olaf Ronneberger, Philipp Fischer, and Thomas Brox. U-net: Convolutional networks for biomedical image segmentation. In *International Conference on Medical Image Computing and Computer-assisted Intervention*, pages 234–241. Springer, 2015.

[260] Andres Castellanos-Gomez, Michele Buscema, Rianda Molenaar, Vibhor Singh, Laurens Janssen, Herre SJ Van Der Zant, and Gary A Steele. Deterministic transfer of two-dimensional materials by all-dry viscoelastic stamping. *2D Materials*, 1(1):011002, 2014.

[261] Guorui Wang, Zhaohe Dai, Yanlei Wang, PingHeng Tan, Luqi Liu, Zhiping Xu, Yueguang Wei, Rui Huang, and Zhong Zhang. Measuring interlayer shear stress in bilayer graphene. *Physical Review Letters*, 119(3):036101, 2017.

[262] Thomas P Darlington, Christian Carmesin, Matthias Florian, Emanuil Yanev, Obafunso Ajayi, Jenny Ardelean, Daniel A Rhodes, Augusto Ghiotto, Andrey Krayev, Kenji Watanabe, et al. Imaging strain-localized excitons in nanoscale bubbles of monolayer WSe_2 at room temperature. *Nature Nanotechnology*, pages 1–7, 2020.

[263] Artur Branny, Santosh Kumar, Raphaël Proux, and Brian D Gerardot. Deterministic strain-induced arrays of quantum emitters in a two-dimensional semiconductor. *Nature Communications*, 8(1):1–7, 2017.

[264] Zhaohe Dai, Luqi Liu, and Zhong Zhang. Strain engineering of 2D materials: issues and opportunities at the interface. *Advanced Materials*, 31(45):1805417, 2019.

Patents and Publications

[1] **Xingchen Dong**,# Hongwei Li,# Zhutong Jiang,# Theresa Gruünleitner, Inci Güler, Jie Dong, Kun Wang, Michael H Köhler, Martin Jakobi, Bjoern Menze, Ali K Yetisen, Ian D Sharp, Andreas V Stier, Jonathan J Finley, and Alexander W Koch. 3D deep learning enables accurate layer mapping of 2D materials. *ACS Nano*, 15(2):3139–3151, 2021. #Equal contribution.

[2] **Xingchen Dong**, Ali K Yetisen, Heng Tian, Inci Güler, Andreas V Stier, Zhendong Li, Michael H Köhler, Jie Dong, Martin Jakobi, Jonathan J Finley, and Alexander W Koch. Line-scan hyperspectral imaging microscopy with linear unmixing for automated two-dimensional crystals identification. *ACS Photonics*, 7(5):1216–1225, 2020. Featured as ACS Editor's Choice.

[3] **Xingchen Dong**, Ali K Yetisen, Heng Tian, Jie Dong, Michael H Köhler, Martin Jakobi, and Alexander W Koch. Analyses of hyperspectral imaging microscopy data sets of semiconducting 2D materials. *Applied Physics Express*, 13(5):052008, 2020.

[4] **Xingchen Dong**, Ali K Yetisen, Michael H Köhler, Jie Dong, Shengjia Wang, Martin Jakobi, Xiaoxing Zhang, and Alexander W Koch. Microscale spectroscopic mapping of 2D optical materials. *Advanced Optical Materials*, 7(18):1900324, 2019.

[5] **Xingchen Dong**, Jie Dong, Ali K Yetisen, Michael H Köhler, Shengjia Wang, Martin Jakobi, and Alexander W Koch. Characterization and layer thickness mapping of two-dimensional MoS_2 flakes via hyperspectral line-scanning microscopy. *Applied Physics Express*, 12(10):102004, 2019.

[6] **Xingchen Dong**, Martin Jakobi, Shengjia Wang, Michael H Köhler, Xiaoxing Zhang, and Alexander W Koch. A review of hyperspectral imaging for nanoscale materials research. *Applied Spectroscopy Reviews*, pages 1–21, 2018.

[7] **Xingchen Dong**. Hyperspektrales abbildungsmikroskopie-linienscanverfahren zur schnellen, großflächigen dickenabbildung von zweidimensionalen materialien, March 24 2020. German patent application, DE 10 2020 XXX XXX.X.

[8] **Xingchen Dong**, Zhendong Li, Jie Dong, Kun Wang, Michael H Köhler, Martin Jakobi, and Alexander W Koch. Line-scan hyperspectral imaging microscopy with structured illumination. In *Unconventional Imaging and Adaptive Optics 2020*, volume 11508, page 115080U. International Society for Optics and Photonics, 2020.

[9] **Xingchen Dong**, Michael H Köhler, Kun Wang, Martin Jakobi, and Alexander W Koch. Mapping the optical dielectric response of isolated monolayer MoS_2 by push-broom microspectroscopy. In *Unconventional Optical Imaging II*, volume 11351, page 113511I. International Society for Optics and Photonics, 2020.

[10] **Xingchen Dong**, Michael H Köhler, Martin Jakobi, and Alexander W Koch. Hyperspectral imaging microscopy for thickness measurement and surface characterization of layered MoS_2. In *Optical Measurement Systems for Industrial Inspection XI*, volume 11056, page 110561S. International Society for Optics and Photonics, 2019.

[11] Kun Wang, **Xingchen Dong**, Michael H Köhler, Patrick Kienle, Qiang Bian, Martin Jakobi, and Alexander W Koch. Advances in optical fiber sensors based on multimode interference (mmi): A review. *IEEE Sensors Journal*, 2020.

[12] Michael H Köhler, Patrick Kienle, **Xingchen Dong**, Michael Schardt, Martin Jakobi, Alexander W Koch, et al. Hyperspectral imager for the mid-infrared spectral range using a single-mirror interferometer and a windowing method. *OSA Continuum*, 2(11):3212–3222, 2019.

[13] Michael H Köhler, Stefan S Naßl, Patrick Kienle, **Xingchen Dong**, and Alexander W Koch. Broadband static fourier transform mid-infrared spectrometer. *Applied Optics*, 58(13):3393–3400, 2019.

[14] Shengjia Wang, Jie Dong, Franziska Pöller, **Xingchen Dong**, Min Lu, Laura M Bilgeri, Martin Jakobi, Félix Salazar-Bloise, and Alexander W Koch. Dual-directional shearography based on a modified common-path configuration using spatial phase shift. *Applied Optics*, 58(3):593–603, 2019.

[15] Jie Dong, Shengjia Wang, Min Lu, Martin Jakobi, Zhanwei Liu, **Xingchen Dong**, Franziska Pöller, Laura Maria Bilgeri, Félix Salazar Bloise, Ali K Yetisen, et al. Real-time dual-sensitive shearography for simultaneous in-plane and out-of-plane strain measurements. *Optics Express*, 27(3):3276–3283, 2019.

[16] Jie Dong, Shengjia Wang, Ali K Yetisen, **Xingchen Dong**, Franziska Pöller, Nicholas Ong, Martin Jakobi, Zhanwei Liu, Félix Salazar Bloise, and Alexan-

der W Koch. Shear-unlimited common-path speckle interferometer. *Optics Letters*, 45(6):1305–1308, 2020.

[17] Michael H Köhler, Patrick Kienle, **Xingchen Dong**, Alexander W Koch, et al. Setup and evaluation of a static imaging fourier transform spectrometer for the mid-infrared spectral range. In *Optical Measurement Systems for Industrial Inspection XI*, volume 11056, page 110561P. International Society for Optics and Photonics, 2019.

[18] Michael H Köhler, Michael Schardt, Hamza B Ghazala, Ennio Colicchia, Patrick Kienle, **Xingchen Dong**, Kun Wang, and Alexander W Koch. Static fourier transform mid-infrared spectrometer with continuous background correction. In *Applied Optical Metrology III*, volume 11102, page 1110218. International Society for Optics and Photonics, 2019.

[19] Michael H Köhler, Michael Müller, Michael Schardt, Patrick Kienle, **Xingchen Dong**, and Alexander W Koch. Statisches fourier-transformationsspektrometer für den mittleren infrarotbereich mit erhöhter spektraler auflösung. In *DGaO Proceedings*, 2019.

[20] Ali K Yetisen, Nan Jiang, Carmen M Castaneda Gonzalez, Zeynep Izlen Erenoglu, Jie Dong, **Xingchen Dong**, Simon Stößer, Martin Brischwein, Haider Butt, Maria F Cordeiro, et al. Scleral lens sensor for ocular electrolyte analysis. *Advanced Materials*, 32(6):1906762, 2020.

[21] Ali K Yetisen, Rosalia Moreddu, Sarah Seifi, Nan Jiang, Katia Vega, **Xingchen Dong**, Jie Dong, Haider Butt, Martin Jakobi, Martin Elsner, et al. Dermal tattoo biosensors for colorimetric metabolite detection. *Angewandte Chemie*, 131(31):10616–10623, 2019.

[22] Nan Jiang, Ali K Yetisen, Nico Linhart, Krzysztof Flisikowski, Jie Dong, **Xingchen Dong**, Haider Butt, Martin Jakobi, Angelika Schnieke, and Alexander W Koch. Fluorescent dermal tattoo biosensors for electrolyte analysis. *Sensors and Actuators B: Chemical*, page 128378, 2020.

[23] Michael H Köhler, Michael Schardt, Michael Müller, Patrick Kienle, Kun Wang, **Xingchen Dong**, Carsten Giebeler, Benjamin R Wiesent, Martin Jakobi, and Alexander W Koch. Static fourier transform mid-infrared spectrometer with increased spectral resolution using a stepped mirror. *OSA Continuum*, 3(8):2134–2142, 2020.

Supervised Student Theses

[1] Zhang Yucheng. Deep-learning-based autofocusing of hyperspectral microscopic imagery. Master thesis, Jun. 2021. In progress.

[2] Qiao Yi. Deep fusion network for segmentation of hyperspectral and optical microscope images. Master thesis, Apr. 2021. In progress.

[3] Zhuo Shi. 3D CNN for hyperspectral microscopic imagery segmentation. Master thesis, Apr. 2021. In progress.

[4] Haoran Cheng. Machine-learning-based multi-label classification of microscopic images of 2D materials. Bachelor thesis, Jul. 2021.

[5] Yuntian Yan. Machine-learning-based segmentation of microscopic images of 2D materials. Bachelor thesis, Jul. 2021.

[6] Hui Xin Zhang. Machine learning for segmenting microscopic imagery of 2D materials. Bachelor thesis, Jul. 2021.

[7] Le Tien Dat. Machine learning for hyperspectral microscopy images segmentation of 2D materials. Bachelor thesis, Feb. 2020.

[8] Jiang Zhutong. Deep-learning-enabled rapid atomic layer mapping of two-dimensional materials. Master thesis, Sep. 2020.

[9] Tian Heng. Deep learning for hyperspectral microscopy images segmentation of two-dimensional materials. Bachelor thesis, Sep. 2020.

[10] Li Zhendong. Line-scan hyperspectral imaging microscopy with structured illumination. Bachelor thesis, Jul. 2020.

[11] Tan WeeMeng. Multivariate analysis of multidimensional data sets acquired by hyperspectral imaging microscopy. Bachelor thesis, Feb. 2020.

[12] Li Zhendong. Resolution-enhanced hyperspectral imaging microscopy with structured illumination. Engineering practice, Oct. 2019.

[13] Tian Heng. Acquire and understand the multidimensional data sets by hyperspectral imaging microscopy. Engineering practice, Oct. 2019.